Title
Sources of Error and Improved Assessment of Trabecular Bone Structure Using In Vivo High-Resolution Peripheral Quantitative Computed Tomography (HR-pQCT)

Author
Sode, Miki

Publication Date
2010

Peer reviewed|Thesis/dissertation

Sources of Error and Improved Assessment of Trabecular Bone Structure Using In Vivo High-Resolution Peripheral Quantitative Computed Tomography (HR-pQCT)

by

Miki Sode

DISSERTATION

Submitted in partial satisfaction of the requirements for the degree of

DOCTOR OF PHILOSOPHY

in

BIOENGINEERING

in the

GRADUATE DIVISION

of the

UNIVERSITY OF CALIFORNIA, SAN FRANCISCO

AND

UNIVERSITY OF CALIFORNIA, BERKELEY

Acknowledgement

First, I would like to express my deepest appreciation to my advisor, Dr. Sharmila Majumdar for her support and giving me a chance to independently explore research topics. I would like to also thank Dr. Thomas M. Link for providing clinical insights and reminding me that my work and everyday clinical practices are symbiotically related. I would also like to thank my other dissertation committee members, Dr. Sarah Nelson and Dr. Tamara Alliston who reviewed each page ensuring a dissertation worthy of a UCSF/Berkeley Ph.D.

It has been my honor and pleasure to be a member of the Musculoskeletal and Quantitative Imaging Research (MQIR) group at UCSF. All members of the MQIR group were very talented people from different backgrounds and cultures. I would never wish for another lab to spend my graduate student days. I feel fortunate and want to thank all of the past and present members of the MQIR group for the chance to work with such talent. I would like to express special thanks to Galateia J. Kazakia, PhD. and Andrew J. Burghardt, who have both been great mentors, role models, and dear friends. I have always appreciated Galateia, ever since she was my graduate student instructor in a biomechanics class at Berkeley. Andy, similarly, has always been there with support, patience, and friendship. Without them, I would not have made it this far. I would also like to thank Gabby Joseph, Ph.D. and Janet Goldenstein, Ph.D. for going through this Ph.D. together. Thank you also to Azucena Rodriguez for standing by me, especially during the qualifying exam. And good luck to Karl Saldanha in completing his Ph.D.

The Joint Graduate Group in Bioengineering is indeed an unparalleled Ph.D. program and I feel grateful to have had the opportunity to spend 5 years with them growing and learning. It was a delight to have met so many wonderful young individuals and enthusiastic professors in the program. Thanks to Dr. Tejal Desai and Dr. Seung-Wuk Lee on

my qualifying examination committee. Dr. Desai and Dr. Roger Cooke were also my academic advisors. Thank you to both of them for their guidance. Special thanks to Joseph R. Leach, Ph.D., for his support and friendship, especially during biochemistry class. Also special thanks to Julia P. Owen for her bright smile; I treasure every stitch we knit together. Finally, thanks to Sarah Jane Taylor and Rebecca Pauling for their administrative support.

When putting the finishing touches on this dissertation (in addition to the dissertation committee members) Galateia, Andy, Dr. Colin Studholme, Joe, and Timur Bilir were kind enough to spare their time reading and editing my drafts and giving feedback to make it something I can be proud of. Thank you.

I would also like to say cheers to a group of strong women in academia who, while contemporaries, have always inspired me: Tammy M. Cleek, Ph.D., Naoko Kurahashi, Ph.D., and Aya Sode, Ph.D. Without witnessing Tammy go through her own Ph.D., and numerous discussions over tea at the Musculoskeletal Biomechanicas Laboratory at NASA Ames Research Center, I would not have pursued my own Ph.D. Naoko walked a similar path at Stanford. We shared the joys and pain of being graduate students. Aya and I share passion for science as well as ballet, and I could not ask for a better sister-in-law. Because of all of you, I was able to be true to myself and held strong. Special thanks to the three of you and go girl power!

And at last but not least, I want to thank my parents, Michiko and Kenji Matsubara, and brother, Naoki Matsubara, for their unconditional love and support throughout my life. I want to give my most special thanks to my amazing husband, Ryo, who has patiently supported me every day these past 5 years. Ryo has also earned his own P.H.D., standing for "Patient Husband Degree."

Writing this acknowledgement makes me realize how fortunate I am to be supported by so many wonderful people. It seems now that this is not just my Ph.D. it is ours – I could not be where I am today without you all. Thank you.

This dissertation work was funded by the following grants: NIH RO1 AG 17762 (SM), Merck & Co., Inc., NIH/NCRR UCSF-CTSI Grant Number UL1 RR024131-01 (AJB), NIH K01 AR056734-01 (GJK), and Graduate Student Research Award Dissertation Award (MS), and UCSF Graduate Dean's Health Science Fellowship.

Abstract

Sources of Error and Improved Assessment of Trabecular Bone Structure Using *In Vivo* High-Resolution Peripheral Quantitative Computed Tomography (HR-pQCT)

Miki Sode

HR-pQCT enables noninvasive *in vivo* characterization of trabecular bone structure at peripheral sites. It can be a powerful tool for assessment of skeletal status and monitoring effect of therapy. The overall objective of this dissertation is two-fold: (i) to characterize errors in the indices describing trabecular structure introduced by partial volume averaging (PVA) and motion artifacts, and (ii) to develop a quantitative technique for estimating error introduced by motion image degradation and a regional analysis technique to account for the inherit spatial heterogeneity of bone structure at the distal radius and tibia.

The first study quantified the degree of error introduced to the topological indices of trabecular bone structure by PVA at *in vivo* resolution of 82 μm. The error in structure model index increased with resampled spatial resolution in a structure-type dependent manner. Connectivity density and degree of anisotropy were constantly underestimated at 82 μm.

The second study proposed a non-subjective technique for measuring subject motion, in which the parallelized projection images at 0° and 180° were compared using sum of squared intensity difference (SSD). SSD correlated strongly to motion-induced error in density, cortical geometric, and trabecular structural indices at the distal radius and tibia.

The third study characterized spatial variability in trabecular structure at the distal radius and tibia by subdividing the cross-section to eight subregions. In addition to

substantial regional variations, the subregions with pronounced gender and age effects were identified.

The fourth study applied subregional analysis to a placebo-controlled randomized pilot study. Significant treatment effects on cortical geometry in the lateral quadrant of the distal radius and the posterior quadrant of the distal tibia were detected in subjects treated with an anti-fracture therapy (alendronate) for 2 years, which was not detected by conventional global analysis.

The results of this work provide a basis for understanding errors in trabecular indices derived from HR-pQCT images as well as a frame-work for quantitative motion detection and regional analysis. The results also serve as a guideline for standardizing protocols across studies, scanners, and study centers, to promote HR-pQCT as an effective tool for assessing skeletal status in research and clinical studies.

Table of Contents

List of Tables

List of Figures

Chapter 1 – Introduction

I. Motivation

Trabecular bone contributes to the mechanical integrity of the whole bone, thereby important for fracture resistance. Its intricate structure dynamically changes throughout life in response to cellular and mechanical stimuli. Noninvasive imaging tools such as high-resolution peripheral quantitative computed tomography (HR-pQCT) can be used to assess skeletal status and monitor the effect of interventions. A number of indices have been introduced and shown to be effective in characterizing trabecular structure. Artifacts inherent in the measurement protocols such as partial volume averaging and motion artifacts still limit the accuracy and reproducibility of the measurement. The conventional global averaging approach may obscure the spatially heterogeneous nature of trabecular structure at the distal radius and tibia. Thorough characterization of the impact on trabecular structure measurements caused by these artifacts is an essential step for any meaningful interpretation of the data and guides improvements in assessment of trabecular structure.

II. Dissertation Aims

The objective of this dissertation is two-fold:

1) To characterize two sources of error – namely, partial volume averaging and motion artifact– that are associated with assessment of trabecular bone structure indices from HR-pQCT images at the distal radius and tibia.
2) To develop two techniques for improved assessment of trabecular bone structure indices using HR-pQCT – a non-subjective quantitative technique to estimating error

introduced by motion image degradation and a regional analysis technique to account for the inherit spatial heterogeneity of bone structure at the distal radius and tibia.

III. Bioengineering Contributions

The primary contributions of this dissertation study are:

3) Quantification of the degree of error introduced to the non-metric indices (structure model index, connectivity density and degree of anisotropy) for trabecular bone structure in relation to varying nominal resolutions (10 to 82 μm).
4) Development of a quantitative approach for detecting motion artifacts during HR-pQCT image acquisition.
5) Development of regional analysis that accounts for spatial heterogeneity of the trabecular structure at the distal radius and tibia.

IV. Chapter Organization

Chapter 1 provides a background of the complex nature of bone, including its function, composition, structure, material properties, as well as its development, adaptation and maintenance. It also introduces techniques for imaging and characterization of bone using x-ray based imaging modalities, and highlights known associated artifacts. Chapter 2 discusses limited imaging resolution and its effect on the accuracy of the non-metric structural index calculation. Chapter 3 proposes a quantitative approach for detecting motion artifacts in HR-pQCT images. Chapter 4 develops a regional analysis of trabecular bone structure to reflect its heterogeneous nature. In Chapter 5, regional analysis is applied to a representative clinical study to demonstrate how it can be utilized. Finally Chapter 6 summarizes the presented work, and provides directions for future work.

Chapter 2 – Background

I. Bone

There are 206 bones in the adult human skeleton. Each bone has a unique form that is adapted to a specific function. Bone is a living organ that is continuously remodeled to adapt to its environment.

Bone serves both mechanical and physiological functions. Physiologically, bone is a source of essential minerals such as calcium, as well as growth factors and cytokines [1], thereby plays a significant role in regulation of metabolic homeostasis and provides a niche environment for hematopoiesis [2, 3]. Mechanically, bone provides protection by encasing vital organs. The skeleton also provides support, allows motion, and plays a key role in locomotion – providing not only its basic shape and support to the body, but also anchor points and levers for other soft tissues, such as muscle. This thesis is written predominantly in the context of the mechanical function of bone.

In order to support the body against gravity and withstand mechanical impact, bone should be strong and resilient. At the same time, to facilitate locomotion, it needs to be lightweight. Bone meets these mechanical challenges through a combination of its material and structural properties. Its composition and the organization of microstructures give rise to the tissue level material properties. In addition, morphology and the organization of macrostructures give rise to the apparent mechanical properties. These multi-level properties are reviewed in the following section. Characterization of bone morphology and structure is a frequent research objective for assessment of the overall mechanical integrity of the whole bone.

1. Composition

Bone is a composite material composed mainly of inorganic minerals such as calcium hydroxyapatite ($Ca_{10}(PO_4)_6(OH)_2$) (50-70 % by weight), organic molecules such as Type I collagen (20-40 %), water (5-10 %), and lipids (<3 %) [4, 5]. Bone composition varies with age, anatomic location, diet, and health [4]. In a bone matrix, the mineral phase is embedded in the collagen network. The mineral phase contributes greatly to the material and mechanical properties particularly to rigidity [6-10]. Bone becomes more mineralized as it matures. Stiffness and strength increase exponentially with the mineral content, more than with an equal-density increase in bone volume [11]. Metabolically, bones contribute to mineral homeostasis by serving as a source of calcium, phosphate and magnesium. Collagen forms a network in bone matrix by cross-linking and provides ductility by absorbing energy of applied external forces, thereby contributing to mechanical toughness [4, 12] and tensile strength [13, 14]. Water is found mostly in pore spaces. Water plays a role in cell signaling as well as iron-, nutrient- and waste-transport between cells. Mechanically, water also contributes to the viscoelastic character of bone [15-17].

2. Morphology

The proximal ends of a long bone are called epiphyses and are slightly broadened. The articular cartilage covers the exterior. The shaft of a long bone is called the diaphysis and its cross-sectional shape is a hollow cylinder (tube) with a wall of compact bone and medullary cavity filled with marrow (**Figure 2.1**). Both the exterior and interior surfaces (called periosteal and endosteal surfaces, respectively) are covered by a thin layer of connective tissue called

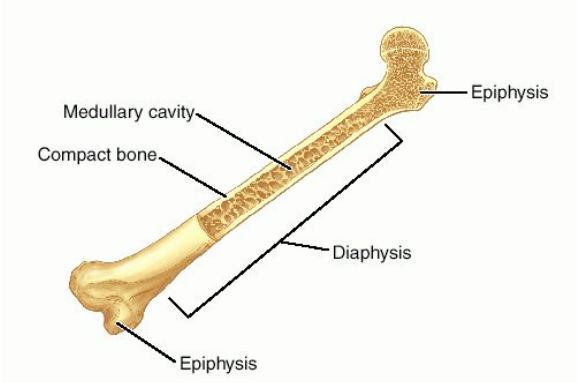

Figure 2.1 Schematic of a long bone (femur).

periosteum and endosteum, respectively. The former is a fibrocollagenous layer containing stem cells and serves as neurovascular supply, while the latter is a layer of stem cells and inactive bone forming cells called bone lining cells.

There are two morphological forms of bone – cortical (compact) and trabecular (spongy or cancellous) (**Figure 2.2** and **Figure 2.3**). The cortical bone comprises the exterior while the trabecular compartment is in the interior of the bone. Overall, in the human skeleton, 85% of bone is cortical and 15% is trabecular by weight with a locally varying ratio depending on site [4] – for instance, the diaphysis of a long bone is a hollow cylinder of cortical bone (**Figure 2.2**) while a vertebral body is highly trabecular with a thin cortical shell (**Figure 2.3**).

Figure 2.2 (left) The coronal cross-section of the proximal femur showing a highly trabecularized epiphysis and thick cortical shell of the diaphysis. (Courtesy of Smithsonian National Museum of Natural History.)

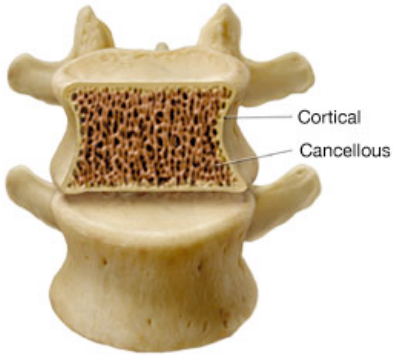

Figure 2.3 (right) The coronal cross-section of a human vertebra showing its highly trabecularized interior. (Courtesy of American Medical Association.)

The two morphologies serve different functions. Cortical bone is dense and comprised of lengthwise columns called the Haversian system or osteons (**Figure 2.4**). Each osteon consists of mineralized collagen fibrils called lamellae arranged concentrically around neurovascular canals called Haversian canals. They run parallel to the length of the bone, connect to canals running perpendicularly between the periosteal and endosteal surfaces supplying blood called Volkmann's canals. Interstitial lamellae, which are the remnants of old osteons, fill the area between current osteons. Outer circumferential

lamellae form a sheet-like structure at the periphery of the cortical bone interfacing the periosteum. Within pits called lacunae of the lamellae, bone cells called osteocytes are found, entrapped themselves as they secrete bone matrix to construct osteonal structure. Osteocytes are interconnected by their cytoplasmic extensions through thin canals called canaliculi. Cortical thickness varies from 1 to 5 mm depending on the site. Cortical bone provides structural support to the body and protection to the internal tissues of a bone.

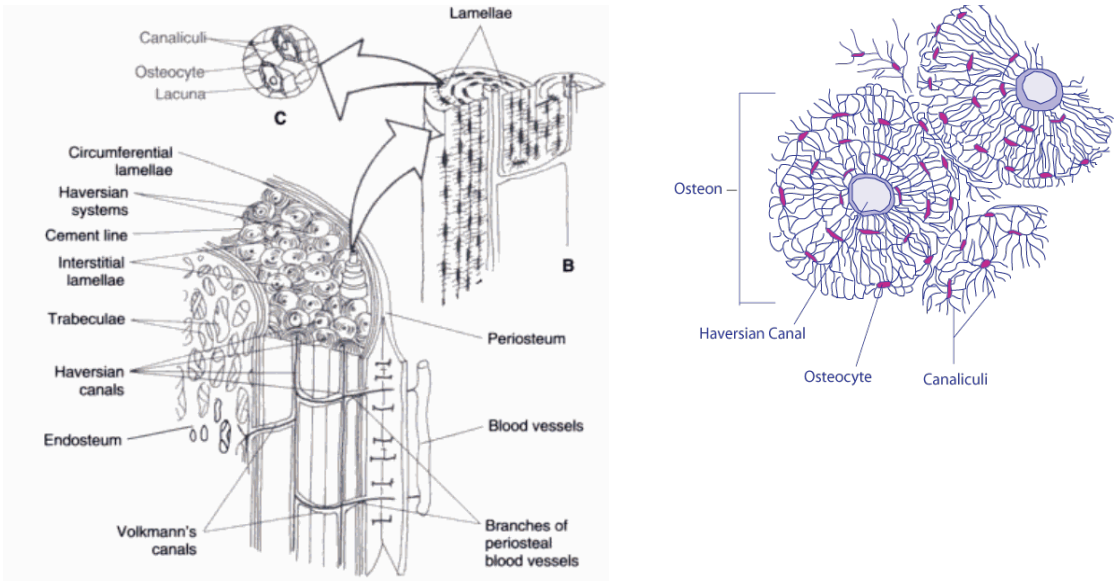

Figure 2.4 (Left) The schematic of cortical bone structure (From M Nordin and VH Frankel: Basic Biomechanics of the Musculoskeletal System, 2nd edition. Philadelphia, Lea G Febtger, 1989) [18]. (Right) A cross-section of Haversian systems (osteons) (from Gray's Anatomy; Figure 77) [19].

Trabecular bone is a porous structure with an intricate network of trabeculae. Each trabecula ranges from 100-150 μm thick, spaced 500-1000 μm on average, depending on the site [20, 21]. It has nearly 10 times the surface area compared to cortical bone. Due to its proximity to bone marrow, its primary function is metabolic in nature. In fact, trabecular bone is 8 times more metabolically active than cortical bone [22]. Trabecular bone is responsive to several factors, including metabolic factors, hormonal balance, daily mechanical loading patterns, and drug therapies. By virtue of its structure, trabecular bone

also contributes mechanically by dispersing applied loads as seen at the head of the femur (**Figure 2.2**).

3. Material properties

Prior to the discussion of bone's material properties, some related terms must be defined. Material properties are intrinsic mechanical properties due to tissue composition and microstructure. The mechanical response of a material under a certain loading condition is generally represented using a stress-strain curve (**Figure 2.5**). This plots stress as a function of deformation per applied load (strain). In a linear regime, the material deforms linearly under load, absorbing applied energy without causing permanent damage. The slope of this linear portion is called the modulus of elasticity (Young's modules, E), and is a measure of specific resistance to strain against a deforming force. In a plastic regime, the stress-strain curve starts to bend as applied force causes deformation that is no longer reversible upon unloading due to microdamage. Yield is the transitional point between linear and plastic regimes. The amount of strain that the material can sustain without structural failure determines its brittleness/ductility — the more strain the material can sustain in this plastic phase, the more ductile it is. The yield strain and stress of mature cortical bone in compression are approximately 6800 με and 130 MPa, respectively [4, 23]. Ultimate strength is the maximum stress the material can withstand without structural failure (fracture). The ultimate strain and stress of mature cortical bone in compression are approximately 15000 με and 200 MPa, respectively [4]. Finally, toughness refers to the area under the whole stress-strain curve. Mechanically, it signifies the amount of energy deposition the material can withstand. Ductility determines toughness more than strength or stiffness, because ductile bone can withstand higher strain, which contributes more to area under the stress-strain curve.

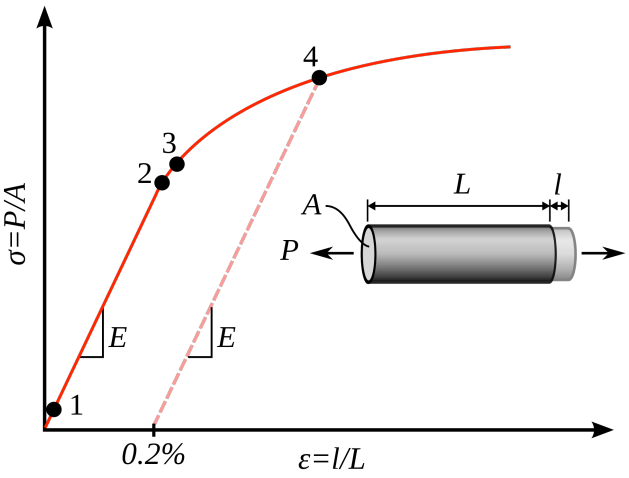

Figure 2.5 A typical stress-strain curve showing yield behavior for nonferrous alloys [24]. Elastic modulus E is the slope of the linear regime (point 1 to 2) where the material deforms linearly without causing permanent damage. The deformation in the plastic regime (point 3 to 4) is not reversible due to microdamage. The transition between the linear and plastic regimes is the yield.

Bone is a viscoelastic material, where both elastic and strength properties are dependent on the rate and duration of the applied load. **Figure 2.6** shows stress-strain curves under compressive and tensile loading. Bone is also an anisotropic material, and its mechanical response therefore differs depending on the relative orientation of the microstructure and applied load [25]. For example, bone is 40% stiffer in the longitudinal direction compared to the transverse direction [26]; the Young's modulus of bone depends the mode and direction of the applied load – it ranges from 11.5 GPa (transverse direction) to 17.0 GPa (longitudinal) for the femur cortical bone on average [26-28]. The material properties of bone tissue are similar for both cortical and trabecular compartments [26], although their dramatic geometric and structural differences add complexity to, and contribute differently to, the overall mechanical properties.

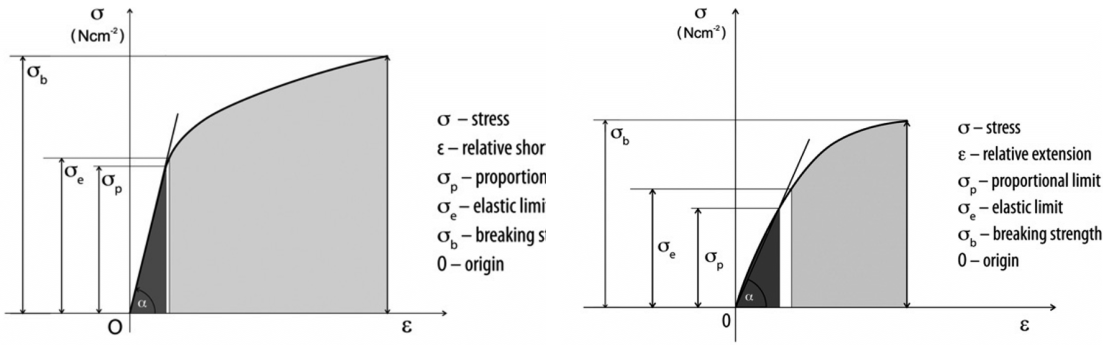

Figure 2.6 Stress-strain curve under compressive loading (left) and tensile loading (right) for bone. (Adapted from Wendlova 2008 [29])

4. Bone adaptation

Bone is a living organ that continuously remodels itself to adapt to its environment. As assessment of skeletal status are often an objective of the quantification of trabecular structure, the following section reviews bone adaptation mechanism. As aging is a predominant factor for alteration of bone properties, the majority of research and clinical studies on trabecular bone are related to aging, such as age-related osteoporosis and evaluations of its interventions. The following section, therefore, also reviews age-related alteration in bone.

Cells involved

There are three cell types involved in bone modeling, remodeling and adaptation/maintenance: osteoblasts, osteoclasts, and osteocytes. These cells are derived from two cell lineages: Osteoblasts and osteocytes originate from osteoprogenitor cells while osteoclasts originate from hematopoetic progenitor cells [30]. Osteoblasts are responsible for the production of new bone matrix. Osteoclasts are multinucleated cells responsible for bone resorption. While osteoblasts and osteoclasts are found on the surface of bone, osteocytes are embedded in the bone matrix. Osteocytes are terminally differentiated osteoblasts that are surrounded by the matrix. They are capable of production as well as resorption of the surrounding matrix to a limited extent. In addition,

they play a major role in mechanosensing and transduction thereby facilitating bone maintenance/remodeling through the activation of osteoblasts and osteoclasts [31, 32].

Bone remodeling and adaptation

Bone remodeling is an essential process for adaptation and maintenance and serves the mechanical and metabolic functions of bone. Mechanically, sustaining the structural integrity is important for fracture prevention. For example, microcracks in bones trigger bone remodeling [33]. It is also necessary to adjust material and structural properties to withstand changing mechanical demands. Osteocytes embedded in the bone matrix are said to be responsible for mechanosensing — their processes in the lacno-canaleculer network senses the alteration in fluid pressure, stretch, or strain by the external force, resulting in sending a signal to initiate bone remodeling. Metabolically, calcium, phosphate and other minerals should be replenished constantly to maintain the mineral homeostasis. In response to changing local biochemical environment bones can adjust, the amount and type of minerals as well.

Bone remodeling occurs in four steps — activation, resorption, reversal and formation — involving the basic multicellular unit (BMU), which is comprised of osteoblasts and osteoclasts (**Figure 2.7**). During the activation phase, mono-nucleated osteoclast precursor cells are recruited. After fusion of several mono-nucleated cells, osteoclasts mature and start resorbing bone matrix by lowering the pH of the matrix with the secreted acid and enzymes. During the formation phase, osteoblasts secrete a collagenous organic matrix and then regulate its mineralization. After bone formation, 30-50% of osteoblasts are either entrapped in the matrix and become osteocytes. They can also enter the quiescent phase on the surface and coat the newly formed bone matrix as bone-lining cells [4]. It is this balance between bone formation and resorption turnover rate) that maintains

the basic shape of the bone suitable for the local environment. Since bone surfaces are subject to constant turnover, bone is less mineralized at the surface.

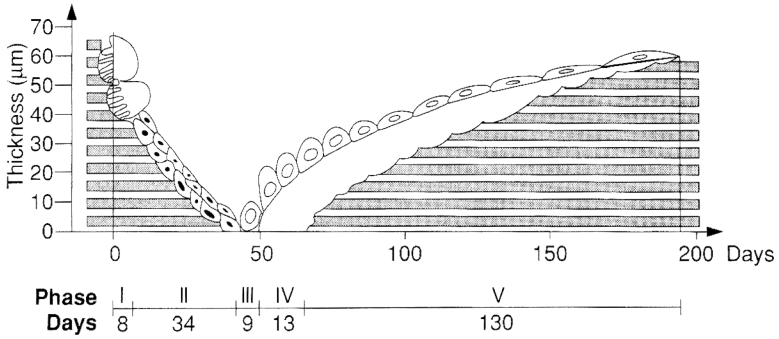

Figure 2.7 The activity of basic multicellular unit for the duration of a complete cycle of trabecular bone turnover process (Adopted from Favus 2003 and Eriksen et al 1994 [4, 34]).

Aging

Aging affects both material and structural properties of bone throughout a lifespan, the. Bone turnover rate is positive (favoring bone formation) during growth. After skeletal maturation, the bone formation rate matches the resorption rate. Bone turnover rate then turns negative (favoring bone resorption). The onset of age-related changes appears in midlife or later in cortical compartment but as early as in young adulthood in trabecular compartment [35, 36].

The consequential age-related change in the composition is elevated mineralization, reduced collagen content, and microdamage accumulation [37, 38]. As a result, material properties at the tissue level become stiffer (higher E) but more brittle (shorter plastic phase, thus smaller area under the strain-stress curve) [39, 40]. In the apparent level, the mechanical integrity is reduced with microdamage accumulation and the alteration of local stress distribution due to resorption cavities, which are particularly detrimental in the trabecular region when coupled with high strain. Upon menopause, women experience accelerated bone loss due to an estrogen deficiency.

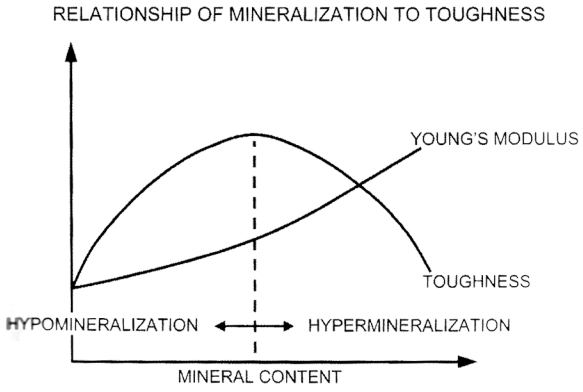

Figure 2.8 The relationship between bone mineral content and tissue-level toughness. The optimal toughness is achieved when bone is 64-66% (by weight) mineralized (Adapted from [4, 41]).

Age-related changes appear in midlife or later in the cortical compartment, while they appear as early as young adulthood in the trabecular compartment [35, 36]. These changes are attributed to the intricate structure of trabecular bone. In the cortex, thickness decreases and porosity increases. In the trabecular compartment, trabeculae become thinner, and plate-like structures become perforated and more rod-like, often resulting in disruption and loss of connectivity (**Figure 2.9**). The combined effects on the apparent mechanical properties are a 7-12% per decade decrease in elastic modulus and a 2-5% decrease in cortical bone strength and a 8-10% decrease in trabecular bone strength [4, 42, 43].

Age-related changes in trabeculae vary depending on site [44]. For example, the onset of age-related decline in cortical bone mineral density (BMD; mg/cm^3) and concurrent increase in cortical porosity is latent by approximately a decade (in 50s to 60s) at the distal radius compared to the tibia (in 40s to 50s) [44, 45]. Similarly, in the trabecular compartment of the distal radius, the onset of trabecular bone volume loss occurs around midlife. Although trabeculae thicken slightly before age 50, the number drops dramatically after midlife for both women and men. At the distal tibia, on the other hand, the onset of bone loss is as early as in young adulthood [36, 44, 46, 47], accompanied by steady decline in the thickness and number of trabeculae for both genders [48].

Age-related changes in trabeculae also vary depending on gender [35, 44, 46]. Decrease in volumetric BMD at the lumber spine and femoral neck is greater in women than in men (-55% vs. -46%, respectively; $p < 0.001$) but similar at the peripheral sites (-24% and -26%, respectively; not significant) [35], for instance. This gender difference in age-related decrease in trabecular vBMD is attributed to differing mechanisms — bone loss occurs by trabecular disruption for women (as evident in fewer numbers of trabeculae for women especially escalated upon menopause in (**Figure 2.10** B) but by trabecular thinning for men (**Figure 2.10** C) [46, 49]. Perforation starts with horizontal trabeculae, increasing the degree of anisotropy as a result [50-52]. Loss of trabecular connectivity is indeed detrimental, increasing fracture risk more than by thinning [53-55]. These gender differences in age-related changes in middle-age to elderly adults are strongly associated with sex steroids, particularly bio estradiol levels [56]. In fact, estrogen deficiencies upon menopause shortens the lifespan of osteoblasts but extends the lifespan of osteoclasts [57], causing bone formation/remodeling balance to be more negative in addition to other age-related effects. As a result, bone resorption is favored and resorption pits deepen, leading to disruption of trabeculae in women.

Given the same amount of external loading, more stress is imposed on the bone; therefore, the risk of fracture increases with age. In fact, the annual incidence of age-related osteoporotic fracture is over 1.5 million in the United States, with hip and vertebrae fractures being the most prevalent. The level of stress that women's vertebrae can withstand decreases with age (-43% vs. -31% in men between 20 and 90 years old; $p = 0.008$) [58]. This is reflected in the high incidence of vertebral fracture among women [59] (**Figure 2.11**).

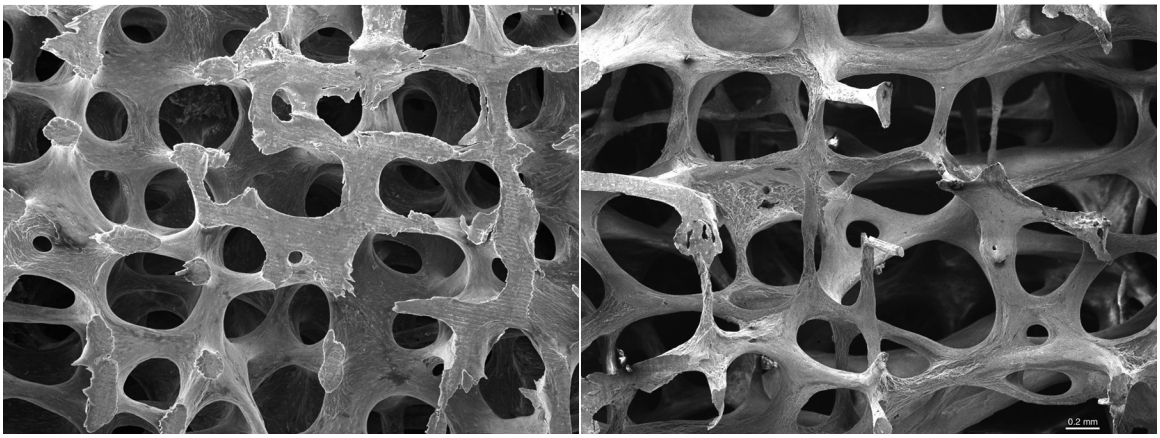

Figure 2.9 Scanning Electron Microscope images of normal (left) and osteoporotic (right) trabecular bone architecture at the third lumbar vertebrae. © Tim Arnett, University College London (Retrieved July 19 2010 from http://www.brsoc.org.uk/gallery/images/19lg.jpg).

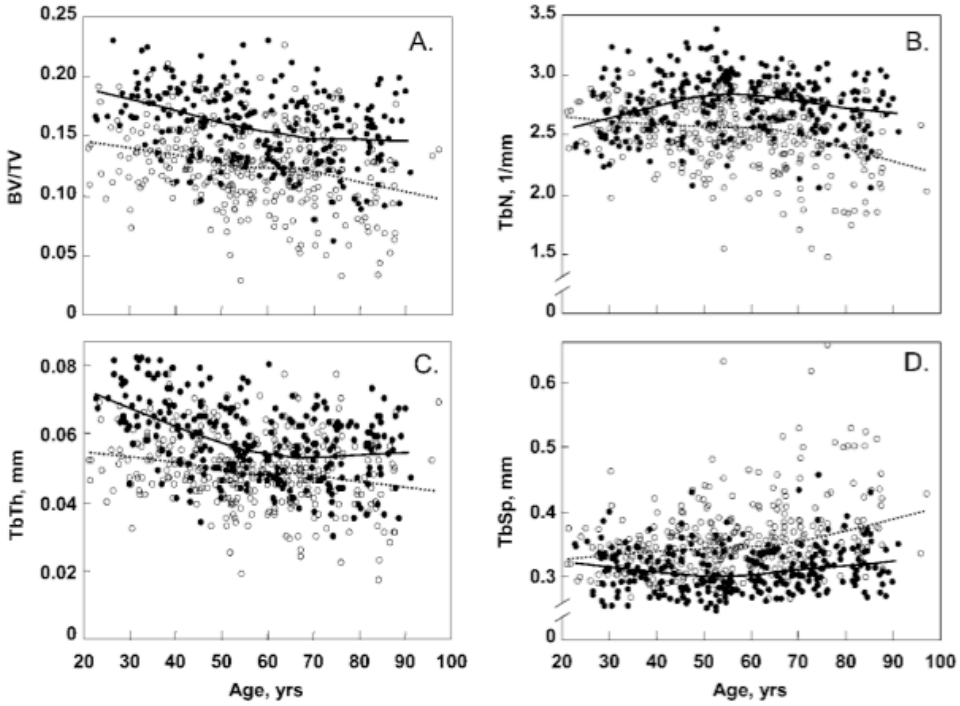

Figure 2.10 Age-related changes in trabecular bone structure indices at the distal radius in women (open circles with dashed line) and men (closed circles with solid line). (Adapted from Khosla 2006 [56])

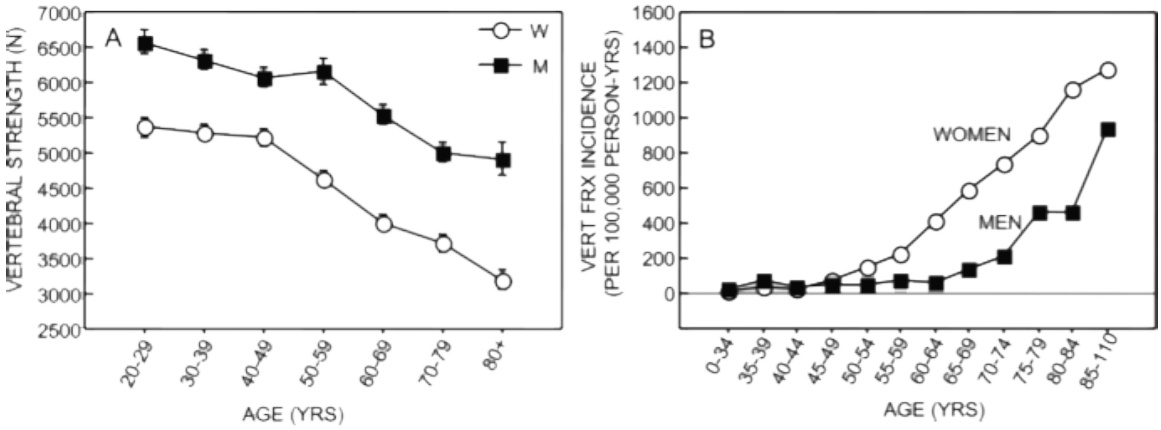

Figure 2.11 Vertebral compressive strength declines gradually with age but sharply after age 50 for women (left). This is reflected on high incidence of vertebral fracture (right). (Adapted from Bouxsein et al 2006 [58]).

II. Imaging of bone

The major modes for imaging bone are all x-ray based imaging technologies, such as radiography, dual x-ray energy absorptiometry (DXA), and computed tomography (CT). Photons interact with tissues as they penetrate through the body. Some are absorbed, causing attenuation, and others are scattered in the process. The attenuated x-ray energy depends on the quantity and intrinsic densities of substances it penetrated during its path. As 45% of bone is mineral phase, the attenuation profile of bone is substantially different from that of the surrounding soft tissue. Essentially this x-ray attenuation contrast between bone and soft tissue results in x-ray based image.

While x-ray imaging technology has revolutionized clinical practice by allowing visualization of internal organs non-invasively, it is not free of risks. Exposure to ionizing radiation (Table 1.1) is the major concern associated with x-ray imaging technology, especially for vital organs, and for children and pregnant women, as it may increase the lifetime cancer risk and cause developmental defects.

Table 2.1 The typical effective x-ray dose during an examination using the clinically used modalities [60, 61].

Modality	Anatomical site	Typical effective dose (mSV)
X-ray (radiography)	Chest	0.1
	Extremities (hand, foot)	0.005
CT	Head	2.0
	Chest	7.0
Cardiac CT Angiogram	Heart	~13
Mammography	Breast	0.36
DXA	Whole body	0.001
HR-pQCT	Extremities (Wrist, Ankle)	0.003
Dental (panoramic)	Teeth	0.01
Naturally occurring background radiation (per year)	Whole body	1-3

Non-x-ray based imaging modalities, such as magnetic resonance (MR) imaging, positron emission tomography (PET), and ultrasound are also available for specialized needs. Discussions on MR, PET and ultrasound are beyond the scope of this dissertation. In the following section, 3 types of CT systems used for characterizing trabecular bone structure, namely, CT, HR-pQCT, and μCT are reviewed.

Computed tomography (CT)

In computed tomography, the x-ray source and the detector rotate about the subject taking multiple projection images. The three-dimensional (volumetric) image is computationally reconstructed from the series of raw two-dimensional images. Several generations of CT were introduced as x-ray beam and detector configurations evolved. Currently available clinical CT scanners (**Figure 2.13 A**) have a cone-beam configuration with a multi-row areal detector for expedited image acquisition. Newer generation CT scanners have faster scan times owing to the improvements in x-ray source, detector and computer. CT is widely used clinically for cardiovascular, brain, gastrointestinal, as well as musculoskeletal evaluations. A contrast agent can be administered intravenously for angiographic studies.

Density values can be obtained quantitatively from grayscale values of a CT image (called quantitative CT, QCT) [62, 63]. Grayscale of the image can be calibrated by a calibration phantom contains cylinders of hydroxyapatite (HA)-resin mixtures with different concentrations. Attenuation values are converted to equivalent HA densities (mg HA/cm^3) using a linear relationship based on the attenuation values of the cylinders in a phantom.

The nominal resolution achievable by a whole body clinical CT is 0.25 to 0.50 mm. Its field of view is 40 cm. While the spatial resolution may be inferior to that of radiographs, the contrast resolution is superior in CT (it can detect more subtle variation in attenuation of x-rays). Other advantages include volumetric image acquisition, shorter acquisition time for large volume coverage, allowing digital image processing and digital storage.

For research purposes, CT scanners are available with various resolutions such as high-resolution peripheral QCT (HR-pQCT) (**Figure 2.13 B**), peripheral QCT (pQCT), μCT (**Figure 2.13 C**), and synchrotron radiation μCT (SRμCT), in the order of decreasing attainable nominal resolution.

1.1. HR-pQCT

HR-pQCT can achieve a nominal resolution of 82 μm (**Figure 2.13 B**), which enable *in vivo* assessment of trabecular bone structure at peripheral sites (specifically at the distal radius and tibia). In the recent years, use of HR-pQCT in skeletal research is rising. The accuracy for density, cortical geometry, trabecular structure parameters calculated from HR-pQCT images have been validated against the values from calibration phantom [64], DXA, and μCT measurements [65-68]. The *in vivo* reproducibility for these parameters has been assessed [69-73] to be CV_{rms} = < 1% and < 4.5% for the densitometric measures and trabecular structure indices, respectively [71]. Biomechanical parameters using micro finite element (μFE) analysis have also been tested against mechanically-tested values [65, 74,

75]. Population-based age-related changes in density, cortical geometry, trabecular structure parameters at the distal radius and tibia have been assessed using HR-pQCT [35, 44, 45, 56, 69, 76-79]. The predictive power of HR-pQCT-obtained trabecular structure indices for disease [69] and fracture status [80-85] has been demonstrated; the efficacy of osteoporosis drugs have also been monitored this modality [86, 87]. Collectively, HR-pQCT has been establishing its potential as a powerful noninvasive tool for assessing skeletal status and related research studies.

The *in vivo* HR-pQCT scanner (XtremeCT, Scanco Medical, Brüttisellen, Switzerland) (**Figure 2.13 B**), used in our laboratory, is a cone-beam CT system with 18.6° fan angle and 3.0° cone angle. It is equipped with the x-ray source potential at 60 kVp with a current of 900 μA. A two-dimensional detector containing a 3072 × 256 CCD elements is used to acquire 750 projections over 180° at a 100 ms integration time at each angular position. The 12.6 mm field of view is reconstructed across a 1536 × 1536 matrix using a modified Feldkamp algorithm, yielding 82 μm isotropic voxels. Image acquisition time is 3 minutes per scan. The effective dose is < 3 μSV per measurement [88].

Attenuation values are converted to equivalent hydroxyapatite density (mg HA/cm^3) using a linear relationship based on a phantom containing cylinders of HA-resin mixtures with five different concentrations (0, 100, 200, 400, and 800 mg HA/cm^3) (QRM, Moehrendorf, Germany) (**Figure 2.13 B**). For quality control, the linear attenuation values of the phantom are monitored daily.

Prior to image acquisition, the subject's forearm and lower leg are positioned in the thumb-up and toe-up positions, respectively. They are immobilized in corresponding carbon-fiber molds, and fixed to the scanner to minimize motion during acquisition. A 9.02-mm-long section (110 slices) of the radius and tibia is imaged starting at 9.5 mm and 22.5 mm proximal to the distal endplate, respectively, extending proximally (**Figure 2.12**).

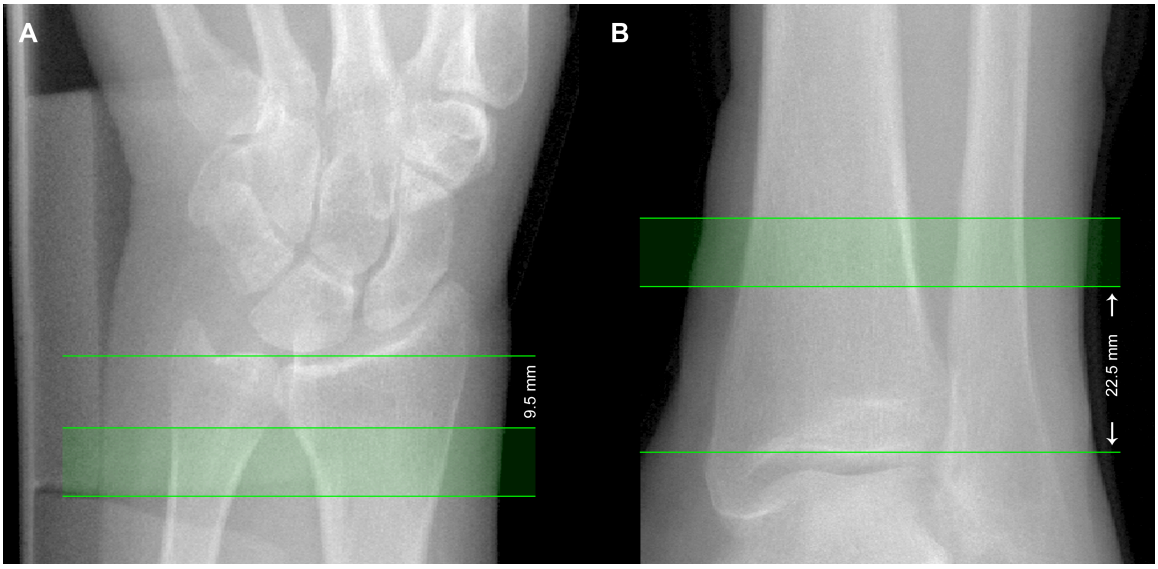

Figure 2.12 The standard location for HR-pQCT image acquisition and measurement, with respect to the reference landmarks at the distal radius (left) and tibia (right) (Courtesy of A.J.Burghardt).

1.2. μCT

The nominal resolution of μCT (**Figure 2.13 C**) is as small as 6 μm. In order to achieve such high spatial resolution, the size of the object being scanned is limited. Both specimen scanners and in-vivo scanners are available. For the former closed system, a specimen is limited and must fit within 38 mm in diameter and 80 mm in length. Bone biopsies are often imaged using a μCT system, for example. The latter is an open system, basically a miniature version of a clinical whole body CT for humans, and used for live sedated small animals. Similar to the other CT systems, the attenuation values are converted to the density values according to the linear relationship between grayscale values and the cylinders of HA-resin mixtures of known concentrations of the calibration phantom (**Figure 2.13 C**). These values are monitored daily for quality control purposes.

A. Multi-detector CT (GE)

B. HR-pQCT (XtremeCT, Scanco Medical)

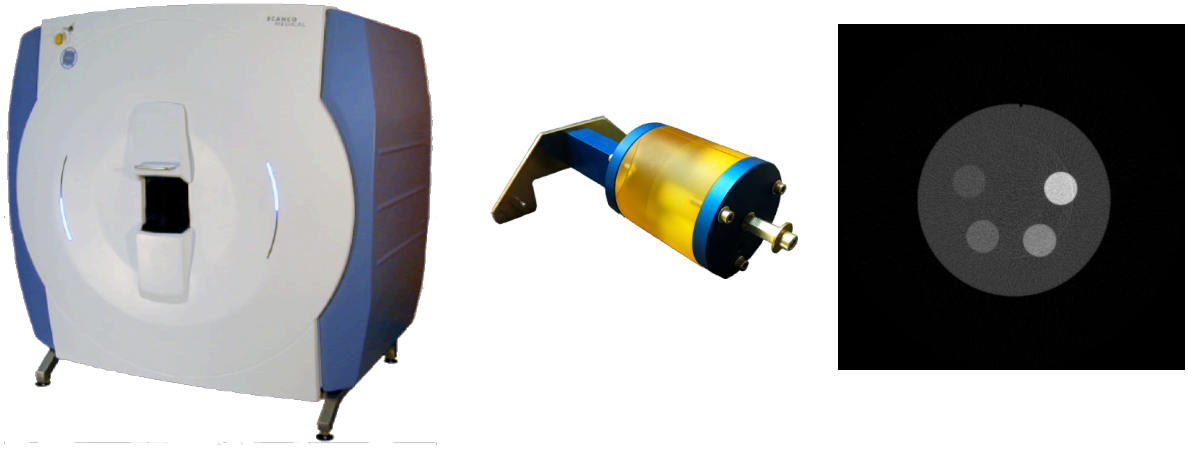

C. Desktop µCT (µCT40, Scanco Medical)

Figure 2.13 Two commonly used *in vivo* CT systems (A) a multi-detector computed tomography by GE for the whole body and (B) HR-pQCT for the peripheral sites and (C) ex vivo CT system for specimens, desktop µCT, their calibration phantoms and their corresponding grayscale images.

III. Characterization of bone using HR-pQCT

Accurate assessment of bone quality is a key component for determining the health status of bone, as well as for prevention, prognosis and diagnosis of disease affecting bone. The strength of bone is determined by the quality and quantity of mineralized skeletal bone tissue, and provides crucial information in predicting fracture risk. The quality of bone is determined by the combination of features such as mineralization, architecture, turnover, collagen cross-link and damage accumulation [89]. This section introduces density, cortical geometry and trabecular structural indices routinely obtained from HR-pQCT images, as well as the ways in which they are commonly characterized.

Density

X-ray-based imaging modalities create images based on the differences in attenuation values of matter in x-ray paths. Attenuation in the skeleton depends on density, which is predominated by the mineral phase of bone. Areal bone mineral density (aBMD) [g/cm^2] measured using dual x-ray energy absorptiometry (DXA) is currently used for the routine diagnosis of osteoporosis. DXA-measured aBMD is highly correlated to biomechanically-tested maximum compressive vertebrae strength [7, 90-92]. Clinically, women without fractures have a significantly higher aBMD at their spine and hip compared to those with fractures [93]. Notice, however, aBMD is a projected/areal measurement, and it reflects both the mineral content (degree of mineralization) as well as the volume (the amount of mineralized tissue) [94], therefore, the size and geometry of the bone and trabecular bone structure are ignored.

The raw image of attenuation values can be calibrated by acquiring images with a density phantom (as described previously) and converted to display quantitative density information. The volumetric bone mineral density (vBMD)[g/cm^3], calculated as the mean

density of all voxels within a volume of interest (VOI), is assessed quantitatively in this manner.

Densitometric indices explain 70% of bone strength [89]. For example, every standard deviation decrease in trabecular vBMD at the distal radius, distal tibia, or vertebra is associated with ~1.5 times increase in fracture prevalence, independent from aBMD [84, 95, 96]. However, the remaining 30% is unexplained and fracture risk increases independent of reduction in BMD with age [97]. The four- to five-fold decrease in strength at the spine from the age of 20 to 80 years also cannot be explained by the two-fold decrease in trabecular apparent BMD [52] either. This is partly attributed to the fact that BMD alone cannot account for all bone fragility in many individuals. For instance, alteration in intrinsic material properties caused by some clinical conditions such as aging, corticosteroid use, osteogenesis imperfecta, and diabetes may not be fully reflected in BMD [4].

Cortical geometry

Cortical thickness (Ct.Th) and cortical area (Ct.Ar) are calculated using an annular model approximation: $Ct.Th = Ct.Ar/\pi(r_{per}+r_{med})$, where r_{per} and r_{med} are the periosteal and medullary radii, respectively. Since it is difficult to define the trabecular and cortical boundary (endosteal surface), $r_{per} \cong r_{med}$, the denominator is effectively $2\pi r_{per}$. Cortical area (Ct.Ar) is directly related to bone's ability to withstand an applied load, as expressed in stress = force/area. With age, in the diaphysis of the long bone, Ct.Ar increases but Ct.Th decreases as periosteal expansion increased r_{per}. Micro-finite element (μFE)-estimated failure load at the distal radius is highly associated with Ct.Th ($r = 0.69$) [80, 81]. Accordingly, decrease in Ct.Th increases the risk of wrist fractures significantly (with the odds ratio = 4.0 to 5.4) [80, 98].

Trabecular structure

Trabecular structure is a mixture of plate-and rod-like structure of various thickness oriented in various direction (**Figure 2.14**). A variety of indices describing the structural features have been introduced – from tissue volume and metric indices such as thickness and distribution, to topological features (non-metric indices).

1.3. Metric indices

The bone volume fraction (BV/TV) is a measure of the amount of bone. BV/TV is highly correlated to the mechanical properties of trabecular bone [99-101] as they are greatly influenced by the volume as well as the degree of mineralization. The trabecular number (Tb.N) is a measure of the number of trabeculae and the trabecular thickness (Tb.Th) is the mean thickness of trabeculae within a unit volume. The vertical trabeculae are about 30% thicker than the horizontal struts at vertebrae [102]. With the same amount of bone volume reduction, the impact/reductions on both the modulus and strength is greater by the reduction in Tb.N compared to by the reduction in Tb.Th [53-55]. While Tb.Th can be recovered with therapeutical interventions, reductions in Tb.N cannot be reversed once a trabecula is lost [103-106]. Trabecular separation or spacing (Tb.Sp) refers to the average distance between individual trabeculae within a unit volume. With age, the trabecular compartment loses bone volume through trabecular thinning, followed by perforation, resulting in scarcity with sporadic remnants [107].

1.4. Non-metric indices

The structure model index (SMI), which is derived from surface convexity, has been proposed as a feature by which to classify the trabecular bone structure type — specifically, the degree to which the structural elements resemble plate-like or rod-like geometries. A rod-like trabecular bone structure is characteristic of osteoporotic patients [108] and is

strongly correlated with bone strength [101]. The degree of trabecular connectivity, measured by connectivity density (Conn.D), also provides valuable information, since loss of connectivity has a substantial impact on structural integrity and results in an elevated fracture risk [38, 53, 109]. The degree of anisotropy (DA) is a measure of directional variation of a structure. Though not directly correlated with the mechanical properties of bone, DA provides insight into the directional dependence of bone strength [38, 110]. With age, trabecular bone is known to become more rod-like [111], with connectivity being lost by disruption of thin horizontal trabeculae, and increasingly anisotropic [50-52].

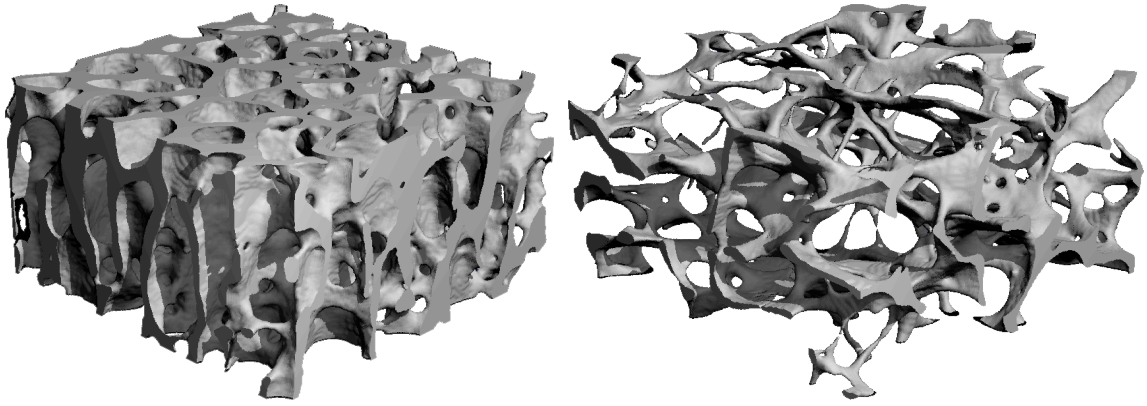

Figure 2.14 Comparing the visual appearance and the structure indices of two distinctly different trabecular bone section at the femoral head of a 67 years old male: (left) thicker and more plate-like trabecular structure in the superior region, and (right) thinner and more rod-like trabecular structure in the inferior region.

1.5. Calculation of trabecular structural indices

Trabecular structures contribute greatly to the mechanical integrity of the whole bone. Each structural feature uniquely contributes to the overall mechanical property, however. Therefore, the accurate characterization of these indices cannot be overlooked.

At an 82-μm isotropic voxel size achieved using HR-pQCT, the average human trabeculae only spans 1 to 2 voxels in diameter. Due to significant partial volume effects, this relatively low resolution confounds the thresholding process and limits the accuracy of structural indices. Therefore, calculation of the trabecular structural indices from the HR-

pQCT images employs a hybrid approach combining the histomorphometric method and the distance transformation (DT) and ridge analysis (**Figure 2.15**). Calculation of the trabecular densitometric and structural indices from HR-pQCT images has been described and validated previously [69, 71, 73, 112, 113]. First, the bone volume fraction (BV/TV) is derived from trabecular volumetric BMD assuming the fully mineralized trabecular bone has a density of 1200 mg HA/cm^3. The mineralized phase is extracted by applying a Laplace-Hamming filter followed by a fixed global threshold, which results in binary representation of trabecular bone. A mean axis transformation is performed on the binary image of trabeculae to find trabecular ridges, followed by the distance transform (DT), where the maximal sphere is filled in the material of interest (bone or marrow space), to create a map of mean distance between ridges [114, 115]. The trabecular number (Tb.N, mm^{-1}) is calculated directly as an average distance between ridges [70, 73, 108]. Trabecular thickness (App.Tb.Th, mm) and separation (App.Tb.Sp, mm) are derived from Tb.N as App.Tb.Th = (BV/TV) / Tb.N, and App.Tb.Sp = (1 – BV/TV) / Tb.N.

Finally the standard deviation of trabecular spacing (Tb.1/N.SD, μm) is taken as a measure of heterogeneity in trabeculae distribution [115]. These trabecular structural indices are calculated for the entire trabecular compartment (the global means). The reproducibility of the trabecular structure indices obtained from *in vivo* HR-pQCT images is ≤1.5% [87].

Due to its limited resolution, the non-metric indices are not routinely assessed from HR-pQCT images as a part of standard patient analysis protocol. The triangulation (TRI) method can facilitate the assessment of the trabecular bone volume by fitting triangles on the surface and consequently tetrahedrons in the volume three-dimensionally [108] (**Figure 2.15**). The structure model index (SMI) is calculated from bone volume (BV) and surface area (BS) obtained using the TRI method: $SMI = 6 \cdot (BV \cdot dBS/dr) / BS^2$.

The mean intercept length (MIL) that is plotted as a radius from the origin at the angle of measurement generates the surface of an ellipsoid in three-dimension. A ratio of maximum to minimum eigenvalues of the MIL tensor is used to calculate degree of anisotropy (DA) [110, 116, 117]. Connectivity density is derived from the Euler characteristic of a three-dimensional structure [109].

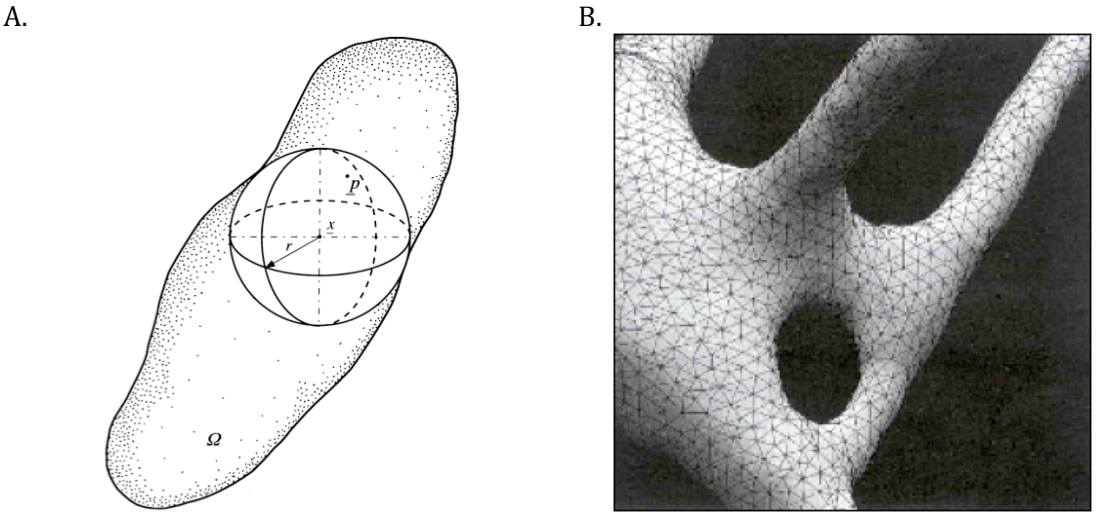

Figure 2.15 Conceptual drawing of a) distance transformation (DT) by fitting the maximal sphere to measure the local trabecular thickness [114] and b) triangulation (TRI) method by fitting triangles on the surface of a trabecula [108].

As these features are interrelated, the intricate structure of trabecular bone can only be described collectively. For instance, the predictive power for the mechanical property often improves by combining multiple trabecular structure indices in a model [66, 101, 116, 118], especially in the case of low BV/TV [119] which is typical for osteoporotic bone.

IV. Artifacts associated with *in vivo* imaging of trabecular bone using HR-pQCT

Errors caused by various associated artifacts must be thoroughly characterized for accurate and reproducible characterization of trabecular bone structure from HR-pQCT images. Three artifacts commonly seen in computed tomography include partial volume

effects, motion artifacts, and beam hardening effects. Although it is not a source of error per se, averaging over the volume of interest poses a problem. For instance, difference between thicker trabeculae along the direction of external load and thinner orthogonal trabeculae is averaged.

Partial volume effect

Although a nominal resolution of 82 μm can be achieved using HR-pQCT for noninvasive *in vivo* assessment of trabecular bone, that resolution is still inusfficient – the average human trabeculae only spans 1-2 voxels at this resolution, giving rise to significant partial volume effects (**Figure 2.16**) that confound the thresholding process and limit the accuracy of structure indices calculation. The degree of error introduced to metric structural indices by the partial volume effect at this resolution has been previously quantified [120, 121]. The partial volume effect is particularly severe for trabeculae with low BV/TV (< 0.15) [122], which is frequently observed for individuals with osteoporosis. In such a case, the variance in the measurement increases [123] and thresholding becomes critical [122, 124] as a voxel taken away by thresholding accounts for a relatively large percentage of the volume [122]. As a result, the accuracy of Tb.Th is compromised, while Tb.N and Tb.Sp remain relatively unaffected at limited resolutions [120, 122, 125, 126]. Chapter 2 addresses the effect of resolution on non-metric indices.

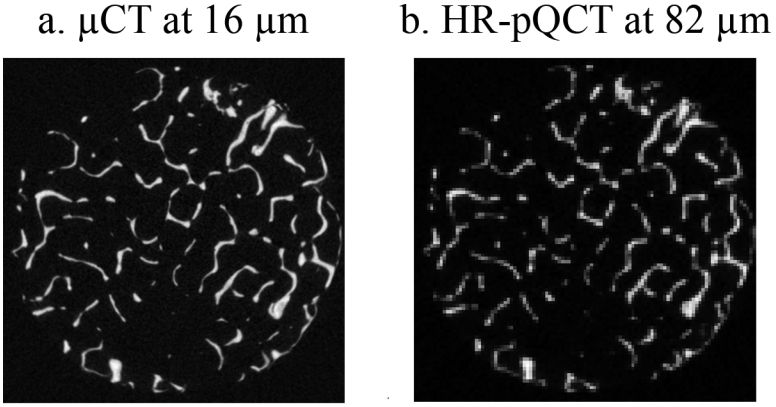

Figure 2.16 With the limited nominal resolution of HR-pQCT at 82 μm, the grayscale image of human distal tibia (b) is highly pixilated due to the severe partial volume averaging effect compared to the matching section imaged using μCT at the nominal resolution of 16 μm (a). (Adapted from Sode et al 2008 [67])

Motion artifacts

Motion artifacts have been a problem for image acquisition and processing for all radiological devices on live subjects, from cardiograms [127, 128] to computer-assisted surgery [129]. Although it takes less than 3 minutes to acquire HR-pQCT image during the standard patient protocol, motion artifacts are commonly seen in the images, particularly at the radius [71] (**Figure 2.17**). The resulting image quality is severely compromised, which confounds the accuracy and reproducibility of measurements, especially for structural indices of trabecular bone [71]. These indices are suspected to be more prone to error due to motion artifacts compared to densitometric indices [71], as trabeculae only span 1-3 pixels and subject to partial volume averaging and thresholding. The degree of error introduced to HR-pQCT-obtained density, cortical geometry, and trabecular structure measurements due to motion artifacts, however, has not been quantified. Such information is useful for more realistic calculation for the statistical power of a study design. It also contributes in establishing a standardized procedure for handling HR-pQCT images with motion artifacts that are based on empirical data. The lack of a standardized procedure also prohibits comprehensive comparisons across studies.

When severe motion artifacts are detected, it is often necessary to repeat the image acquisition, exposing the subject to more radiation. The manufacturer has provided a grading system according to the apparent severity of the motion artifact in the image. While this system can distinguish the worst image quality (grade 4 or 5) from the best quality (grade 1 or 2), the discriminatory power is not linear or reliable [130].

In chapter 3, the motion artifact in the *in vivo* HR-pQCT images of the distal radius and tibia is quantified using three similarity measures to compare the parallelized projection images at 0° and at 180°.

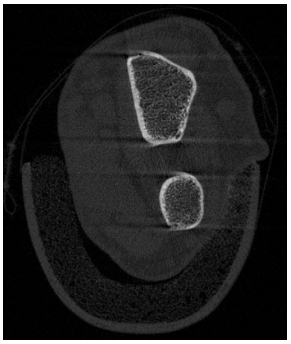

Figure 2.17 (left) Representative reconstructed HR-pQCT image of the distal radius with severe motion artifacts. Characteristic horizontal streak is visible, the cortex is disrupted, and trabeculae are blurred.

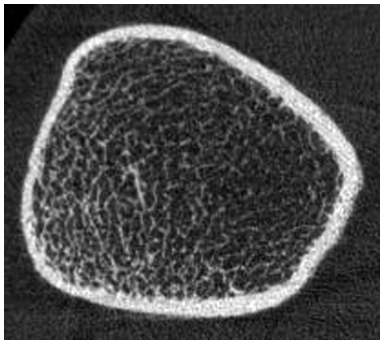

Figure 2.18 (right) Representative grayscale image of the human distal tibia showing the heterogeneous nature of trabecular structure and its distribution across the cross-section.

Beam Hardening

Beam hardening (BH) is an artifact arising from the polychromatic nature of an x-ray beam. It is caused by the lower energy x-rays being preferentially attenuated by dense (such as bone) and/or thick material, thereby skewing the penetrated x-ray beam towards higher energy. It results in an inaccuracy in attenuation profile with a characteristic cupping shape – higher attenuation at the edges but depressed at the center of a profile of a homogeneous object with uniform thickness [131]. It has the effect of compromising the accuracies of density measurement and thresholding. To account for the artifact, filters on the beam as well as correction algorithms during reconstruction are implemented in CT systems, including HR-pQCT. These countermeasures, however, only reduce the effect but cannot eliminate it completely [64, 132-135]. In HR-pQCT, Sekhon et al [64] found that error in trabecular volumetric BMD depends on both cortical thickness and apparent trabecular density, and can be up to 41% at radius and the tibia, respectively. Overestimation in BV/TV and Tb.Th results. Artifacts caused by beam hardening are not within the scope of this dissertation.

A. With BH effect **B.** With BH correction **C.** Line profiles

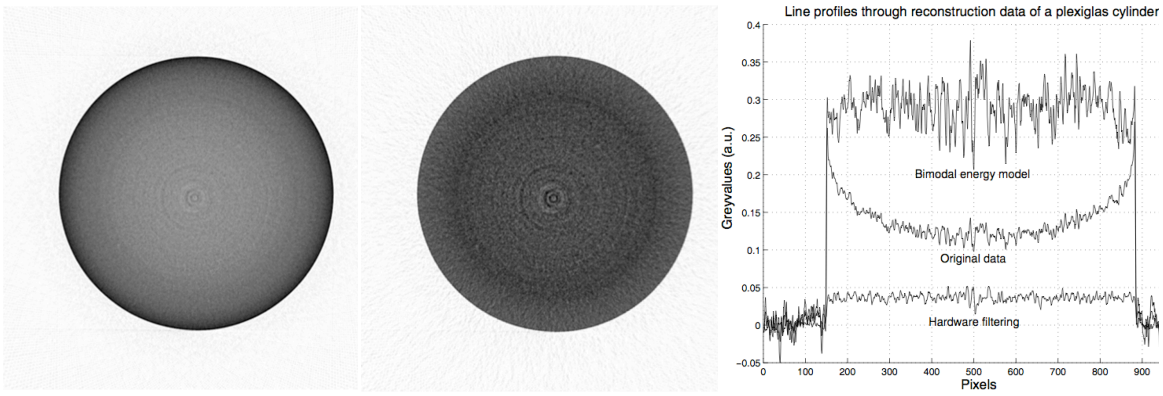

D. Streaking artifact

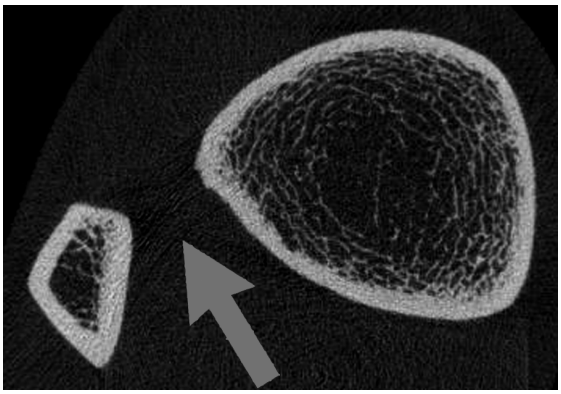

Figure 2.19 The representative grayscale images of a cylinder with uniform density with (A) and without (B) beam hardening artifacts (corrected by a BH correction algorithm). The corresponding line profiles (C) show characteristic cupping effect at the center (Adapted from Van de Casteel, 2004 [136]). As the x-ray beams pass through the thick cortex parallel to the streaks, the low energy x-rays were preferentially attenuated. Darker streaks between the tibia and fibula resulted (D).

Global analysis

Trabecular density and structure can vary substantially across axial sections of the distal radius and tibia (**Figure 2.18**) [137, 138]. The indices describing trabecular bone structure calculated from HR-pQCT images are conventionally reported as average values for the entire trabecular compartment of interest, however. This global analysis therefore obscures the inherent regional differences in trabecular compartment. A standard deviation only indicates the degree to which a structure index is spatially heterogeneous for the entire trabecular region but does not characterize the variation from subregion to subregion. Therefore, a procedure to account for this regional variation may provide complementary information to the global analysis. In addition, it may reveal the information related to the underlying biomechanical conditions refleted by the intrinsic structural heterogeneity of trabecular bone. In chapter 4, the regional analysis is applied to a normative dataset to reveal

substantial regional differences that are obscured by the conventional approach. In Chapter 5, regional analysis is applied to a clinical dataset to further demonstrate its utility in revealing the treatment effect regionally.

REFERENCES

[1] Taichman RS. Blood and bone: two tissues whose fates are intertwined to create the hematopoietic stem-cell niche. Blood 2005; 105: 2631-9.

[2] Nervi B, Link DC, DiPersio JF. Cytokines and hematopoietic stem cell mobilization. J Cell Biochem 2006; 99: 690-705.

[3] Weidt C, Niggemann B, Kasenda B, Drell TL, Zanker KS, Dittmar T. Stem cell migration: a quintessential stepping stone to successful therapy. Curr Stem Cell Res Ther 2007; 2: 89-103.

[4] Favus MJ, American Society for Bone and Mineral Research. Primer on the metabolic bone diseases and disorders of mineral metabolism. 5th ed. Washington, DC: American Society for Bone and Mineral Research; 2003.

[5] Rosen CJ, American Society for Bone and Mineral Research. Primer on the metabolic bone diseases and disorders of mineral metabolism. 7th ed. Washington, D.C.: American Society for Bone and Mineral Research; 2009.

[6] Bell GH, Dunbar O, Beck JS, Gibb A. Variations in strength of vertebrae with age and their relation to osteoporosis. Calcif Tissue Res 1967; 1: 75-86.

[7] Ebbesen EN, Thomsen JS, Beck-Nielsen H, Nepper-Rasmussen HJ, Mosekilde L. Lumbar vertebral body compressive strength evaluated by dual-energy X-ray absorptiometry, quantitative computed tomography, and ashing. Bone 1999; 25: 713-24.

[8] Keller TS. Predicting the compressive mechanical behavior of bone. J Biomech 1994; 27: 1159-68.

[9] Mosekilde L, Danielsen CC. Biomechanical competence of vertebral trabecular bone in relation to ash density and age in normal individuals. Bone 1987; 8: 79-85.

[10] Weaver JK, Chalmers J. Cancellous bone: its strength and changes with aging and an evaluation of some methods for measuring its mineral content. J Bone Joint Surg Am 1966; 48: 289-98.

[11] Hernandez CJ, Beaupre GS, Keller TS, Carter DR. The influence of bone volume fraction and ash fraction on bone strength and modulus. Bone 2001; 29: 74-8.

[12] Viguet-Carrin S, Garnero P, Delmas PD. The role of collagen in bone strength. Osteoporos Int 2006; 17: 319-36.

[13] Buehler MJ. Nature designs tough collagen: explaining the nanostructure of collagen fibrils. Proc Natl Acad Sci U S A 2006; 103: 12285-90.

[14] Martin RB, Ishida J. The relative effects of collagen fiber orientation, porosity, density, and mineralization on bone strength. J Biomech 1989; 22: 419-26.

[15] Timmins PA, Wall JC. Bone water. Calcif Tissue Res 1977; 23: 1-5.

[16] Wehrli FW, Fernandez-Seara MA. Nuclear magnetic resonance studies of bone water. Ann Biomed Eng 2005; 33: 79-86.

[17] Wilson EE, Awonusi A, Morris MD, Kohn DH, Tecklenburg MM, Beck LW. Three structural roles for water in bone observed by solid-state NMR. Biophys J 2006; 90: 3722-31.

[18] Nordin M, Frankel VH. Basic biomechanics of the musculoskeletal system. 2nd ed ed. Philadelphia: Lea & Febiger; 1989.

[19] Gray H, Lewis WH. Anatomy of the human body. In. 20th ed. New York: Bartleby.com; 2000.

[20] Hildebrand T, Laib A, Muller R, Dequeker J, Ruegsegger P. Direct three-dimensional morphometric analysis of human cancellous bone: microstructural data from spine, femur, iliac crest, and calcaneus. J Bone Miner Res 1999; 14: 1167-74.

[21] Parfitt AM, Mathews CH, Villanueva AR, Kleerekoper M, Frame B, Rao DS. Relationships between surface, volume, and thickness of iliac trabecular bone in aging and in osteoporosis. Implications for the microanatomic and cellular mechanisms of bone loss. J Clin Invest 1983; 72: 1396-409.

[22] Frost HM. Bone biodynamics. 1st ed. Boston,: Little; 1964.

[23] Carter DR, Caler WE. Cycle-dependent and time-dependent bone fracture with repeated loading. J Biomech Eng 1983; 105: 166-70.

[24] Dieter GE. Mechanical metallurgy. 3rd ed ed. New York: McGraw-Hill; 1986.

[25] Carter DR, Spengler DM. Mechanical properties and composition of cortical bone. Clin Orthop Relat Res 1978: 192-217.

[26] Turner CH, Rho J, Takano Y, Tsui TY, Pharr GM. The elastic properties of trabecular and cortical bone tissues are similar: results from two microscopic measurement techniques. J Biomech 1999; 32: 437-41.

[27] Ashman RB, Cowin SC, Van Buskirk WC, Rice JC. A continuous wave technique for the measurement of the elastic properties of cortical bone. J Biomech 1984; 17: 349-61.

[28] Reilly DT, Burstein AH. The elastic and ultimate properties of compact bone tissue. J Biomech 1975; 8: 393-405.

[29] Wendlova J. Bone quality. Elasticity and strength. Bratisl Lek Listy 2008; 109: 383-6.

[30] Boyle WJ, Simonet WS, Lacey DL. Osteoclast differentiation and activation. Nature 2003; 423: 337-42.

[31] Burger EH, Klein-Nulend J, Smit TH. Strain-derived canalicular fluid flow regulates osteoclast activity in a remodelling osteon--a proposal. J Biomech 2003; 36: 1453-9.

[32] Huiskes R, Ruimerman R, van Lenthe GH, Janssen JD. Effects of mechanical forces on maintenance and adaptation of form in trabecular bone. Nature 2000; 405: 704-6.

[33] Mori S, Burr DB. Increased intracortical remodeling following fatigue damage. Bone 1993; 14: 103-9.

[34] Eriksen EF, Axelrod DW, Melsen F. Bone histomorphometry. New York: Raven Press; 1994.

[35] Riggs BL, Melton Iii LJ, 3rd, Robb RA, Camp JJ, Atkinson EJ, Peterson JM, Rouleau PA, McCollough CH, Bouxsein ML, Khosla S. Population-based study of age and sex differences in bone volumetric density, size, geometry, and structure at different skeletal sites. J Bone Miner Res 2004; 19: 1945-54.

[36] Riggs BL, Melton LJ, Robb RA, Camp JJ, Atkinson EJ, McDaniel L, Amin S, Rouleau PA, Khosla S. A population-based assessment of rates of bone loss at multiple skeletal sites: evidence for substantial trabecular bone loss in young adult women and men. J Bone Miner Res 2008; 23: 205-14.

[37] Burr DB, Turner CH, Naick P, Forwood MR, Ambrosius W, Hasan MS, Pidaparti R. Does microdamage accumulation affect the mechanical properties of bone? J Biomech 1998; 31: 337-45.

[38] Davison KS, Siminoski K, Adachi JD, Hanley DA, Goltzman D, Hodsman AB, Josse R, Kaiser S, Olszynski WP, Papaioannou A, Ste-Marie LG, Kendler DL, Tenenhouse A, Brown JP. Bone strength: the whole is greater than the sum of its parts. Semin Arthritis Rheum 2006; 36: 22-31.

[39] Currey JD. Bones : structure and mechanics. Princeton, NJ: Princeton University Press; 2002.

[40] Currey JD, Brear K, Zioupos P. The effects of ageing and changes in mineral content in degrading the toughness of human femora. J Biomech 1996; 29: 257-60.

[41] Wainwright SA. Mechanical design in organisms. London: Edward Arnold; 1976.

[42] McCalden RW, McGeough JA, Barker MB, Court-Brown CM. Age-related changes in the tensile properties of cortical bone. The relative importance of changes in porosity, mineralization, and microstructure. J Bone Joint Surg Am 1993; 75: 1193-205.

[43] McCalden RW, McGeough JA, Court-Brown CM. Age-related changes in the compressive strength of cancellous bone. The relative importance of changes in density and trabecular architecture. J Bone Joint Surg Am 1997; 79: 421-7.

[44] Macdonald HM, Nishiyama KK, Kang J, Hanley DA, Boyd SK. Age-related patterns of trabecular and cortical bone loss differ between sexes and skeletal sites: A population-based HR-pQCT study. J Bone Miner Res 2010.

[45] Burghardt AJ, Kazakia GJ, Ramachandran S, Link TM, Majumdar S. Age- and gender-related differences in the geometric properties and biomechanical significance of intracortical porosity in the distal radius and tibia. J Bone Miner Res 2009; 25: 983-93.

[46] Khosla S, Riggs BL, Atkinson EJ, Oberg AL, McDaniel LJ, Holets M, Peterson JM, Melton LJ, 3rd. Effects of sex and age on bone microstructure at the ultradistal radius: a population-based noninvasive *in vivo* assessment. J Bone Miner Res 2006; 21: 124-31.

[47] Lauretani F, Bandinelli S, Griswold ME, Maggio M, Semba R, Guralnik JM, Ferrucci L. Longitudinal changes in BMD and bone geometry in a population-based study. J Bone Miner Res 2008; 23: 400-8.

[48] Macdonald HM, Cooper DM, McKay HA. Anterior-posterior bending strength at the tibial shaft increases with physical activity in boys: evidence for non-uniform geometric adaptation. Osteoporos Int 2009; 20: 61-70.

[49] Aaron JE, Makins NB, Sagreiya K. The microanatomy of trabecular bone loss in normal aging men and women. Clin Orthop Relat Res 1987: 260-71.

[50] Mosekilde L. Consequences of the remodelling process for vertebral trabecular bone structure: a scanning electron microscopy study (uncoupling of unloaded structures). Bone Miner 1990; 10: 13-35.

[51] Mosekilde L. Normal age-related changes in bone mass, structure, and strength--consequences of the remodelling process. Dan Med Bull 1993; 40: 65-83.

[52] Mosekilde L, Ebbesen EN, Tornvig L, Thomsen JS. Trabecular bone structure and strength - remodelling and repair. J Musculoskelet Neuronal Interact 2000; 1: 25-30.

[53] Guo XE, Kim CH. Mechanical consequence of trabecular bone loss and its treatment: a three-dimensional model simulation. Bone 2002; 30: 404-11.

[54] Silva MJ, Gibson LJ. Modeling the mechanical behavior of vertebral trabecular bone: effects of age-related changes in microstructure. Bone 1997; 21: 191-9.

[55] Song Y, Liebschner MA, Gunaratne GH. A study of age-related architectural changes that are most damaging to bones. Biophys J 2004; 87: 3642-7.

[56] Khosla S, Melton LJ, 3rd, Achenbach SJ, Oberg AL, Riggs BL. Hormonal and biochemical determinants of trabecular microstructure at the ultradistal radius in women and men. J Clin Endocrinol Metab 2006; 91: 885-91.

[57] Manolagas SC. Birth and death of bone cells: basic regulatory mechanisms and implications for the pathogenesis and treatment of osteoporosis. Endocr Rev 2000; 21: 115-37.

[58] Bouxsein ML, Melton LJ, 3rd, Riggs BL, Muller J, Atkinson EJ, Oberg AL, Robb RA, Camp JJ, Rouleau PA, McCollough CH, Khosla S. Age- and sex-specific differences in the factor of risk for vertebral fracture: a population-based study using QCT. J Bone Miner Res 2006; 21: 1475-82.

[59] Keaveny TM, Morgan EF, Niebur GL, Yeh OC. Biomechanics of trabecular bone. Annu Rev Biomed Eng 2001; 3: 307-33.

[60] Radiation Exposure in X-ray Examinations. In: RadiologyInfo: Radiological Society of North America, Inc.; 2007. p. 1-4.

[61] Radiation Exposure from Medical Exams and Procedures. In: Health Physics Society Specialists in Radiation Safety Fact Sheet. McLean, VA: The Health Physics Society; 2010. p. 1-4.

[62] Isherwood I, Rutherford RA, Pullan BR, Adams PH. Bone-mineral estimation by computer-assisted transverse axial tomography. Lancet 1976; 2: 712-5.

[63] Ruegsegger P, Elsasser U, Anliker M, Gnehm H, Kind H, Prader A. Quantification of bone mineralization using computed tomography. Radiology 1976; 121: 93-7.

[64] Sekhon K, Kazakia GJ, Burghardt AJ, Hermannsson B, Majumdar S. Accuracy of volumetric bone mineral density measurement in high-resolution peripheral quantitative computed tomography. Bone 2009; 45: 473-9.

[65] Liu XS, Zhang XH, Sekhon KK, Adam MF, McMahon DJ, Bilezikian JP, Shane E, Guo XE. High-Resolution Peripheral Quantitative Computed Tomography Can Assess Microstructural and Mechanical Properties of Human Distal Tibial Bone. J Bone Miner Res 2009.

[66] MacNeil JA, Boyd SK. Accuracy of high-resolution peripheral quantitative computed tomography for measurement of bone quality. Med Eng Phys 2007; 29: 1096-105.

[67] Sode M, Burghardt AJ, Nissenson RA, Majumdar S. Resolution dependence of the non-metric trabecular structure indices. Bone 2008; 42: 728-36.

[68] Varga P, Zysset PK. Assessment of volume fraction and fabric in the distal radius using HR-pQCT. Bone 2009; 45: 909-17.

[69] Boutroy S, Bouxsein ML, Munoz F, Delmas PD. *In vivo* assessment of trabecular bone microarchitecture by high-resolution peripheral quantitative computed tomography. J Clin Endocrinol Metab 2005; 90: 6508-15.

[70] Laib A, Hildebrand T, Hauselmann HJ, Ruegsegger P. Ridge number density: a new parameter for *in vivo* bone structure analysis. Bone 1997; 21: 541-6.

[71] MacNeil JA, Boyd SK. Improved reproducibility of high-resolution peripheral quantitative computed tomography for measurement of bone quality. Med Eng Phys 2008; 30: 792-9.

[72] Mueller TL, Stauber M, Kohler T, Eckstein F, Muller R, van Lenthe GH. Non-invasive bone competence analysis by high-resolution pQCT: an in vitro reproducibility study on structural and mechanical properties at the human radius. Bone 2009; 44: 364-71.

[73] Muller R, Hildebrand T, Hauselmann HJ, Ruegsegger P. *In vivo* reproducibility of three-dimensional structural properties of noninvasive bone biopsies using 3D-pQCT. J Bone Miner Res 1996; 11: 1745-50.

[74] Macneil JA, Boyd SK. Bone strength at the distal radius can be estimated from high-resolution peripheral quantitative computed tomography and the finite element method. Bone 2008; 42: 1203-13.

[75] Varga P, Baumbach S, Pahr D, Zysset PK. Validation of an anatomy specific finite element model of Colles' fracture. J Biomech 2009; 42: 1726-31.

[76] Dalzell N, Kaptoge S, Morris N, Berthier A, Koller B, Braak L, van Rietbergen B, Reeve J. Bone micro-architecture and determinants of strength in the radius and tibia: age-related changes in a population-based study of normal adults measured with high-resolution pQCT. Osteoporos Int 2009; 20: 1683-94.

[77] Kirmani S, Christen D, van Lenthe GH, Fischer PR, Bouxsein ML, McCready LK, Melton LJ, 3rd, Riggs BL, Amin S, Muller R, Khosla S. Bone structure at the distal radius during adolescent growth. J Bone Miner Res 2009; 24: 1033-42.

[78] Mueller TL, van Lenthe GH, Stauber M, Gratzke C, Eckstein F, Muller R. Regional, age and gender differences in architectural measures of bone quality and their correlation to bone mechanical competence in the human radius of an elderly population. Bone 2009; 45: 882-91.

[79] Nishiyama KK, Macdonald HM, Buie HR, Hanley DA, Boyd SK. Postmenopausal women with osteopenia have higher cortical porosity and thinner cortices at the distal radius and tibia than women with normal aBMD: an *in vivo* HR-pQCT study. J Bone Miner Res 2010; 25: 882-90.

[80] Burghardt AJ, Kazakia GJ, Sode M, de Papp AE, Link TM, Majumdar S. A longitudinal HR-pQCT study of alendronate treatment in post-menopausal women with low bone

density: Relations between density, cortical and trabecular micro-architecture, biomechanics, and bone turnover. J Bone Miner Res 2010.

[81] Kazakia GJ, Hyun B, Burghardt AJ, Krug R, Newitt DC, de Papp AE, Link TM, Majumdar S. *In vivo* determination of bone structure in postmenopausal women: a comparison of HR-pQCT and high-field MR imaging. J Bone Miner Res 2008; 23: 463-74.

[82] Laib A, Hammerle S, Koller B. A new 100 µm resolution scanner for *in vivo* 3D-CT of the human forearm and lower leg. In: 16th International Bone Densitometry Workshop. Annecy, France; 2004.

[83] Osteoporosis prevention, diagnosis, and therapy. NIH Consens Statement 2000; 17: 1-45.

[84] Bjarnason K, Hassager C, Svendsen OL, Stang H, Christiansen C. Anteroposterior and lateral spinal DXA for the assessment of vertebral body strength: comparison with hip and forearm measurement. Osteoporos Int 1996; 6: 37-42.

[85] Lochmuller EM, Eckstein F, Kaiser D, Zeller JB, Landgraf J, Putz R, Steldinger R. Prediction of vertebral failure loads from spinal and femoral dual-energy X-ray absorptiometry, and calcaneal ultrasound: an in situ analysis with intact soft tissues. Bone 1998; 23: 417-24.

[86] Myers BS, Arbogast KB, Lobaugh B, Harper KD, Richardson WJ, Drezner MK. Improved assessment of lumbar vertebral body strength using supine lateral dual-energy x-ray absorptiometry. J Bone Miner Res 1994; 9: 687-93.

[87] Deng HW, Xu FH, Davies KM, Heaney R, Recker RR. Differences in bone mineral density, bone mineral content, and bone areal size in fracturing and non-fracturing women, and their interrelationships at the spine and hip. J Bone Miner Metab 2002; 20: 358-66.

[88] Meunier PJ, Boivin G. Bone mineral density reflects bone mass but also the degree of mineralization of bone: therapeutic implications. Bone 1997; 21: 373-7.

[89] Darelid A, Ohlsson C, Rudang R, Kindblom JM, Mellstrom D, Lorentzon M. Trabecular volumetric bone mineral density is associated with previous fracture during childhood and adolescence in males: the GOOD study. J Bone Miner Res 2010; 25: 537-44.

[90] Mackey DC, Eby JG, Harris F, Taaffe DR, Cauley JA, Tylavsky FA, Harris TB, Lang TF, Cummings SR. Prediction of clinical non-spine fractures in older black and white men and women with volumetric BMD of the spine and areal BMD of the hip: the Health, Aging, and Body Composition Study*. J Bone Miner Res 2007; 22: 1862-8.

[91] Stein EM, Liu XS, Nickolas TL, Cohen A, Thomas V, McMahon DJ, Zhang C, Yin PT, Cosman F, Nieves J, Guo XE, Shane E. Abnormal microarchitecture and reduced stiffness at the radius and tibia in postmenopausal women with fractures. J Bone Miner Res 2010.

[92] Cummings SR, Nevitt MC, Browner WS, Stone K, Fox KM, Ensrud KE, Cauley J, Black D, Vogt TM. Risk factors for hip fracture in white women. Study of Osteoporotic Fractures Research Group. N Engl J Med 1995; 332: 767-73.

[93] Boutroy S, Van Rietbergen B, Sornay-Rendu E, Munoz F, Bouxsein ML, Delmas PD. Finite element analysis based on *in vivo* HR-pQCT images of the distal radius is

associated with wrist fracture in postmenopausal women. J Bone Miner Res 2008; 23: 392-9.

[94] Melton LJ, 3rd, Riggs BL, van Lenthe GH, Achenbach SJ, Muller R, Bouxsein ML, Amin S, Atkinson EJ, Khosla S. Contribution of *in vivo* structural measurements and load/strength ratios to the determination of forearm fracture risk in postmenopausal women. J Bone Miner Res 2007; 22: 1442-8.

[95] Pistoia W, van Rietbergen B, Ruegsegger P. Mechanical consequences of different scenarios for simulated bone atrophy and recovery in the distal radius. Bone 2003; 33: 937-45.

[96] MacNeil JA, Boyd SK. Load distribution and the predictive power of morphological indices in the distal radius and tibia by high resolution peripheral quantitative computed tomography. Bone 2007; 41: 129-37.

[97] Mittra E, Rubin C, Gruber B, Qin YX. Evaluation of trabecular mechanical and microstructural properties in human calcaneal bone of advanced age using mechanical testing, muCT, and DXA. J Biomech 2007.

[98] Mittra E, Rubin C, Qin YX. Interrelationship of trabecular mechanical and microstructural properties in sheep trabecular bone. J Biomech 2005; 38: 1229-37.

[99] Kinney JH, Stolken JS, Smith TS, Ryaby JT, Lane NE. An orientation distribution function for trabecular bone. Bone 2005; 36: 193-201.

[100] Li M, Mosekilde L, Sogaard CH, Thomsen JS, Wronski TJ. Parathyroid hormone monotherapy and cotherapy with antiresorptive agents restore vertebral bone mass and strength in aged ovariectomized rats. Bone 1995; 16: 629-35.

[101] Mosekilde L, Danielsen CC, Gasser J. The effect on vertebral bone mass and strength of long term treatment with antiresorptive agents (estrogen and calcitonin), human parathyroid hormone-(1-38), and combination therapy, assessed in aged ovariectomized rats. Endocrinology 1994; 134: 2126-34.

[102] Ohnishi H, Nakamura T, Narusawa K, Murakami H, Abe M, Barbier A, Suzuki K. Bisphosphonate tiludronate increases bone strength by improving mass and structure in established osteopenia after ovariectomy in rats. Bone 1997; 21: 335-43.

[103] Okimoto N, Tsurukami H, Okazaki Y, Nishida S, Sakai A, Ohnishi H, Hori M, Yasukawa K, Nakamura T. Effects of a weekly injection of human parathyroid hormone (1-34) and withdrawal on bone mass, strength, and turnover in mature ovariectomized rats. Bone 1998; 22: 523-31.

[104] Ding M, Odgaard A, Linde F, Hvid I. Age-related variations in the microstructure of human tibial cancellous bone. J Orthop Res 2002; 20: 615-21.

[105] Hildebrand T, Ruegsegger P. Quantification of Bone Microarchitecture with the Structure Model Index. Comput Methods Biomech Biomed Engin 1997; 1: 15-23.

[106] Odgaard A, Gundersen HJ. Quantification of connectivity in cancellous bone, with special emphasis on 3-D reconstructions. Bone 1993; 14: 173-82.

[107] Harrigan TP, Mann RW. Characterization of microstructural anisotropy in orthotropic materials using a second rank tensor. Journal of Materials Science 1984; 19: 761-767.

[108] Ding M, Hvid I. Quantification of age-related changes in the structure model type and trabecular thickness of human tibial cancellous bone. Bone 2000; 26: 291-5.

[109] Laib A, Hauselmann HJ, Ruegsegger P. *In vivo* high resolution 3D-QCT of the human forearm. Technol Health Care 1998; 6: 329-37.

[110] Laib A, Ruegsegger P. Calibration of trabecular bone structure measurements of *in vivo* three-dimensional peripheral quantitative computed tomography with 28-microm-resolution microcomputed tomography. Bone 1999; 24: 35-9.

[111] Hildebrand T, Ruegsegger P. A new method for the model independent assessment of thickness in three-dimensional images. Journal of Microscopy 1997; 185: 67-75.

[112] Laib A, Newitt DC, Lu Y, Majumdar S. New model-independent measures of trabecular bone structure applied to *in vivo* high-resolution MR images. Osteoporos Int 2002; 13: 130-6.

[113] Goulet RW, Goldstein SA, Ciarelli MJ, Kuhn JL, Brown MB, Feldkamp LA. The relationship between the structural and orthogonal compressive properties of trabecular bone. J Biomech 1994; 27: 375-89.

[114] Odgaard A. Three-dimensional methods for quantification of cancellous bone architecture. Bone 1997; 20: 315-28.

[115] Ito M, Nishida A, Koga A, Ikeda S, Shiraishi A, Uetani M, Hayashi K, Nakamura T. Contribution of trabecular and cortical components to the mechanical properties of bone and their regulating parameters. Bone 2002; 31: 351-8.

[116] Nazarian A, Stauber M, Zurakowski D, Snyder BD, Muller R. The interaction of microstructure and volume fraction in predicting failure in cancellous bone. Bone 2006; 39: 1196-202.

[117] Kothari M, Keaveny TM, Lin JC, Newitt DC, Genant HK, Majumdar S. Impact of spatial resolution on the prediction of trabecular architecture parameters. Bone 1998; 22: 437-43.

[118] Muller R, Koller B, Hildebrand T, Laib A, Gianolini S, Ruegsegger P. Resolution dependency of microstructural properties of cancellous bone based on three-dimensional mu-tomography. Technol Health Care 1996; 4: 113-9.

[119] Hara T, Tanck E, Homminga J, Huiskes R. The influence of microcomputed tomography threshold variations on the assessment of structural and mechanical trabecular bone properties. Bone 2002; 31: 107-9.

[120] Kim DG, Christopherson GT, Dong XN, Fyhrie DP, Yeni YN. The effect of microcomputed tomography scanning and reconstruction voxel size on the accuracy of stereological measurements in human cancellous bone. Bone 2004; 35: 1375-82.

[121] Ding M, Odgaard A, Hvid I. Accuracy of cancellous bone volume fraction measured by micro-CT scanning. J Biomech 1999; 32: 323-6.

[122] Banse X, Devogelaer JP, Grynpas M. Patient-specific microarchitecture of vertebral cancellous bone: a peripheral quantitative computed tomographic and histological study. Bone 2002; 30: 829-35.

[123] McColl DJ, Abel RL, Spears IR, Macho GA. Automated method to measure trabecular thickness from microcomputed tomographic scans and its application. Anat Rec A Discov Mol Cell Evol Biol 2006; 288: 982-8.

[124] Horiguchi J, Fukuda H, Yamamoto H, Hirai N, Alam F, Kakizawa H, Hieda M, Tachikake T, Marukawa K, Ito K. The impact of motion artifacts on the reproducibility of repeated coronary artery calcium measurements. Eur Radiol 2007; 17: 81-6.

[125] Lu W, Parikh PJ, Hubenschmidt JP, Politte DG, Whiting BR, Bradley JD, Mutic S, Low DA. Reduction of motion blurring artifacts using respiratory gated CT in sinogram space: a quantitative evaluation. Med Phys 2005; 32: 3295-304.

[126] Marmulla R, Muhling J. The influence of computed tomography motion artifacts on computer-assisted surgery. J Oral Maxillofac Surg 2006; 64: 466-70.

[127] Pialat JB, Burghardt AJ, Sode M, Link TM, Majumdar S. Motion Artifacts in High-Resolution Peripheral Quantitative Computed-Tomography of Wrist and Ankle: Usefulness of Visual Grading to assess Image Quality. In: ASBMR 2010 Annual Meeting. Tronto, ON, Canada; 2010.

[128] Brooks RA, Di Chiro G. Beam hardening in x-ray reconstructive tomography. Phys Med Biol 1976; 21: 390-8.

[129] Fajardo RJ, Cory E, Patel ND, Nazarian A, Laib A, Manoharan RK, Schmitz JE, DeSilva JM, MacLatchy LM, Snyder BD, Bouxsein ML. Specimen size and porosity can introduce error into microCT-based tissue mineral density measurements. Bone 2009; 44: 176-84.

[130] Kazakia GJ, Burghardt AJ, Cheung S, Majumdar S. Assessment of bone tissue mineralization by conventional x-ray microcomputed tomography: comparison with synchrotron radiation microcomputed tomography and ash measurements. Med Phys 2008; 35: 3170-9.

[131] Mulder L, Koolstra JH, Van Eijden TM. Accuracy of microCT in the quantitative determination of the degree and distribution of mineralization in developing bone. Acta Radiol 2004; 45: 769-77.

[132] Mulder L, Koolstra JH, Van Eijden TM. Accuracy of MicroCT in the quantitative determination of the degree and distribution of mineralization in developing bone. Acta Radiol 2006; 47: 882-3.

[133] Van de Casteele E. Model-based approach for Beam Hardening Correction and Resolution Measurements in Microtomography. In: Physics. Antwerp, Belgium: University of Antwerp; 2004. p. 142.

[134] Lai YM, Qin L, Hung VW, Choy WY, Chan ST, Chan LW, Chan KM. Trabecular bone status in ultradistal tibia under habitual gait loading: a pQCT study in postmenopausal women. J Clin Densitom 2006; 9: 175-83.

[135] Lai YM, Qin L, Yeung HY, Lee KK, Chan KM. Regional differences in trabecular BMD and micro-architecture of weight-bearing bone under habitual gait loading--a pQCT and microCT study in human cadavers. Bone 2005; 37: 274-82.

Chapter 3 – Resolution Dependence of the Non-metric Trabecular Structure Indices

I. INTRODUCTION

Recent advances in non-invasive imaging techniques, such as high-resolution magnetic resonance imaging (HR-MRI) and peripheral quantitative computed tomography (HR-pQCT), allow *in vivo* assessment of trabecular bone structure indices. Structural indices that describe three-dimensional trabecular bone have been routinely assessed in *ex vivo* samples using images obtained by micro-computed tomography (μCT). Assessment of trabecular microstructure has been attempted using multi-detector-row computed tomography at an in-plane resolution of 250 μm and a slice thickness of 500 μm [1]. With the emergence of HR-MRI and HR-pQCT, *in vivo* nominal resolutions of approximately 150 μm in-plane with a 400-μm slice thickness and an 82-μm isotropic voxel size, can be achieved. At these resolutions, the average human trabeculae only spans 1 - 2 voxels in diameter, giving rise to significant partial volume effects that confound the thresholding process and limit the accuracy of structural indices. While the effects of resolution on conventional structure indices such as BV/TV, Tb.Th, Tb.N, and Tb.Sp has been investigated for different modalities [2-5], the effects of resolution on non-metric indices, such as SMI, Conn.D, and DA have not been rigorously evaluated. A more detailed investigation on the dependence of non-metric indices on resolution is needed to determine their applicability for *in vivo* imaging of trabecular bone structure.

The objective of this study was two-fold: 1) to characterize dependence of three non-metric indices, namely SMI, Conn.D and DA of a trabecular bone structure to the spatial

resolution of CT images, and 2) to determine their applicability for assessing trabecular bone structure to the *in vivo* imaging. To achieve the first objective, three non-metric indices were calculated for specimens with varying plate-like and rod-like structures and sizes from resampled μCT images across a range of spatial resolutions (Part 1 Simulations). To achieve the second objective, the impact of resolution on three non-metric indices was evaluated for the clinical HR-pQCT images by comparing against the μCT reference measurements (Part 2 HR-pQCT protocol).

II. MATERIALS AND METHODS

1. Simulations

To determine whether the non-metric indices of a trabecular bone are affected by the spatial resolution of CT images, the values calculated for specimens with varying plate-like and rod-like structures from resampled μCT images were compared to the reference values at a range of spatial resolution.

Specimens

To represent various trabecular structure sizes and types (i.e. spanning rod, plate, and mixed structures), the following four specimen groups were used in the simulation part of this study: bovine proximal femur and tibia, human radius, and murine proximal tibia. Seven bovine proximal femur cores and eight bovine proximal tibia cores, 8 mm in diameter and 10 mm in length, were obtained. The cores were repeatedly sonicated (Branson 2510, Branson Ultrasonic Corporation, Denbury, CT, USA) in a mild detergent (10% Terg-A-Zyme solution, Aclonox, White Plains, NY, USA) bath for defatting prior to immersion in water in preparation for imaging. Fifteen cubes from human radius with a side length of 12 mm were extracted from fifteen cadavers (eight males and seven females, aged 72.8 ± 10.8 years), 10 mm proximal to the distal endplate. The cubes were fixed with marrow intact for imaging.

Left tibiae (n = 14) from 12-week old mice were isolated and cleaned of adherent tissue. The bones were then defatted by sequential extraction in ethanol and diethyl ether using a Soxhlet apparatus and dried overnight at 90°C.

Micro-computed tomography Acquisition

The bovine proximal femur and bovine proximal tibia specimens were imaged with an isotropic voxel size of 16 μm in a commercial micro-tomography system (μCT 40, Scanco Medical AG, Bassersdorf, Switzerland). The following settings were used for acquisition: source voltage 55 kVp, tube current 144 μA, and matrix size of 1024 × 1024. The human radius and murine tibia were imaged in a μCT 20 (Scanco MedicalAG) system at voxel sizes of 34 μm and 9 μm respectively. Data acquisition was performed as described previously [6].

Analysis

For structural evaluation purposes, volumes of interest comprising trabecular bone were manually identified for each specimen. A central 5.12 mm cubic section for both bovine femur and tibia cores and an 8.8 mm cubic section for the human radius cubes were extracted from the center of each volume. The full trabecular compartment of murine tibia, defined by semi-automatically drawn contours at the endocortical boundary was used, spanning 1 mm distally from the growth plate. All subsequent image-processing steps were conducted using the Image Processing Language (IPL, Scanco Medical AG) on a dual-Alpha OpenVMS workstation (DS20E, Hewlett Packard Inc.).

To examine the effect of voxel size on SMI, Conn.D, and DA, the original grayscale images were resampled isotropically to a range of lower voxels: Human radii were resampled to isotropic voxel sizes of 34, 59, 82 and 153 μm; murine tibiae to voxel sizes of 18, 27, 36, 54 and 72 μm; and both bovine proximal femur and tibia cores to voxel sizes of 16, 34, 82, 153 μm. Representative three-dimensional images and grayscale cross-sectional

images of each specimen type are shown in **Figure 3.1** at their original resolutions and at the corresponding lowest tested resolution. The nominal resolutions of 82 μm and 153 μm are comparable to the *in vivo* in-plane resolutions of HR-pQCT imaging and clinical magnetic resonance imaging, respectively. Similarly, 72 μm is comparable to the low-end resolution mode for common *in vivo* small animal μCT.

A fixed global threshold was used to segment the bone phase prior to the structure indices calculations. A grayscale value was visually selected, so that the resulting binary image best represented the original grayscale image. This process was done on each sample group and at each resampled voxel size.

The non-metric indices and Tb.Th were obtained from the resulting binary images generated at each resampled voxel size. As described by Hildebrand and Rueggsegger [7], the SMI values were calculated from the tetrahedrons enclosed in the triangulated surface representation of the volume data. The distance transformation method, where maximal spheres are filled into the object of interest, was applied to obtain Tb.Th, Conn.D was calculated using the Conn-Euler method as described in Odgaard et al [8] and DA was calculated as the ratio of the minor and major principal components of the mean intercept length ellipsoid determined using a projected surface method [9].

The non-metric indices obtained from the images reconstructed at the original voxel size were taken as the reference values and listed in **Table 3.1**. The values obtained from the resampled images were compared to these reference values to evaluate the effect of resolution on the non-metric indices calculation. To account for differences in trabecular thickness across different species and anatomical sites, the nominal resolution was normalized by the reference Tb.Th, the group average value calculated at the reference resolution of each sample (**Table 3.1**). This relative resolution is a measure of number of

pixels assigned to an average trabecula. All results are presented in term of this relative resolution.

2. HR-pQCT Protocols

To determine the applicability of the non-metric indices for trabecular bone structure to *in vivo* imaging, the non-metric indices were calculated for trabecular bone cores of human distal tibia from the images obtained using HR-pQCT and compared to μCT reference measurements.

Specimens

Sixteen trabecular bone cores (10 mm in diameter, 15 mm in length) were obtained from the distal tibiae of 5 human donors post mortem (three males and two females, aged 62.6 ± 10.4 years). The tissue was acquired from a national tissue bank (National Disease Research Interchange, Philadelphia, PA). The cores were extracted approximately 10 mm away from the joint line, defatted and immersed in distilled water, as described above, prior to HR-pQCT and μCT imaging.

Micro-computed tomography and HR-pQCT acquisition

The human distal tibia core specimens were imaged by μCT at 16 μm resolution as described above for the bovine samples. Additionally, the samples were imaged with a clinical HR-pQCT system (XtremeCT, Scanco Medical AG, Bassersdorf, Switzerland) using the standard *in vivo* protocol described in previous patient studies [10, 11]. In short, the x-ray source potential was 60 kVp with a current of 900 μA. A 2D 3072 × 256 element CCD detector was used to acquire 750 projections at a 100 ms integration time per rotation. The 12.6 mm field of view was reconstructed across a 1536 × 1536 matrix, yielding 82 μm

voxels. The full length of each core was covered by the automatic acquisition of two adjacent image stacks, spanning 9.05 mm each.

Analysis

A concentric cylindrical volume of interest with an 8 mm diameter was manually defined for each distal tibia core sample. Representative grayscale images of human distal tibia core are shown in **Figure 3.2** at 16 μm using μCT and at 82 μm using HR-pQCT. The original grayscale μCT images of human distal tibiae were processed in the following manner: noise was reduced by applying Gaussian filter (σ = 1.0, support = 1) and the image was binarized using a visually selected, fixed global threshold described previously [12, 13]. Since resampling effectively removes high frequency noise, a smoothing step was not performed for the resampled images prior to discretization. The resulting images were then binarized in the same manner as described for the 16μm images. Calculation of the structural indices for HR-pQCT was based on the segmentation scheme provided by the manufacturer for *in vivo* analyses. A Laplace-Hamming filter was applied to the original grayscale images to provide smoothing and edge enhancement. Next, the smoothed image was normalized to a fixed maximum intensity. Finally, a fixed global threshold was used to extract the bone phase in the same manner. The SMI, Conn.D, and DA were calculated from the binary images for each of the previous cases.

3. Statistical Analysis

In the simulation study, the significance of differences in the SMI, Conn.D, and DA for each specimen with respect to the relative resolution was tested by a single-factor repeated measure analysis of variance. If significance is found, then a paired t-test was applied to isolate the significant differences against the reference value. In addition, the coefficient of determination (r^2) between values obtained at each resampled resolution and at the

reference relative resolution was calculated to measure the degree of agreement. In the HR-pQCT protocol study, the non-metric indices for human distal tibia cores obtained from the HR-pQCT images and the μCT images resampled at 82 μm were both compared to the reference values. A regression analysis was performed and the linear equations and coefficients of determination (r^2) were obtained for each case. The significance in difference was tested using a paired t-test with $\alpha = 0.05$. For the SMI, a Bland-Altman plot was assessed for qualitative comparison against the values obtained at the reference resolution.

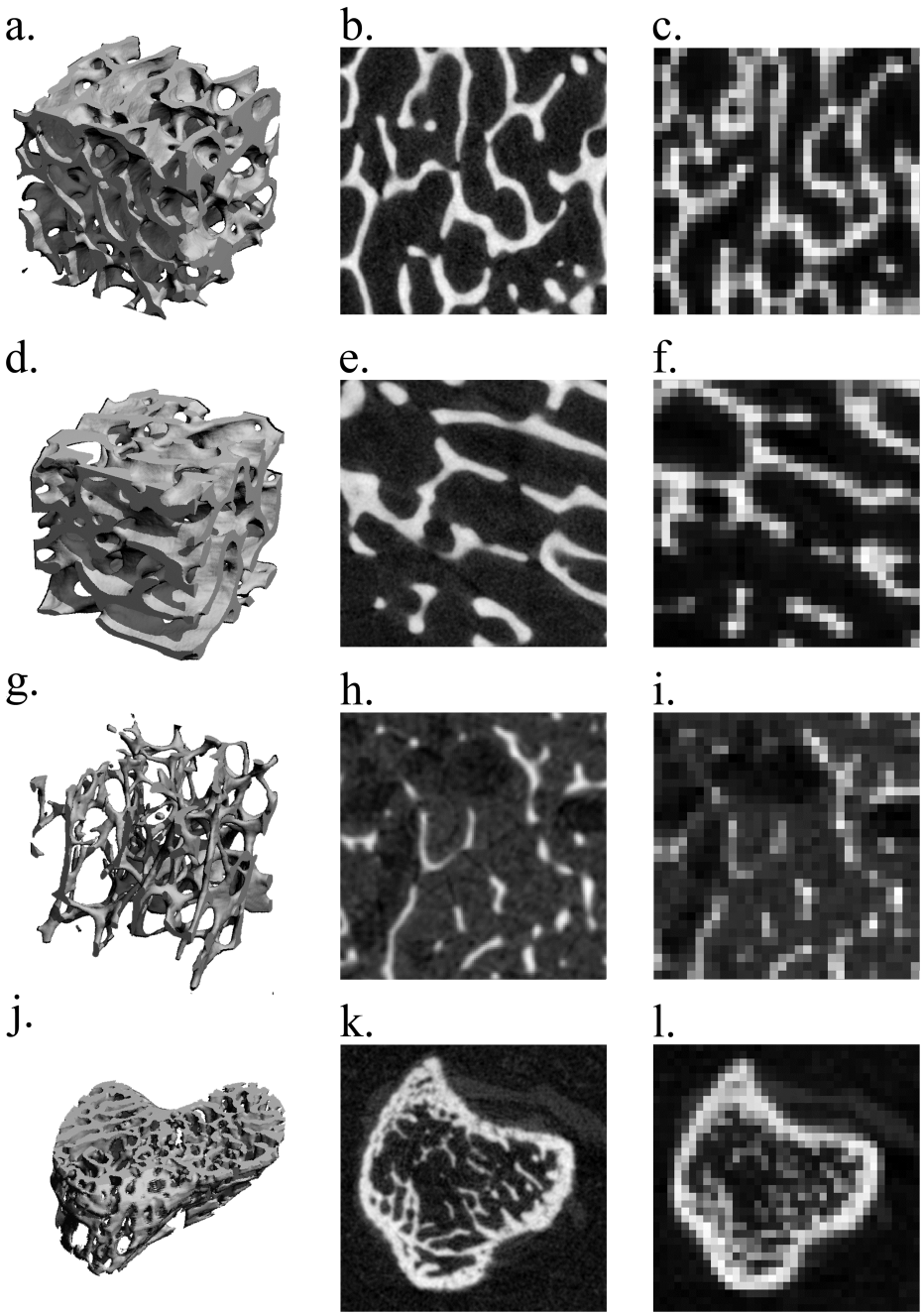

Figure 3.1 The representative μCT three-dimensional images (4 mm cubic sections (a, d, g) and a murine tibia section) and the visually matched cross-sectional images of the specimens used in this study: a bovine proximal femur and tibia (b, e) imaged at 16 μm and (c, f) resampled to 153 μm; a human distal tibia (h) imaged at 34 μm and (i) resampled to 153 μm; a murine tibia (k) imaged at 9 μm and (l) resampled to 72 μm. At the lowest resampled resolutions, images are highly pixelated, approximating the details of trabecular structure.

Table 3.1 The reference values for Tb.Th and the non-metric indices (SMI, Conn.D and DA) (mean ± SD) for each specimen used in the simulation study, calculated from the μCT images at the original (reference) resolution.

Index	Bovine prox. femur	Bovine prox. tibia	Human radius	Murine tibia
N	7	8	15	14
Original nominal resolution [μm]	16	16	34	9
Relative resolution [Pixels/Tb.Th]	11.1	12.2	4.3	6.1
Ref. Tb.Th [μm]	177.5 ± 7.2	195.9 ± 14.8	147.3 ± 18.2	54.9 ± 6.6
SMI	0.20 ± 0.36	0.76 ± 0.62	2.26 ± 0.40	1.32 ± 0.5
Conn.D [mm-3]	4.92 ± 1.59	3.48 ± 0.80	1.90 ± 0.97	246 ± 35
DA	2.12 ± 0.31	1.80 ± 0.43	1.73 ± 0.14	1.91 ± 0.1

The reference Tb.Th at the original nominal resolution was used to calculate the relative resolution.

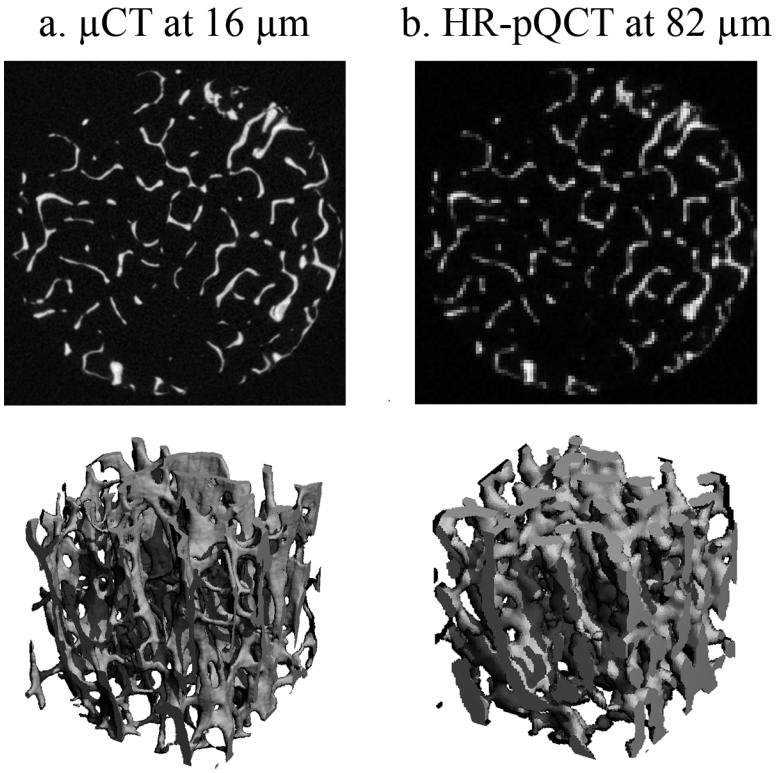

Figure 3.2 The representative visually matched grayscale cross-sectional images (top) and three-dimensional images (bottom) of human distal tibia imaged using a) μCT at 16μm, and b) HR-pQCT at 82 μm (equivalent to relative resolution of 1.73 pixels/Tb.Th). The image is highly pixelated causing severe approximation of the fine trabecular structure in the HR-pQCT image.

III. RESULTS

1. Simulations

Among the four specimen types, human radius cubes had the most rod-like trabecular structure while the bovine proximal femora had the most plate-like trabecular structure. The bovine bones (both tibiae and femora) and the human tibiae were similar in trabecular thickness; the murine tibiae were roughly one-third the size of the other specimens. As is evident in representative grayscale images shown in **Figure 3.1**, the details of the trabecular structures are lost and the images are highly pixilated at a low resolution.

The SMI increasingly deviated from the reference values in response to decreased relative resolution (**Figure 3.3**a); however, the degrees varied depending on a structure type. More rod-like structures among the tested specimens, human distal radii and murine tibiae became significantly different ($p < 0.001$) from the corresponding reference values at around 3 pixels/Tb.Th (**Figure 3.3**a). For example, at 6.1 pixels/Tb.Th, the SMI of the murine tibiae was 1.3 on average (**Table 3.1**), meaning a mixture of plate-like and rod-like structures. However, as the relative resolution degraded down to 0.8 pixel/Tb.Th, its SMI became 2.4, a more rod-like structure (**Figure 3.3**a). At this low relative resolution, the details were lost and the trabecular structure became more like clusters (**Figure 3.1**). Consequently the r^2 value for the murine tibiae dropped to 0.76 (**Figure 3.3**b).

RMANOVA and paired t-tests revealed significant decreases in Conn.D with a decrease in relative resolution for all tested specimens (all $p < 0.001$) (**Figure 3.3**c). The degree of decrease in Conn.D varied from 28% (bovine tibiae) to 76% (murine tibiae) depending on specimen type. The correlations to the reference values, decreased dramatically for bovine proximal femur and murine tibia as the relative resolution decreased (Figure 3.3d).

The observed deviations of DA from the reference values ranged up to -11% (murine tibiae) (**Figure 3.3**e). The correlations to the reference values started weakening at a notably higher relative resolution than SMI (**Figure 3.3**f). For instance, although no significant deviation from the reference value was detected for murine tibiae (**Figure 3.3**e), the correlation to the reference value dropped dramatically down to $r^2 = 0.01$ (**Figure 3.3**f).

2. HR-pQCT Protocols

The non-metric indices for trabecular bone cores of human distal tibia calculated from the images at 82 μm correlated well ($r^2 > 0.75$) with the reference values obtained from the μCT images at 16 μm, whether images were resampled from the μCT images or acquired using HR-pQCT (**Table 3.2**). However, the errors in absolute values were observed (**Figure 3.4**a-c and **Table 3.2**). As observed in the simulation study, the accuracy of SMI was structure-type dependent (**Figure 3.5**) (see Discussions). Despite their excellent correlations to the reference values, the Conn.D obtained from the resample images and the HR-pQCT images were significantly underestimated ($p < 0.001$) by 16% and 31%, respectively (**Table 3.1**). Similarly, the DA obtained from the HR-pQCT images was significantly underestimated ($p < 0.001$) by 10% (**Table 3.2**).

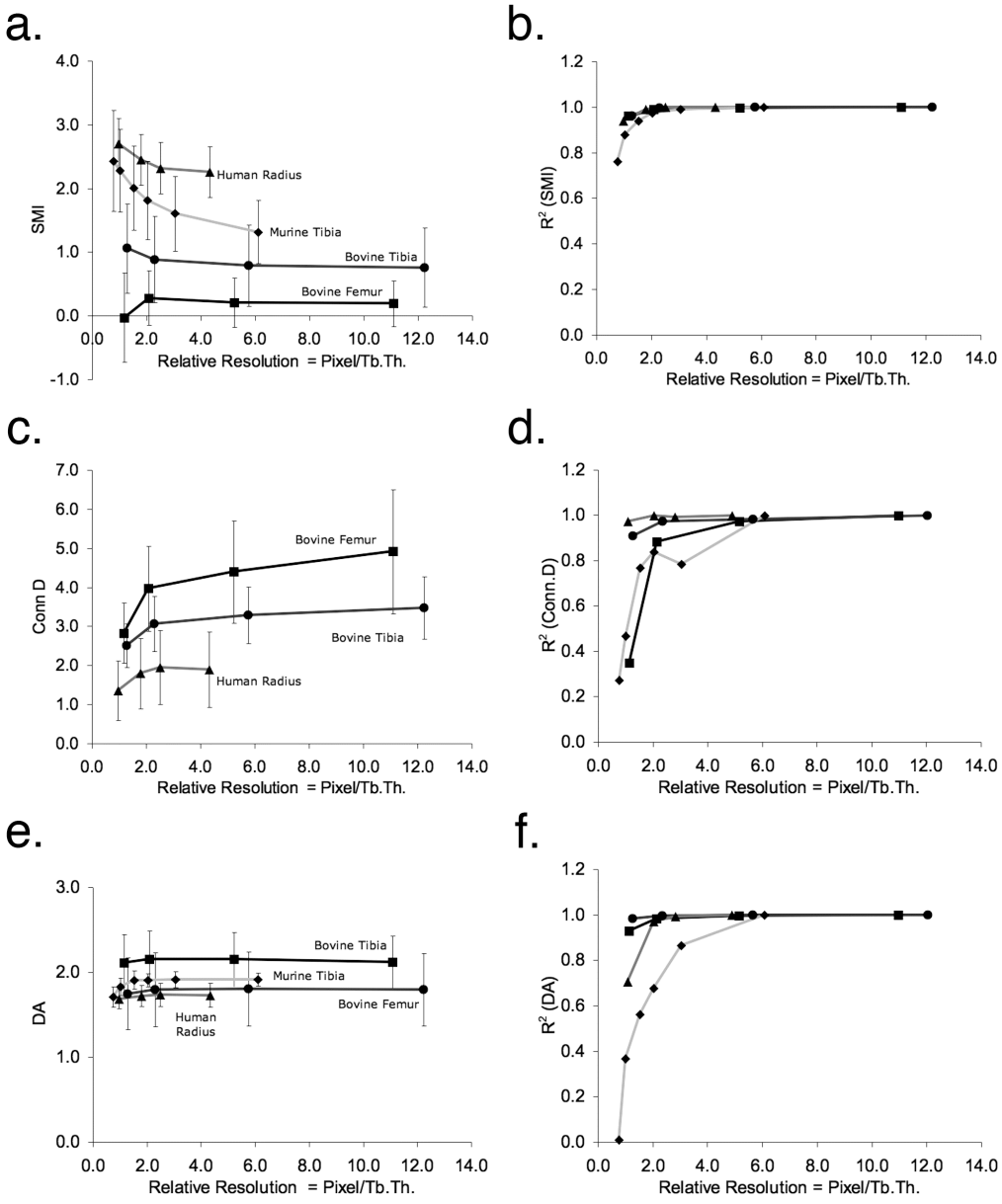

Figure 3.3 The changes in the non-metric indices (a, c, and e) and in their correlation (r^2) with the reference resolution (b, d, and f) against relative resolution. The Conn.D for murine tibia is out of the plotted range thus not shown here. The lines are simply connecting the data points.

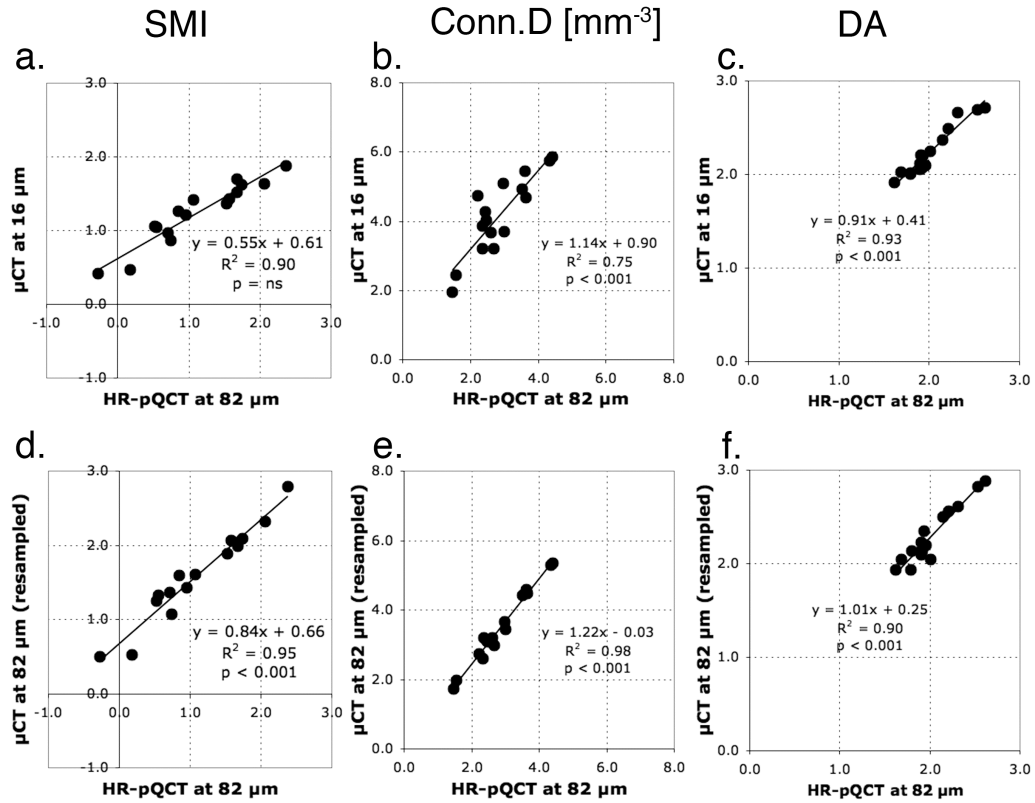

Figure 3.4 The linear regression analyses on the non-metric indices for trabecular bone core of human distal tibia to determine the correlations between the measurements calculated from two sets of images obtained differently: (a-c) the HR-pQCT images and the µCT images at reference resolution (16 µm) and (d-f) the resampled µCT images and the HR-pQCT images both at 82 µm.

Table 3.2 The average values of Tb.Th, non-metric indices (SMI, Conn.D, and DA) (mean ± SD), and the correlation coefficients (r^2) of non-metric indices for trabecular bone cores of human distal tibia obtained from the reference µCT images (16 µm), the µCT images resampled at 82 µm, and the HR-pQCT images acquired at 82 µm.

Index	Mean ± SD			r^2		
	µCT at 16 µm	µCT at 82 µm (resampled)	HR-pQCT at 82 µm	µCT at 16µm vs. µCT at 82 µm (resampled)	µCT at 16 µm vs. HR-pQCT at 82 µm	µCT at 82 (resampl vs. HR-pQCT at
Ref. Tb.Th [µm]	146.5 ± 23.1	175.7 ± 21.1	232.4 ± 22.4	-	-	-
SMI						
Over all	1.24 ± 0.42	1.61 ± 0.62	1.13 ± 0.72	0.94**	0.90^{ns}	0.95**
More plate-like (SMI ≤ 1.5)	1.04 ± 0.35	1.32 ± 0.49	0.77 ± 0.54	0.93**	0.82*	0.90**
More rod-like (SMI > 1.5)	1.67 ± 0.13	2.24 ± 0.33	1.92 ± 0.31	0.73*	0.60^{ns}	0.97**
Conn.D [mm^{-3}]	4.16 ± 1.14	3.48 ± 1.08	2.87 ± 0.87	0.81**	0.75**	0.98**
DA	2.24 ± 0.27	2.28 ± 0.30	2.02 ± 0.28	0.89^{ns}	0.93**	0.90**

The reference Tb.Th was used to calculate the relative resolution.
* $p < 0.01$; ** $p < 0.001$; ^{ns} not significant ($p > 0.05$)

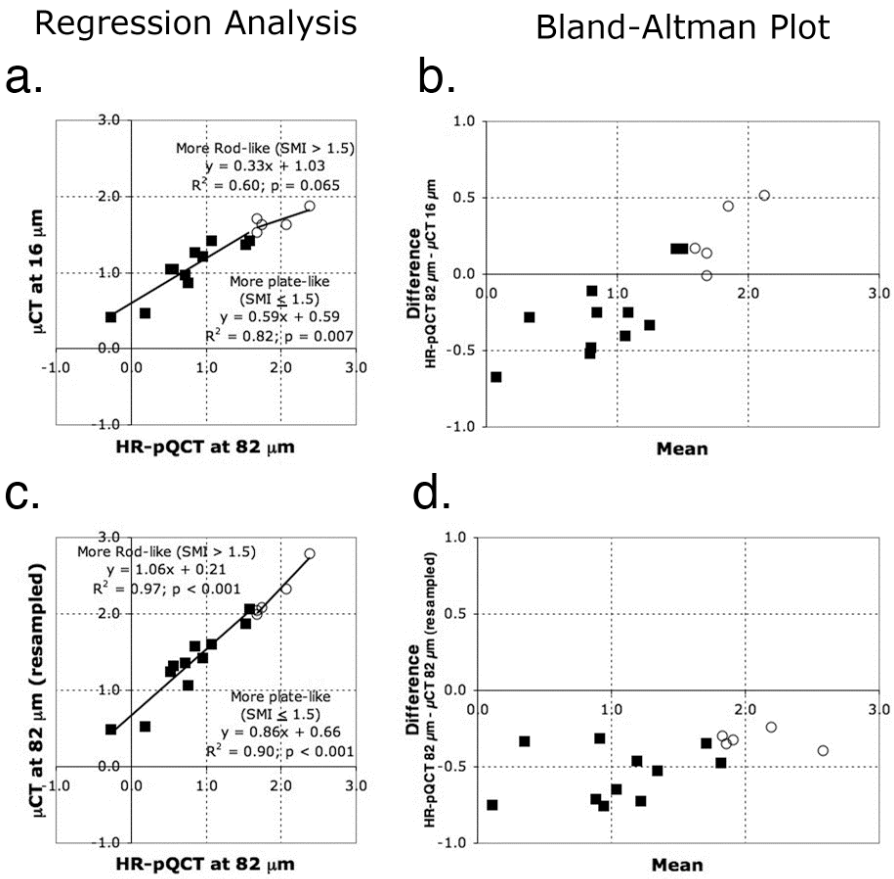

Figure 3.5 The linear regression analyses and the Bland-Altman plots on the SMI for trabecular bone core of human distal tibia calculated from two sets of images obtained differently: (a-b) The HR-pQCT images and the μCT images at reference resolution (16 μm) and (c-d) the resampled μCT images and the HR-pQCT images both at 82 μm. The measurements are grouped by the structure type at threshold SMI = 1.5. The predominantly plate-like structure (SMI ≤ 1.5) is represented by a filled square and the predominantly rod-like structure (SMI > 1.5) by an open circle. The linear regression analysis determines the correlations and the Bland-Altman plots qualitatively compare the measurements obtained from two datasets.

IV. DISCUSSION

In this study, we found that three non-metric indices of trabecular bone structure were affected by the spatial resolution of CT images. Specifically, the SMI values we obtained from resampled μCT images for bone specimens with a range of morphologies increasingly deviated from the reference values as the relative resolution decreased (**Figure 3.3**a), and its magnitude varied depending on the structure type, whether plate-like or rod-like. Similarly in a more clinically relevant context, the SMI of human trabecular bone from

the distal tibia obtained at the *in vivo* resolution (82 μm) was structure-type dependent: the magnitude of deviation from the reference value increased as the SMI increased (**Figure 3.5**b). Both Conn.D and DA of the specimens obtained from their resampled μCT images decreased as the relative resolution decreased (**Figure 3.3**c and e), and those of human distal tibia obtained from the HR-pQCT images were significantly lower than the corresponding μCT reference values (**Table 3.2**).

Considering the applicability of SMI to the *in vivo* imaging such as using HR-pQCT, the challenges are two-fold. First, the current *in vivo* relative resolution is limited to ~2 pixels/trabecula on average for the distal radius and tibia. Ito et al [1] reported that even with images obtained using multi-detector-row CT at a spatial resolution of 250 × 250 × 500 μm, fractured and non-fractured vertebrae were distinguishable ($p < 0.0001$). However, the in-plane relative resolution was only 1.4 pixels/Tb.Th at this resolution. Our results show that the reliability of the measurement at this relative resolution is questionable (Figure 3.3b). Therefore, we speculate that the observed discriminatory power of the SMI by Ito et al [1] is driven primarily by bone volume rather than by its true topology at this resolution. The question on the minimal relative resolution required for the reasonable accuracy and reliability of SMI is not trivial to answer as discussed here.

From the simulation study, we found that the accuracy of the SMI with respect to relative resolution is structure-type dependent: a plate-like structure is less sensitive to resolution degradation and consequent partial volume averaging than a rod-like structure is. A possible explanation for this difference lies in the definition, $SMI = (BV \cdot dBS/dr)/BS^2$. A plate-like structure has minimal change in surface curvature ($dBS/dr \approx 0$), making it robust against pixelation. On the contrary, a rod-like structure has more curved surface (high dBS/dr), as well as inherent low bone volume fraction (BV/TV) and high surface-to-volume ratio (BS/BV), together making it more prone to greater partial volume effect. As a result, a

rod-like structure is increasingly misrepresented as the relative resolution decreases (**Figure 3.1**).

Second, in a clinically relevant context, the observed structure-type dependence of SMI at a low relative resolution (particularly 1 - 2 pixels/Tb.Th achievable by HR-pQCT) implies that the errors are different not only between anatomical sites (e.g. radius and tibia) but also between two trabecular bones with different structure types at the same anatomical site. For example, although determined from the HR-pQCT images at the same resolution (82 μm), radius specimens in MacNeil and Boyd [14] were highly rod-like (SMI = 3.0 ± 0.8) and the SMI correlated poorly (r^2 = 0.075) with the reference value; on the other hand, human distal tibia in the current study had a mixture of plate-like and rod-like structures (SMI = 1.2 ± 0.4) and correlated strongly (r^2 = 0.90) with the μCT-obtained reference value (**Table 3.2**).

In addition, the difference in errors between specimens with different structure types at the same anatomical site can be a problem in clinical studies. To illustrate this inter-specimen difference of errors in the SMI at the *in vivo* resolution, human distal tibia samples were grouped by the structure type at a threshold SMI of 1.5, as seen in **Figure 3.5**. Although SMI obtained from the HR-pQCT images had no significant error compared to the reference value *overall* (**Figure 3.2**), SMI of the predominantly plate-like structure (SMI ≤ 1.5) was 26% lower than the reference value on average, while that of the predominantly rod-like structure (SMI > 1.5) was 14 % higher (**Figure 3.5**a and b). In other words, a structure type assessed by the SMI may be exaggerated beyond the true trabecular structure type when obtained from images at the *in vivo* resolution.

Although the Conn.D for trabecular bone cores of human distal tibia obtained from the HR-pQCT images at the *in vivo* resolution was significantly underestimated, it correlated well with the μCT reference value (r^2 = 0.75, $p < 0.001$) (**Table 3.2**). Hence, this result supports the

suggestion of obtaining Conn.D from the HR-pQCT images at 82 μm [14]. However, in the simulation study, the correlation with the reference value dramatically decreased with the relative resolution for some specimens (Figure 3.3d), in agreement with the previous studies [15, 16]. From these results, the resolution dependence of Conn.D may be affected by site dependent differences. In addition, Conn.D alone cannot be a measure of bone quality [17] due to its weak correlations with mechanical properties and other metrics [18]. Thus it must be used in conjunction with other metrics and micro finite element analysis [14].

Among the three tested non-metric trabecular structure indices, the DA showed no significant difference from the reference value throughout the tested relative resolutions for all specimens. In addition, the strong correlation with the reference value ($r^2 \geq 0.71$) was also maintained except for murine tibiae (Figure 3.3f). The underlying mechanism is that isotropic resampling averages equally in all directions, thereby effectively leaving the ratio constant [15]. While the DA of human distal tibiae obtained from the HR-pQCT images at the clinical *in vivo* resolution had an excellent correlation ($r^2 = 0.93$) in this study, MacNeil and Boyd [14] reported weaker correlation for human distal radii ($r^2 = 0.67$).

Two limitations in the methods used in this study are worth noting. First, even though thresholding is crucial in segmenting the bone phase for the calculation of non-metric indices, selecting an optimal threshold value is not trivial. Although commonly used, a manual threshold selection, such as the global fixed threshold method used in this study, can be increasingly subjective, especially as relative resolution decreases. As a result, non-negligible systematic errors are introduced in the structure measure calculations. An automatic, non-subjective thresholding method, however, did not relieve the challenge in selecting the optimal threshold for images at such a low relative resolution – the non-metric indices calculated from the images segmented using adaptive-iterative threshold method [19], showed similar deviation patterns from the reference values and had similar or lower

correlations to the reference values especially at a low relative resolution below 3 pixels/Tb.Th (data not shown).

Second, neither resampling μCT images at a lower resolution nor *ex vivo* imaging represents the image quality actually acquired in an *in vivo* scenario. By resampling, the noise is effectively reduced, resulting in under-representation of the impact of resolution on the non-metric indices than in *in vivo* imaging using HR-pQCT acquired at the same resolution [15] (**Figure 3.5**d). However, resampling facilitated accurate comparison between exactly matched volumes of interest [16]. Similarly, *ex vivo* imaging disregards the artifacts typically associated with *in vivo* imaging conditions such as lower signal-to-noise ratio due to greater surrounding bone and soft tissue volumes, increased beam hardening, and artifacts related to patient motion. Nonetheless, *ex vivo* imaging was necessary in this study for obtaining the μCT reference values and for the resampling simulations.

In conclusion, we found that three non-metric indices of trabecular bone structure are affected by the spatial resolution of CT images. Most notably, the SMI deviated from the high-resolution μCT reference value depending on the structure type, whether plate-like or rod-like. The other two indices, the Conn.D and DA were both underestimated at an *in vivo* resolution (82 μm). It is not trivial to determine absolute threshold for validity of these non-metric indices without considering a specific study design (e.g. relative resolution, the size of the treatment effect to detect, and specimen type). The results of this study provide an upper bound for the accuracy of the non-metric indices under limited resolution scenarios.

REFERENCES

[1] Gouveia CH, Jorgetti V, Bianco AC. Effects of thyroid hormone administration and estrogen deficiency on bone mass of female rats. J Bone Miner Res 1997; 12: 2098-107.

[2] Zeni S, Gomez-Acotto C, Di Gregorio S, Mautalen C. Differences in bone turnover and skeletal response to thyroid hormone treatment between estrogen-depleted and repleted rats. Calcif Tissue Int 2000; 67: 173-7.

[3] Huiskes R, Ruimerman R, van Lenthe GH, Janssen JD. Effects of mechanical forces on maintenance and adaptation of form in trabecular bone. Nature 2000; 405: 704-6.

[4] Chesnut CH, 3rd, Majumdar S, Newitt DC, Shields A, Van Pelt J, Laschansky E, Azria M, Kriegman A, Olson M, Eriksen EF, Mindeholm L. Effects of salmon calcitonin on trabecular microarchitecture as determined by magnetic resonance imaging: results from the QUEST study. J Bone Miner Res 2005; 20: 1548-61.

[5] van Rietbergen B, Majumdar S, Newitt D, MacDonald B. High-resolution MRI and micro-FE for the evaluation of changes in bone mechanical properties during longitudinal clinical trials: application to calcaneal bone in postmenopausal women after one year of idoxifene treatment. Clin Biomech (Bristol, Avon) 2002; 17: 81-8.

[6] Bouxsein ML, Uchiyama T, Rosen CJ, Shultz KL, Donahue LR, Turner CH, Sen S, Churchill GA, Muller R, Beamer WG. Mapping quantitative trait loci for vertebral trabecular bone volume fraction and microarchitecture in mice. J Bone Miner Res 2004; 19: 587-99.

[7] Kohler T, Beyeler M, Webster D, Muller R. Compartmental bone morphometry in the mouse femur: reproducibility and resolution dependence of microtomographic measurements. Calcif Tissue Int 2005; 77: 281-90.

[8] Boutroy S, Bouxsein ML, Munoz F, Delmas PD. In vivo assessment of trabecular bone microarchitecture by high-resolution peripheral quantitative computed tomography. J Clin Endocrinol Metab 2005; 90: 6508-15.

[9] Khosla S, Riggs BL, Atkinson EJ, Oberg AL, McDaniel LJ, Holets M, Peterson JM, Melton LJ, 3rd. Effects of sex and age on bone microstructure at the ultradistal radius: a population-based noninvasive in vivo assessment. J Bone Miner Res 2006; 21: 124-31.

[10] Ito M, Nishida A, Koga A, Ikeda S, Shiraishi A, Uetani M, Hayashi K, Nakamura T. Contribution of trabecular and cortical components to the mechanical properties of bone and their regulating parameters. Bone 2002; 31: 351-8.

[11] MacNeil JA, Boyd SK. Load distribution and the predictive power of morphological indices in the distal radius and tibia by high resolution peripheral quantitative computed tomography. Bone 2007; 41: 129-37.

[12] Mittra E, Rubin C, Qin YX. Interrelationship of trabecular mechanical and microstructural properties in sheep trabecular bone. J Biomech 2005; 38: 1229-37.

[13] Hildebrand T, Ruegsegger P. Quantification of Bone Microarchitecture with the Structure Model Index. Comput Methods Biomech Biomed Engin 1997; 1: 15-23.

[14] Davison KS, Siminoski K, Adachi JD, Hanley DA, Goltzman D, Hodsman AB, Josse R, Kaiser S, Olszynski WP, Papaioannou A, Ste-Marie LG, Kendler DL, Tenenhouse A,

Brown JP. Bone strength: the whole is greater than the sum of its parts. Semin Arthritis Rheum 2006; 36: 22-31.

[15] Guo XE, Kim CH. Mechanical consequence of trabecular bone loss and its treatment: a three-dimensional model simulation. Bone 2002; 30: 404-11.

[16] Odgaard A, Gundersen HJ. Quantification of connectivity in cancellous bone, with special emphasis on 3-D reconstructions. Bone 1993; 14: 173-82.

[17] Goulet RW, Goldstein SA, Ciarelli MJ, Kuhn JL, Brown MB, Feldkamp LA. The relationship between the structural and orthogonal compressive properties of trabecular bone. J Biomech 1994; 27: 375-89.

[18] Harrigan TP, Mann RW. Characterization of microstructural anisotropy in orthotropic materials using a second rank tensor. Journal of Materials Science 1984; 19: 761-767.

[19] Odgaard A. Three-dimensional methods for quantification of cancellous bone architecture. Bone 1997; 20: 315-28.

[20] Ding M, Hvid I. Quantification of age-related changes in the structure model type and trabecular thickness of human tibial cancellous bone. Bone 2000; 26: 291-5.

[21] Mosekilde L, Ebbesen EN, Tornvig L, Thomsen JS. Trabecular bone structure and strength - remodelling and repair. J Musculoskelet Neuronal Interact 2000; 1: 25-30.

[22] Ito M, Ikeda K, Nishiguchi M, Shindo H, Uetani M, Hosoi T, Orimo H. Multi-detector row CT imaging of vertebral microstructure for evaluation of fracture risk. J Bone Miner Res 2005; 20: 1828-36.

[23] Kothari M, Keaveny TM, Lin JC, Newitt DC, Genant HK, Majumdar S. Impact of spatial resolution on the prediction of trabecular architecture parameters. Bone 1998; 22: 437-43.

[24] Laib A, Ruegsegger P. Calibration of trabecular bone structure measurements of in vivo three-dimensional peripheral quantitative computed tomography with 28-microm-resolution microcomputed tomography. Bone 1999; 24: 35-9.

[25] Muller R, Koller B, Hildebrand T, Laib A, Gianolini S, Ruegsegger P. Resolution dependency of microstructural properties of cancellous bone based on three-dimensional mu-tomography. Technol Health Care 1996; 4: 113-9.

[26] Tabor Z. Analysis of the influence of image resolution on the discriminating power of trabecular bone architectural parameters. Bone 2004; 34: 170-9.

[27] Laib A, Hauselmann HJ, Ruegsegger P. In vivo high resolution 3D-QCT of the human forearm. Technol Health Care 1998; 6: 329-37.

[28] Burghardt AJ, Kazakia GJ, Majumdar S. A local adaptive threshold strategy for high resolution peripheral quantitative computed tomography of trabecular bone. Ann Biomed Eng 2007; 35: 1678-86.

[29] Davis KA, Burghardt AJ, Link TM, Majumdar S. The effects of geometric and threshold definitions on cortical bone metrics assessed by in vivo high-resolution peripheral quantitative computed tomography. Calcif Tissue Int 2007; 81: 364-71.

[30] Macneil JA, Boyd SK. Accuracy of high-resolution peripheral quantitative computed tomography for measurement of bone quality. Med Eng Phys 2007.

[31] Kim DG, Christopherson GT, Dong XN, Fyhrie DP, Yeni YN. The effect of microcomputed tomography scanning and reconstruction voxel size on the accuracy of stereological measurements in human cancellous bone. Bone 2004; 35: 1375-82.

[32] Day JS, Ding M, Odgaard A, Sumner DR, Hvid I, Weinans H. Parallel plate model for trabecular bone exhibits volume fraction-dependent bias. Bone 2000; 27: 715-20.

[33] Ridler TW, Calvard S. Picture thresholding using an iterative selection method. IEEE Transaction on Systems, Man, and Cybernetics 1979; SMC-8: 630-632.

Chapter 4 – Quantitative Characterization of Motion Artifact in the HR-pQCT Images of Distal Radius and Tibia

I. INTRODUCTION

An increasing number of research and clinical studies using high-resolution peripheral quantitative computed tomography (HR-pQCT) have been reported for the noninvasive *in vivo* assessment of trabecular bone structure at peripheral sites. The accuracy for estimating density, cortical geometry, trabecular structure, and mechanical parameters (using micro finite element modeling) has been validated against the corresponding gold-standard measurements [1-6]. The *in vivo* reproducibility for the densitometric measures and trabecular structure indices are CV_{rms} = < 1% and < 4.5%, respectively [3].

Motion artifacts, however, are confounding factor for the accuracy and reproducibility of these measurements. Although it only takes < 3 minutes for image acquisition during standard patient protocols, motion artifacts are commonly seen in the images (**Figure 4.1**), especially at the radius [3]. Patient movements typical during HR-pQCT image acquisition include tremor, twitch/spasm, and displacement. These motions are unpredictable (unlike periodic breathing during cardiogram) and difficult to monitor.

The severely degraded image quality associated with the motion artifact. It introduces substantial error in the accuracy and reproducibility of measurements obtained from the images. Indices that describe trabecular structure are suspected to be more prone to such errors compared with densitometric indices [3], because trabeculae only span 1-3 pixels and are is subject to partial volume averaging and thresholding. The degree of error

in density, cortical geometry, and trabecular structure measurements from HR-pQCT by motion artifacts has not previously been quantified. This information is essential for predicting the error caused by the detected degree of motion. It also contributes to preventing the subject from being exposed to additional radiation upon repeating the acquisition. In an effort to provide a guideline for grading image quality, the manufacturer has provided a grading system according to the apparent severity of the motion artifact in the image (**Figure 4.1**). The criteria for grading, however, are highly subjective and are not based on a quantitative measurement. While this image quality grading system can distinguish the worst image quality (grade 4 or 5) from the best quality (grade 1 or 2), the discriminatory power was not linear or reliable [7].

A non-subjective, standardized procedure for repeating the acquisition based on empirical data and that allows immediate decision-making in a clinical setting is necessary. The objective of this study is three-fold: (1) to develop a non-subjective technique to quantify subject motion during an HR-pQCT acquisition, (2) to establish an optimal metric for estimating the error in density and structure measures due to motion degradation, and (3) to define parameter-specific relationships between the optimal metric and expected precision error.

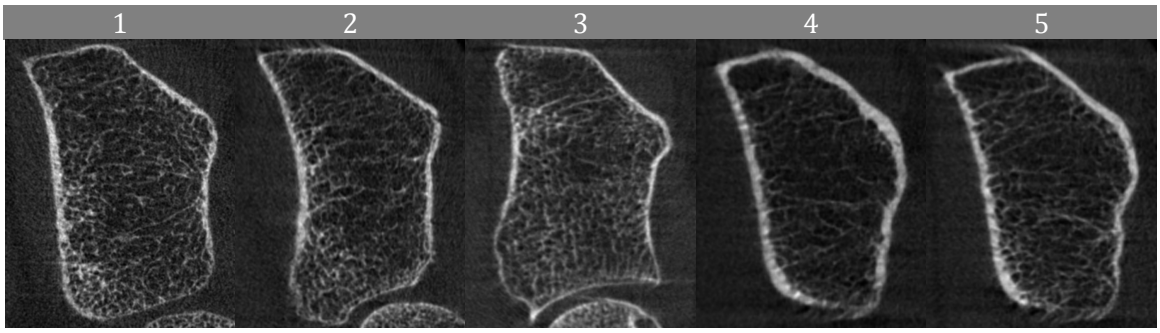

1	2	3	4	5
No visible motion artifacts.	Very slight artifacts - horizontal streaks at upper and lower ends of radius/tibia visible.	Horizontal streaks visible but cortex continuity is intact.	Large horizontal streaks visible; Cortex continuity is moderately disrupted at places and trabeculae are smeared.	Major horizontal streaks; Complete disruption of continuity of the cortex and trabecular structure.

Figure 4.1 Image quality grading guideline suggested by the manufacturer and representative reconstructed grayscale image of the distal radius for each grade.

II. METHODS

Motion artifact is a problem for image acquisition and procedure using any radiological devices on a live subject, from cardiogram [8, 9] to computer-assisted surgery [10]. In the effort to control for motion artifacts, restraining fixtures are used, the patient motion is monitored, and the detected motion is corrected for using a post-processing algorithm. For computed tomography, as three-dimensional image volume is reconstructed from a series of projection images (sinograms) collected over 180° and a certain integration time, the majority of motion leaves distinct traces in the sinogram data. The sinogram thereby includes the temporal and spatial information of the motion. Therefore, many attempts for detecting and correcting motion artifacts have been focused on the sinogram space. The object contour, fiducial markers [11], or anatomical landmarks are traced in the sinogram space, and the deviation from the idealized sinusoidal line is assumed to be due to subject motion.

In this study, as a non-subjective technique for quantifying the subject motion during an HR-pQCT image acquisition, the parallelized projection image at the 0° and 180° were compared using three commonly used similarity measures, namely sum of squared

intensity difference (SSD), normalized cross correlation (NCC), and the entropy (E) of the difference image. **Figure 4.3** summarizes the workflow for measuring the amount of motion during a single acquisition quantitatively.

Parallelization

Two parallel projection images at 0° and 180° must be constructed from the raw cone-beam projection using the manufacturer-provided algorithm prior to the calculations of the similarity measures. The in vivo HR-pQCT scanner (XtremeCT, Scanco Medical, Brüttisellen, Switzerland) used in this study was a cone-beam CT system with 18.6° fan angle and 3.0° cone angle. To construct the parallel projection at 0° and 180°, therefore, the beams extracted from the contiguous 78 projections spanning adjacent ±9.32° degrees each were used (**Figure 4.3**). The resulting parallel projection image at each angle, therefore, contained both spatial and temporal information collected over this range. The resulting images correspond to the palmer and dorsal projections for the radius, and the medial and lateral projections for the tibia (**Figure 4.3**). Next, the dark and flat field intensities were corrected in each image. The parallel projection image at 180° was then flipped with respect to the detector center to match and to be compared to the parallel projection image at 0° (**Figure 4.3**). If there was absolutely no motion, this flipped 180° parallel projection image should match the parallel projection image at 0°. Any difference between these two parallel projection images were, therefore, assumed to be the result of patient motion during the acquisition primarily. Finally, a fixed threshold was applied to the parallel projection image at 0°, to identify the region containing bone along the long axis of the detector. On average, this bone region spanned 528 pixels and 598 pixels out of 1536 pixels for the radius and tibia, respectively. The similarity measures were calculated in the same region of both images.

Similarity measures

Similarity measures are metrics that assess the degree to which two images are comparable, and they have been the essential part of motion detection and image registration. These include sum or mean of squared intensity difference, cross correlation, ratio image uniformity, and mutual information. The former three metrics are intensity-based methods, therefore, work better for images from the same modality as the image intensity is the same [12]. SSD and NCC have successfully been used to compare projection images in sinogram-based motion detection [13], therefore, selected to be used in this study. Let *f* be the fixed image (the projection image at 0°) and *g* be the moving image (the projection image at 180°). The SSD and NCC are given by:

$$SSD = \sum_i^N \left(\frac{f_i - g_i}{\bar{f}} \right)^2,$$

and

$$NCC = -\frac{\sum_i^N (f_i \cdot g_i)}{\sqrt{\sum_i^N f_i^2 \cdot \sum_i^N g_i^2}},$$

where N is the number of voxels and f_i and g_i are the intensity values of the *i*th voxel. The greater the value, the larger the difference between the 0° and 180° projection images. Consequently, the proportional degree of motion artifact in the resulting reconstructed images is expected. Although entropy (E) of the difference image is not commonly used for motion detection or image registration, it is a measure the disorder. E was calculated by:

$$E = -\sum p(h) \cdot \log(p(h))$$

where *p(h)* is the histogram counts of the difference image, *h*, of the projection image at 0° (*f*) and 180° (*g*). The greater the disorder in the difference image, the larger the difference between the 0° and 180° projection images (**Figure 4.2**).

All similarity measures were normalized by the mean value of the respective measure for all images with grade 1 at the respective site (no visible motion), in order to contrast between similarity measures. Only the similarity measures of the image with worse grade of a pair were included, as no a priori knowledge of the degree of motion artifact in the reconstructed image is available in a clinical setting. Similarity measure calculations were implemented using Matlab (Mathworks, Natick, MA).

Dataset

All datasets with repeated acquisitions of the same site acquired during a single exam collected for various studies conducted in our laboratory over the past 5 years were retrospectively evaluated. Two trained observers independently graded all the images according to the manufacturer-suggested image quality grading system (**Figure 4.1**). In case of disagreement, a consensus grade was decided mutually. For this study, all exams with pairs that include at least one grade 1 image (no visible motion) were included. A total of 54 pairs of HR-pQCT images of the distal radius (N=33) and tibia (N=21) acquired for 51 women (age = 59 ± 14 yr) and 3 men (46 ± 2 yr) resulted. The number of pairs in each grade combination is summarized in **Table 4.1**. All subjects gave written informed consent prior to participation to each study. The protocol was approved by the University of California, San Francisco Committee on Human Research.

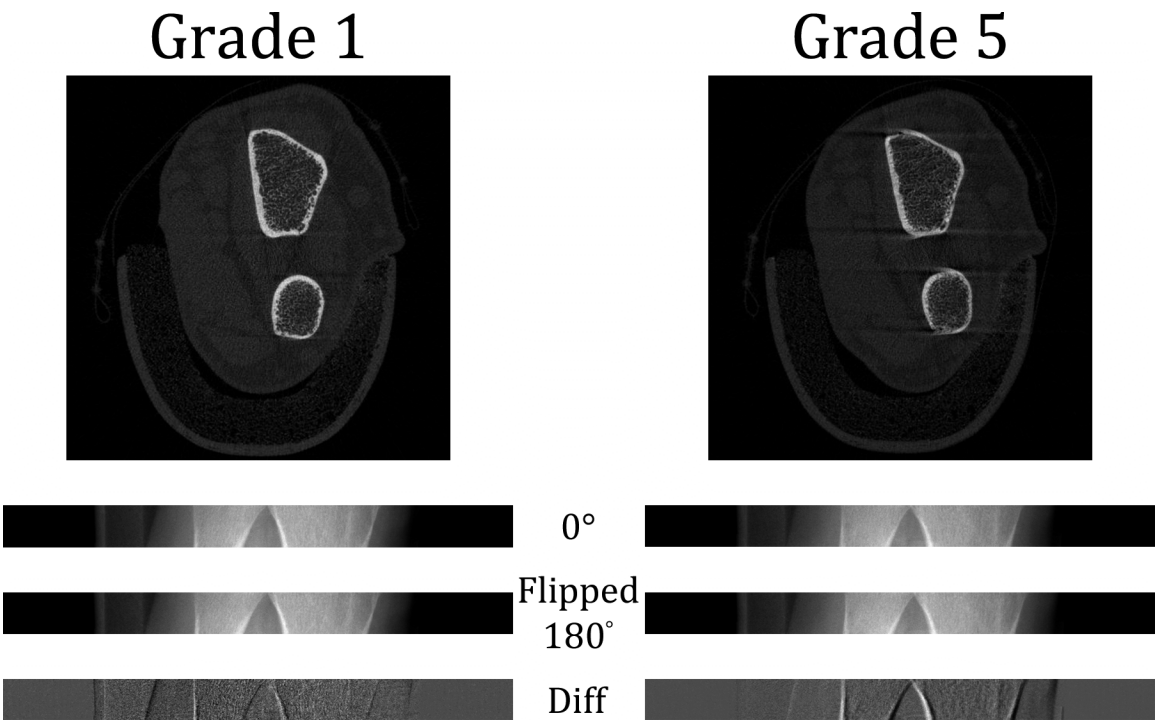

Figure 4.2 Comparison of the same radius image with grade 1 motion (left) and grade 5 motion (right). From the top: the reconstructed images, parallelized projection images at 0°, flipped parallelized projection images at 180°, and the difference between image of the two. For grade 5, the flipped parallelized projection image at 180° is shifted to the right with respect to the parallelized projection image at 0°. This offset is also apparent in the difference image with more defined edges of the projected bone contour.

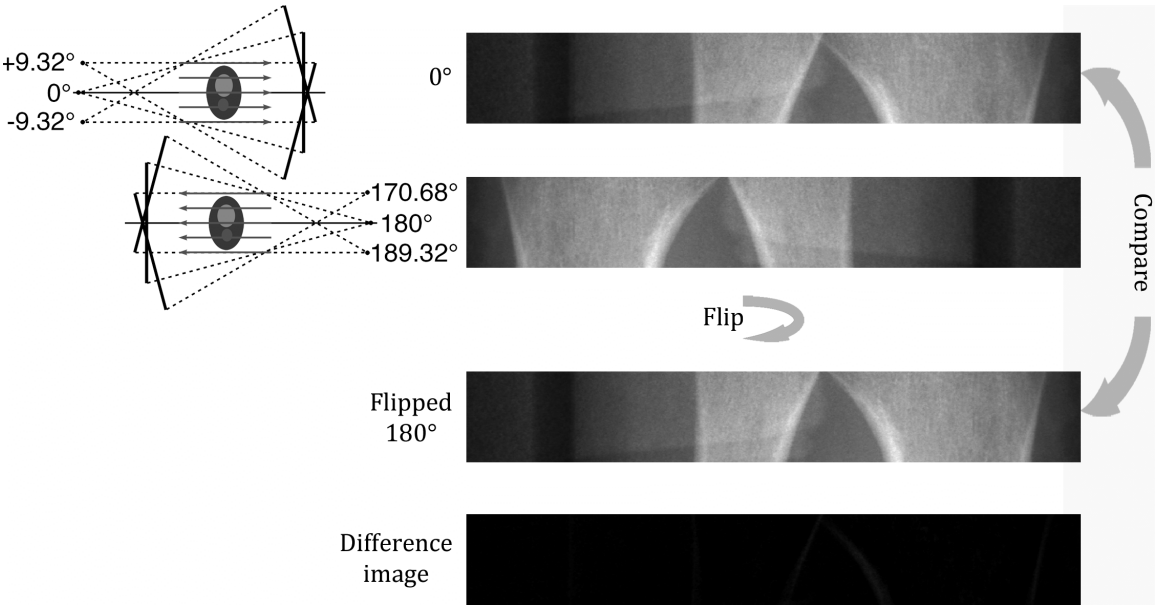

Figure 4.3 Schematic drawing explaining the analysis process. Two parallelized projection images at 0° and at 180° were constructed from the contiguous 78 raw projections each. The 180° image was flipped and compared to the 0° image using the SSD and NCC. For the ideal case where there is no motion, the difference image between the two parallelized projection images should be zero. The disorder in the difference image was measured using E.

Table 4.1 Number of samples in each grade pair

Pairs	N		
	Total	Radius	Tibia
1-1	7	3	4
1-2	18	12	6
1-3	18	11	7
1-4	7	5	2
1-5	4	2	2
TOTAL	54	33	21

HR-pQCT image acquisition

Subjects were imaged at least twice in a clinical HR-pQCT system (XtremeCT, Scanco Medical AG, Brüttisellen, Switzerland) using the manufacturer's standard in vivo protocol [3, 14-18]. Each subject's forearm and lower leg were positioned in the thumb-up and toe-up positions, respectively. They were then immobilized in corresponding carbon-fiber molds, and fixed to the scanner to minimize motion during acquisition. A 9.02-mm-long section (110 slices) of the radius and tibia was imaged starting at 9.5 mm and 22.5 mm proximal to the distal endplate, respectively, extending proximally. The non-dominant side was scanned unless there was a history of fracture, in which case, the contra-lateral side was scanned.

The x-ray source potential was 60 kVp with a current of 900 μA. A two-dimensional detector containing 3072 × 256 CCD elements was used to acquire 750 projections over 180 degrees with at a 100 ms integration time per angular position. The 12.6 cm field of view was reconstructed across a 1536 × 1536 matrix, yielding 82 μm isotropic voxels. Image acquisition time was 3 minutes per scan. Images were immediately reviewed for motion artifacts in a single low-resolution reconstructed image for checking motion artifacts. Acquisition was repeated if obvious artifacts were detected. The effective dose was 3 μSv per measurement.

Attenuation values were converted to equivalent hydroxyapatite density (mg HA/cm^3) using a linear relationship based on a phantom containing cylinders of HA-resin mixtures with five different concentrations (0, 100, 200, 400, and 800 mg HA/cm^3) (QRM, Moehrendorf, Germany). For quality control, the linear attenuation values of the phantom were monitored daily.

HR-pQCT image analysis

The images were segmented and processed in accordance with the standard patient-style analysis protocol using Image Processing Language (Scanco Medical AG, Brüttisellen, Switzerland) as described elsewhere [3, 14-18]. First, a semi-automated edge-defining algorithm was applied to the original grayscale image to contour the periosteal surface. The total volumetric bone mineral density (vBMD) was calculated within this contour. The cortical and trabecular regions were segmented automatically by the analysis protocol as described in detail by Laib et al [19]. Cortical and trabecular volumetric BMDs (Ct.vBMD and Tb.vBMD, respectively) were calculated as the mean density within the segmented corresponding volume of interest. Cortical thickness (Ct.Th) and cortical area (Ct.Ar) were calculated using an annular model approximation [20].

Calculation of the trabecular densitometric and structural indices from HR-pQCT images has been described [19], validated [2, 21, 22] and employed in a number of recent studies [3, 14-16, 18, 23, 24]. Trabecular bone volume fraction (BV/TV) is derived from Tb.vBMD assuming fully mineralized bone to have 1200 mg/cc HA. In addition, trabecular number (Tb.N), -thickness (Tb.Th), and -separation (Tb.Sp) were calculated. The reproducibility of the trabecular structure indices obtained from in vivo HR-pQCT images is ≤ 5.8% at the radius and ≤1.5% at the tibia [16]. The percent difference in the cortical and trabecular densitometric, geometric, and structure indices were calculated between the images with and without motion artifact as the error introduced by the motion artifact.

Statistical Analysis

The Shapiro–Wilk W test was used to test the normality of the data. As most similarity measures and the bone indices were not normally distributed, non-parametric methods were employed. First, to put it in a perspective, the variability of the similarity measures were compared against the quality grade system proposed by the manufacturer. To further contrast between each grade, Wilcoxon/Kruskal-Wallis (WKW) tests and post hoc (Siegel) Turkey HSD tests were applied. To identify an optimal metric for estimating the error in density and structure measures due to motion degradation, Spearman's ρ was calculated for their association. A positive correlation indicates that the larger the value of a similarity measure, the proportionally larger the expected error in a calculated index, and vice versa. Furthermore, to establish the relationship between the degree of absolute percent error in an index of interest and the similarity measures, multiple linear regression analyses were performed. From the slopes and intercepts, the expected error can be extrapolated. The significance was set at $\alpha = 0.05$ unless otherwise stated. All statistical tests were performed using JMP (version 7.0, SAS Institute Inc., Cary, NC).

III. RESULTS

Figure 4.4 displays the variability of the similarity measures of the parallel projection images with respect to the image quality grade of the reconstructed HR-pQCT images at the distal radius and tibia. WKW tests indicated that the mean values of sum of squared intensity difference (SSD) and normalized cross correlation (NCC) increased with the image quality grade for both radius and tibia ($p < 0.001$), but not entropy (E). Tukey-Kramer HSD test further revealed that the mean values of the similarity measures for the images graded higher than 3 were significantly higher compared to that of the images graded 1 regardless for both SSD and NCC and at both sites ($p < 0.01$ for radius and $p <$

0.001 for tibia) (**Figure 4.4**). While the mean values of the SSD and NCC for the images with adjacent grades (e.g. 1 and 2, 2 and 3, and 3 and 4), were not significantly different; however, the mean values for the images graded 5 were significantly higher than those for the images graded 3 and 4.

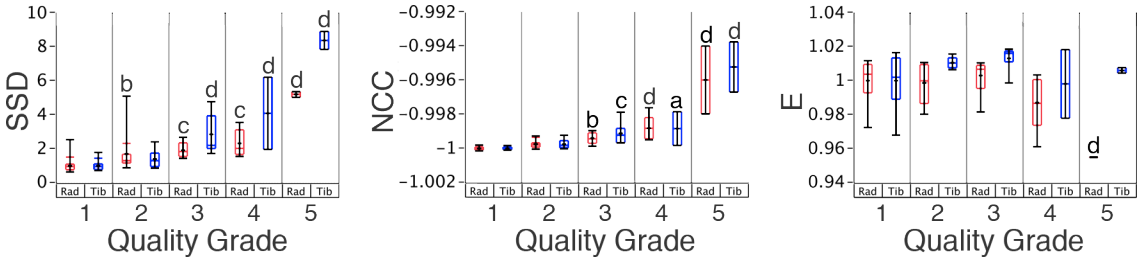

Figure 4.4 Variability of the similarity measures with respect to the image quality grade of HR-pQCT images at the distal radius (red) and tibia (blue). [a] $p < 0.05$; [b] $p < 0.01$; [c] $p < 0.001$; [d] $p < 0.0001$ with respect to the quality grade 1 (with no visible motion) determined by the (Siegel) Tukey test.

In general, with increasing motion artifacts as measured by SSD and NCC, the Ct.vBMD and Ct.Th were increasingly underestimated, and BV/TV and Tb.N were increasingly overestimated (**Figure 4.5**). In addition, both SSD and NCC were negatively correlated to the errors in Ct.Ar, Tot.vBMD, Tb.Th, and Tb.Sp (increasingly underestimated with increasing motion artifacts), and positively correlated to Tb.vBMD (increasingly overestimated) (**Table 4.2**). No significant correlation was found between any similarity measure and Ct.Ar, Tot.vBMD at the radius and Tb.vBMD and BV/TV at the tibia. The degree of correlations was similar between the two measures. E did not correlate with the error in any indices, except negatively correlated to Tot.vBMD, Tb.vBMD, and BV/TV at the radius only. The correlations were comparable between the radius and tibia in their density parameters, but stronger at the distal tibia in the cortical geometry and trabecular structure parameters (e.g. in the trabecular structure parameters, $|\rho| = 0.76\text{-}0.83$ and $p < 0.001$ vs. 0.38-0.55 and $p < 0.05$ at the radius).

Table 4.3 and **Table 4.4** summarize the results of the linear regression analyses between the similarity measures and the absolute percent errors introduced to Ct.vBMD,

Ct.Th, BV/TV, and Tb.N at distal radius and tibia, respectively. The slopes and intercepts for NCC were four orders of magnitude larger than SSD. This showcases the difference in their dynamics ranges – while a change in SSD indicates a proportional degree of error in a calculated index, a small increase in SSD indicates a large error. For example, if the value of NCC increased 1.5x the mean value for the images graded 1 (no visible motion), the error in Ct.vBMD would increase from 0.5% to 0.8%, whereas the same degree of increase in error can be achieved by NCC changing by 1/200 (**Table 4.3**). Among the three parameters, the largest slope was for Tb.N at both sites regardless of the similarity measure. This indicates that the errors in the Tb.N are more sensitive to the changes in the values of the similarity measures, thus to the motion artifacts.

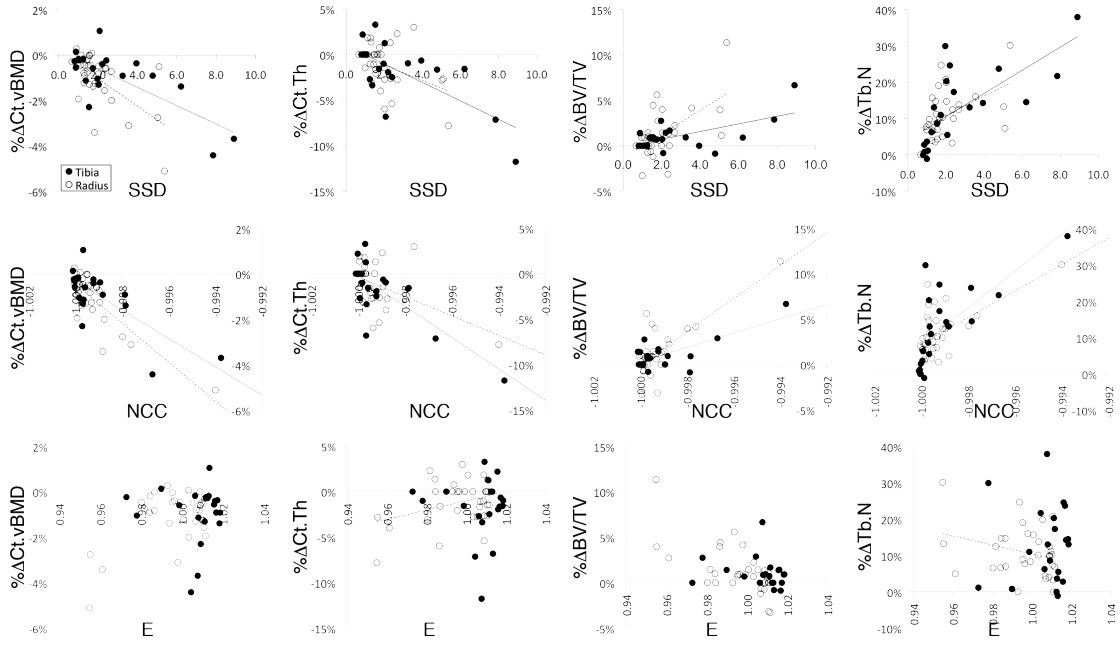

Figure 4.5 Scatter plots to show the correlations between the selected density, cortical geometry and trabecular structure parameters (Ct.vBMD, Ct.Th, BV/TV, and Tb.N) and the similarity measures (SSD, NCC, and E).

Table 4.2 Correlations (Spearman's ρ) between the similarity measures of the projection images with motion artifacts and the percent errors in the densitometric, cortical geometric and trabecular structure indices at the distal radius and tibia due to motion artifacts.

	%Δ Tot.vBMD		%Δ Ct.vBMD		%Δ Tb.vBMD		%Δ Ct.Th		%Δ Ct.Ar		%Δ BV/TV		%Δ Tb.N		%Δ Tb.Th		%Δ Tb.Sp	
	Rad	Tib	Rad	Tib	Rad	Tib	Rad	Tib	Rad	Tib	Rad	Tib	Rad	Tib	Rad	Tib	Rad	Tib
SSD	NS	-0.48[a]	-0.51[b]	-0.56[b]	0.53[b]	NS	-0.37[a]	-0.62[b]	NS	-0.59[b]	0.51[b]	NS	0.53[b]	0.83[d]	-0.38[a]	-0.81[d]	-0.55[c]	-0.81[d]
NCC	NS	-0.61[b]	-0.58[c]	-0.62[a]	0.51[b]	NS	-0.39[a]	-0.64[b]	NS	-0.62[b]	0.50[b]	NS	0.51[b]	0.78[d]	-0.38[a]	-0.77[d]	-0.54[b]	-0.76[c]
E	-0.52[b]	NS	NS	NS	-0.52[b]	NS	NS	NS	NS	NS	-0.58[c]	NS	NS	NS	NS	NS	NS	NS

N.B. [a] $p < 0.05$; [b] $p < 0.01$; [c] $p < 0.001$; [d] $p < 0.0001$; NS, not significant.

Table 4.3 Regression analyses between the similarity measures of the projection images with motion artifacts and the percent errors in Ct.vBMD, Ct.Th, BV/TV, and Tb.N at the distal radius due to motion artifacts.

	%Δ Ct.vBMD		%Δ Ct.Th		%Δ BV/TV		%Δ Tb.N	
	Slope	Intercept	Slope	Intercept	Slope	Intercept	Slope	Intercept
SSD	0.58[c]	-0.10	0.96[c]	-0.02	1.14[c]	-0.44	2.64[b]	5.57
NCC	847[d]	847	1189[d]	1190	1650[d]	1651	3649[c]	3657
E	-38.4[b]	39.3	-54.4[b]	56.1	-79.4[c]	80.9	NS	NS

N.B. [a] $p < 0.05$; [b] $p < 0.01$; [c] $p < 0.001$; [d] $p < 0.0001$; otherwise, not significant.

Table 4.4 Regression analyses between the similarity measures of the projection images with motion artifacts and the percent errors in Ct.vBMD, Ct.Th, BV/TV, and Tb.N at the distal tibia due to motion artifacts.

	%Δ Ct.vBMD		%Δ Ct.Th		%Δ BV/TV		%Δ Tb.N	
	Slope	Intercept	Slope	Intercept	Slope	Intercept	Slope	Intercept
SSD	0.39[d]	-0.03	0.85[c]	0.09	0.44[c]	-0.02	3.15[c]	4.36
NCC	591[d]	592	1505[d]	1506	815[d]	815	5006[c]	5014
E	NS	NS	NS	NS	NS	NS	NS	NS

N.B. [a] $p < 0.05$; [b] $p < 0.01$; [c] $p < 0.001$; [d] $p < 0.0001$; otherwise, not significant.

IV. DISCUSSION

In this study, we proposed a non-subjective, standardized procedure for repeating the HR-pQCT acquisition, where the parallelized projection images at the 0° and 180° were compared using three similarity measures – namely, SSD, NCC, and E. SSD and NCC were significantly correlated to the percent errors in the densitometric, cortical geometric, and trabecular structural indices at the distal radius and tibia calculated from the reconstructed HR-pQCT images. Both were particularly sensitive to the errors in the trabecular structure indices, and at the distal tibia. E only correlated to Tot.vBMD, Tb.BMD, and BV/TV in the

radius. While the SSD was proportionally correlated to the errors in the calculated indices, the dynamic range for NCC was four orders of magnitude larger than that of SSD. Therefore, SSD is the most suitable similarity measure for comparing the parallelized projection images at 0° and 180° as a quantitative metric for motion artifacts in the reconstructed HR-pQCT image.

It has been demonstrated that SSD can differentiate the sinograms with and without motion with low probability for false detection [13]. It is also robust against the object form in the (projection) image, the geometry of the CT system, and beam hardening effect [13]. For instance, a 4.5% change in Ct.Th at the distal tibia for postmenopausal women after being on alendronate treatment for 24 months was reported [25]. Deducting from our linear regression results, such degree of error is expected from the images with 5 times the mean SSD value of the images with no visible motion artifacts. It also compares to the degree of error in Ct.Th calculated from the reconstructed image with a grade-5-level motion.

The size of the object being scanned may impact signal to noise ratios, and hence affect the performance of the proposed method. Multiple regression analyses with analyzed bone area included improved the correlation between SSD and the errors in the Ct.vBMD and Ct.Th significantly (both $p < 0.05$), but not for the errors in the trabecular structure indices. Therefore, controlling for the analyzed area is suggested when predicting the error in Ct.vBMD and Ct.Th using SSD as the similarity measure.

There are several limitations worth noting. The fact that HR-pQCT image acquisition does not cover full 360° means that only the 0° image and the flipped 180° images can be compared. Although the raw cone-beam projection images were parallelized the temporal and spatial information contained in the 78 projections each were utilized to construct the 0° image and 180° image, it accounts for 20% of the entire sinogram (**Figure 4.3**). The

information contained in the remaining 80% is not fully utilized. For example, if the arm or leg twitched and came back to the exact same spatial location within this interval, it will be undetected when comparing the 0° and 180° images; yet the motion artifact may be visible in the reconstructed image.

It is suspected that the proposed method is most sensitive to a permanent in-plane horizontal translational movement (wall-to-wall movement). Its sensitivity for other types of subject movement, however, may be limited. An out-of-plane movement (pull-in or -out of the scanner), in-plane vertical translational movement (towards or away from the floor/ceiling) of sub-millimeter level, and rotational displacement of few degrees occurred during the acquisition may not cause as dramatic difference in the 180° image from the 0° image. Rotational motion, however, may cause larger error in the trabecular structure indices compared to the translational motion as reported by Gomberg et al [26]. The correlation between the degree of error in the index of interest and the degree of motion must also be elucidated. A future study, therefore, should evaluate the sensitivity of the proposed method in detecting both rotational and translational movements in a controlled manner.

The strengths of the proposed approach for detecting the subject movement during HR-pQCT image acquisition are that it is (1) quantitative (non-subjective) and (2) practical and implementable for a clinical use. From the empirical relationship between the similarity measures and the errors in the calculated indices this study has provided, the expected error in the index of interest can be calculated. Such information is also important for more realistic statistical power calculation. It also provides a basis for establishing a threshold in which to accept or reject an image or to include or exclude a measurement that fits the specific study design. Since it is non-subjective, a decision for repeating the acquisition can be standardized across operator, scanner, and sites for a large-scale study. The clear

definition of the acceptance/rejection criteria saves the subject from unnecessary radiation exposure. It also allows comprehensive comparison across different study results. The use of raw sinograms allows an immediate response in case a motion artifact is suspected without waiting for the reconstruction process to complete.

In conclusion, the technique for detecting the subject movement during HR-pQCT image acquisition that is proposed has the potential for improving both research and clinical studies using this modality.

REFERENCES

[1] Liu XS, Zhang XH, Sekhon KK, Adam MF, McMahon DJ, Bilezikian JP, Shane E, Guo XE. High-Resolution Peripheral Quantitative Computed Tomography Can Assess Microstructural and Mechanical Properties of Human Distal Tibial Bone. J Bone Miner Res 2009.

[2] MacNeil JA, Boyd SK. Accuracy of high-resolution peripheral quantitative computed tomography for measurement of bone quality. Med Eng Phys 2007; 29: 1096-105.

[3] MacNeil JA, Boyd SK. Improved reproducibility of high-resolution peripheral quantitative computed tomography for measurement of bone quality. Med Eng Phys 2008; 30: 792-9.

[4] Sekhon K, Kazakia GJ, Burghardt AJ, Hermannsson B, Majumdar S. Accuracy of volumetric bone mineral density measurement in high-resolution peripheral quantitative computed tomography. Bone 2009; 45: 473-9.

[5] Sode M, Burghardt AJ, Nissenson RA, Majumdar S. Resolution dependence of the non-metric trabecular structure indices. Bone 2008; 42: 728-36.

[6] Varga P, Zysset PK. Assessment of volume fraction and fabric in the distal radius using HR-pQCT. Bone 2009; 45: 909-17.

[7] Pialat JB, Burghardt AJ, Sode M, Link TM, Majumdar S. Motion Artifacts in High-Resolution Peripheral Quantitative Computed-Tomography of Wrist and Ankle: Usefulness of Visual Grading to assess Image Quality. In: ASBMR 2010 Annual Meeting. Tronto, ON, Canada; 2010.

[8] Horiguchi J, Fukuda H, Yamamoto H, Hirai N, Alam F, Kakizawa H, Hieda M, Tachikake T, Marukawa K, Ito K. The impact of motion artifacts on the reproducibility of repeated coronary artery calcium measurements. Eur Radiol 2007; 17: 81-6.

[9] Lu W, Parikh PJ, Hubenschmidt JP, Politte DG, Whiting BR, Bradley JD, Mutic S, Low DA. Reduction of motion blurring artifacts using respiratory gated CT in sinogram space: a quantitative evaluation. Med Phys 2005; 32: 3295-304.

[10] Marmulla R, Muhling J. The influence of computed tomography motion artifacts on computer-assisted surgery. J Oral Maxillofac Surg 2006; 64: 466-70.

[11] Pauchard Y, Boyd SK. Landmark based compensation of patient motion artifacts in computed tomography. In: Jiang H, Ehsan S, editors.: SPIE; 2008. p. 69133C.

[12] Hajnal JV, Saeed N, Soar EJ, Oatridge A, Young IR, Bydder GM. A Registration and Interpolation Procedure for Subvoxel Matching of Serially Acquired MR Images. Journal of Computer Assisted Tomography 1995; 19: 289-296.

[13] Ens S, Muller J, Kratz B, Buzug TM, European c, th. Sinogram-Based Motion Detection in Transmission Computed Tomography. 2008.

[14] Boutroy S, Bouxsein ML, Munoz F, Delmas PD. In vivo assessment of trabecular bone microarchitecture by high-resolution peripheral quantitative computed tomography. J Clin Endocrinol Metab 2005; 90: 6508-15.

[15] Dalzell N, Kaptoge S, Morris N, Berthier A, Koller B, Braak L, van Rietbergen B, Reeve J. Bone micro-architecture and determinants of strength in the radius and tibia: age-

related changes in a population-based study of normal adults measured with high-resolution pQCT. Osteoporos Int 2009; 20: 1683-94.

[16] Kazakia GJ, Hyun B, Burghardt AJ, Krug R, Newitt DC, de Papp AE, Link TM, Majumdar S. In vivo determination of bone structure in postmenopausal women: a comparison of HR-pQCT and high-field MR imaging. J Bone Miner Res 2008; 23: 463-74.

[17] Melton LJ, 3rd, Riggs BL, van Lenthe GH, Achenbach SJ, Muller R, Bouxsein ML, Amin S, Atkinson EJ, Khosla S. Contribution of in vivo structural measurements and load/strength ratios to the determination of forearm fracture risk in postmenopausal women. J Bone Miner Res 2007; 22: 1442-8.

[18] Vico L, Zouch M, Amirouche A, Frère D, Laroche N, Koller B, Laib A, Thomas T, Alexandre C. High-Resolution pQCT Analysis at the Distal Radius and Tibia Discriminates Patients With Recent Wrist and Femoral Neck Fractures. Journal of Bone and Mineral Research 2008; 23: 1741-1750.

[19] Laib A, Hauselmann HJ, Ruegsegger P. In vivo high resolution 3D-QCT of the human forearm. Technol Health Care 1998; 6: 329-37.

[20] Davis KA, Burghardt AJ, Link TM, Majumdar S. The effects of geometric and threshold definitions on cortical bone metrics assessed by in vivo high-resolution peripheral quantitative computed tomography. Calcif Tissue Int 2007; 81: 364-71.

[21] Laib A, Ruegsegger P. Calibration of trabecular bone structure measurements of in vivo three-dimensional peripheral quantitative computed tomography with 28-microm-resolution microcomputed tomography. Bone 1999; 24: 35-9.

[22] Muller R, Hildebrand T, Hauselmann HJ, Ruegsegger P. In vivo reproducibility of three-dimensional structural properties of noninvasive bone biopsies using 3D-pQCT. J Bone Miner Res 1996; 11: 1745-50.

[23] Khosla S, Riggs BL, Atkinson EJ, Oberg AL, McDaniel LJ, Holets M, Peterson JM, Melton LJ, 3rd. Effects of sex and age on bone microstructure at the ultradistal radius: a population-based noninvasive in vivo assessment. J Bone Miner Res 2006; 21: 124-31.

[24] Sornay-Rendu E, Boutroy S, Munoz F, Delmas PD. Alterations of cortical and trabecular architecture are associated with fractures in postmenopausal women, partially independent of decreased BMD measured by DXA: the OFELY study. J Bone Miner Res 2007; 22: 425-33.

[25] Burghardt AJ, Kazakia GJ, Sode M, de Papp AE, Link TM, Majumdar S. A longitudinal HR-pQCT study of alendronate treatment in post-menopausal women with low bone density: Relations between density, cortical and trabecular micro-architecture, biomechanics, and bone turnover. J Bone Miner Res 2010.

[26] Gomberg BR, Wehrli FW, Vasilic B, Weening RH, Saha PK, Song HK, Wright AC. Reproducibility and error sources of micro-MRI-based trabecular bone structural parameters of the distal radius and tibia. Bone 2004; 35: 266-76.

Chapter 5 – Regional Variations of Gender-Specific and Age-Related Differences in Trabecular Bone Structure of the Distal Radius and Tibia

I. INTRODUCTION

Density and structural indices of trabecular bone derived from HR-pQCT images are usually reported as average values for the entire trabecular compartment of interest. In practice, their measurements can vary substantially throughout cross-sections of the distal radius and tibia (**Figure 5.1**). In fact, Lai et al imaged cores of trabecular bone using μCT and found that the trabecular bone in the posterior region of the distal tibia exhibits significantly higher BMD, BV/TV, Tb.N, Tb.Th, and degree of anisotropy, as well as lower Tb.Sp and structure model index compared to the anterior region (all $p < 0.01$) [1]. This is most likely the result of adaptation to the habitual loading pattern [1], because the posterior part of the distal tibia is subject to substantial compressive and shear forces from the ground reaction and internal muscle forces during gait [2, 3]. These regional differences are obscured by global averaging of the entire trabecular compartment. The standard deviation of trabecular separation (denoted either as Tb.1/N.SD or Tb.Sp.SD) is often regarded as a measure of heterogeneity in trabecular bone distribution. While this indicates the degree to which the structure is heterogeneous across the entire trabecular region, it does not provide spatial information.

Regional analysis, by subdividing the HR-pQCT images of the radius and tibia cross-section, provides complementary information about how the intrinsic structural heterogeneity of trabecular structure is related to the underlying biomechanical conditions.

We hypothesize that trabecular bone structure varies spatially in the distal radius and tibia, and that the degree of gender- and age-related differences vary depending on the region. The objective of this study is to use *in vivo* HR-pQCT to investigate regional variations in trabecular structure at the distal radius and tibia and its differences due to gender and age.

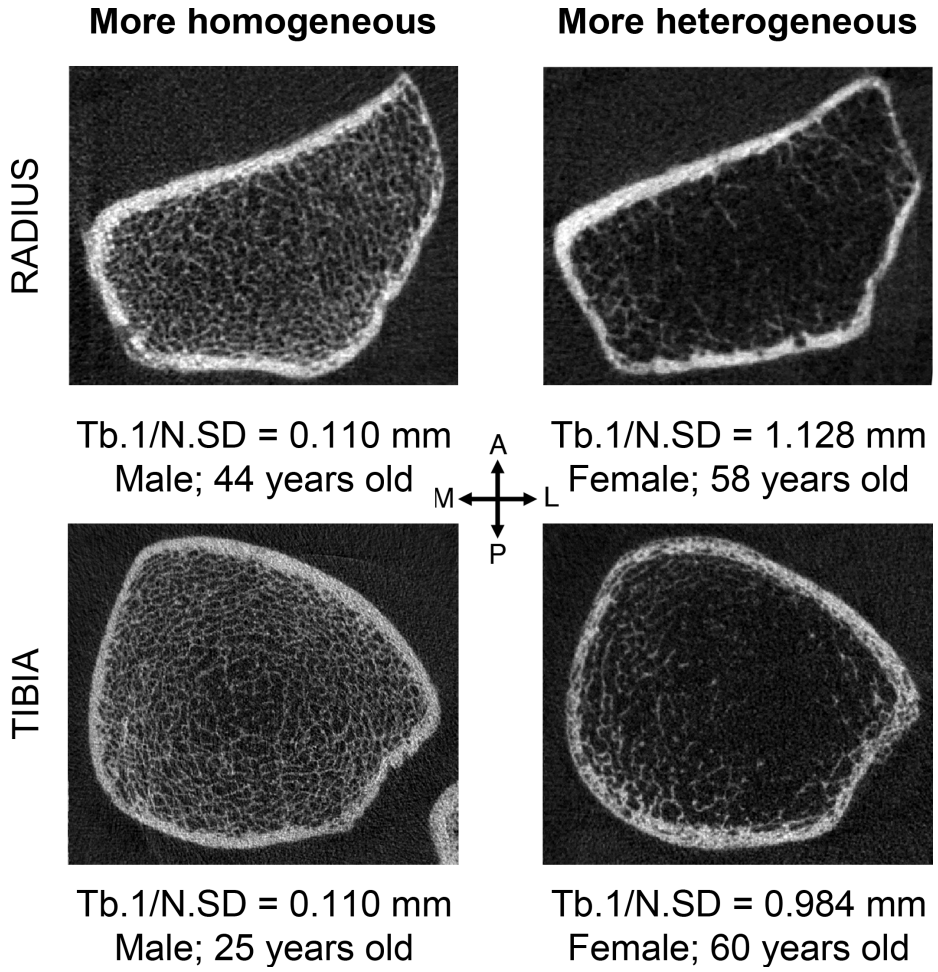

Figure 5.1 Representative HR-pQCT images of cross-sections of human distal left radius (top) and tibiae (bottom) with low Tb.1/N.SD (more homogenously distributed) (left) and high Tb.1/N.SD (more heterogeneous distributed) (right). Notice that not only the distribution but also the thickness of trabeculae varies from subregion to subregion.

II. MATERIALS AND METHODS

Subjects

Healthy volunteers aged between 20 to 78 years – 93 women (mean age 48.1 ± 15.8 yr) and 53 men (mean age 44.7 ± 16.7 yr) – were recruited through public fliers posted locally as a part of ongoing effort to build a normative database. Subjects with no known disease conditions or who had received no chronic treatment that may affect bone metabolism were enrolled. All subjects gave written informed consent prior to participation. Out of 93 women, 43 were postmenopausal, who had complete cessation of menses for at least six months prior to entrance into the study. Among a total of 79 individuals with DXA measurements (54 women and 25 men), 15 women and 10 men were classified as osteopenic (-1 < T-score < -2.5 at either L1-L4 or total femur), and 7 women and 3 men were classified as osteoporotic (T-score ≤ -2.5). 46% of the subjects were Asian, followed by 46% Caucasian, reflecting the ethnic composition of San Francisco Bay Area. The study protocol was approved by the University of California San Francisco Committee on Human Research.

HR-pQCT Image Acquisition

The distal radius and tibia of each subject were imaged using an *in vivo* HR-pQCT scanner (XtremeCT, Scanco Medical, Brüttisellen, Switzerland). HR-pQCT image acquisitions were performed by a total of 5 operators over the 3-year course of the study. Each subject's forearm and lower leg were immobilized in corresponding carbon-fiber molds, and fixed to the scanner to minimize motion during acquisition. A 9-mm-long section of the radius and tibia was imaged 9.5 mm and 22.5 mm proximal to the distal endplate, respectively. The non-dominant side was scanned unless there was a history of fracture, in which case, the contra-lateral side was scanned. The x-ray source potential was 60 kVp with a current of

900 μA. A two-dimensional detector containing 3072 × 256 CCD elements was used to acquire 750 projections at a 100 ms integration time per projection. The 12.6 mm field of view was reconstructed across a 1536 × 1536 matrix, yielding 82 μm isotropic voxels. Image acquisition time was 3 minutes per scan. Images were immediately reviewed for motion artifacts and repeated if obvious artifacts were detected. Five radius images were excluded due to motion artifacts despite repeated acquisition. The final dataset consisted of 142 radius and 146 tibiae images. The effective dose was < 3 μSV per measurement [4].

Attenuation values were converted to equivalent hydroxyapatite density (mg HA/cm^3) using a linear relationship based on a phantom containing cylinders of HA-resin mixtures with five different concentrations (0, 100, 200, 400, and 800 mg HA/cm^3) (QRM, Moehrendorf, Germany). For quality control, the linear attenuation values of the phantom were monitored daily.

Analysis

The images were segmented and processed in accordance to the standard patient-style analysis protocol using the Image Processing Language (Scanco Medical AG, Brüttisellen, Switzerland) as described elsewhere [5-12]. First, a semi-automated edge-defining algorithm was applied to the original grayscale image to contour the periosteal surface. The cortical and trabecular regions were segmented automatically by the analysis protocol as described in detail by Laib et al [9]. The following process for defining subregions was performed on the trabecular mask automatically using Matlab at every slice. The trabecular compartment was first divided into two concentric circular regions (inner and outer subregions), where the area of the inner subregion was 60% of the entire trabecular region. This was consistent with the definition of inner and outer subregions where density measurements were obtained as a part of the standard patient analysis [12,

13]. Furthermore, the inner and outer trabecular compartments were divided into angular quadrants at each slice based on the defined reference line. For the radius, the major axis of the radius cross-section (the longest diameter through the centroid) was used as a reference, as the angle between the major axis of the radius and a line connecting the centroids of the radius and ulna cross-sections moved substantially within a scanned span (~ 3° for radius as opposed to 0.5° for tibia). The quadrants were placed 45° to the reference line. For the tibia, a line connecting the centroids of the tibia and fibula cross-sections was used as a reference. The quadrants were placed 0° to the reference line. A total of 8 subregions resulted, as shown in **Figure 5.2**. Each subregion is denoted in a combination of two letters based on anatomic location – I and O denote inner and outer subregions, respectively; and M, P, L, and A denote medial, posterior, lateral and anterior, respectively.

Calculation of the trabecular densitometric and structural indices from HR-pQCT images has been described [9], validated [14-16] and employed in many studies [5-8, 10-12]. In addition to the trabecular bone volume fraction (BV/TV), number (Tb.N), thickness (Tb.Th), separation (Tb.Sp), standard for the patient analysis, the standard deviation of trabecular separation (Tb.1/N.SD, μm) was taken as a measure of heterogeneity in trabecular distribution [17]. These trabecular structural indices were calculated for the entire trabecular compartment (the global means), as well as for the inner, outer, and all 8 subregions. The reproducibility of the trabecular structure indices obtained from *in vivo* HR-pQCT images is ≤ 5.8% at the radius and ≤1.5% at the tibia [7].

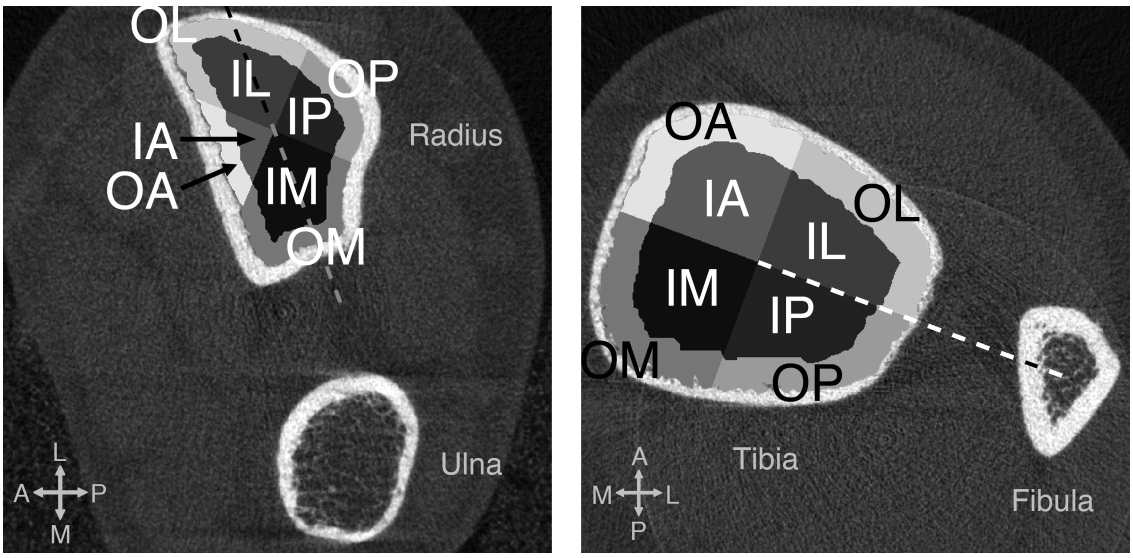

Figure 5.2 The region definitions at the distal radius (left) and tibia (right) used in this study. A total of 8 subregions were defined at each slice as follows. The trabecular compartment was divided into two concentric circular regions (inner and outer subregions) where the area of inner subregion was 60% of the entire trabecular region. The trabecular compartment was further divided into angular quadrants based on the defined reference line (dashed). The major axis of the cross-section was used as a reference for radius, and the quadrants were placed 45° to it. The line connecting the centroids of the tibia and fibula cross-sections was used as a reference for tibia, and quadrants were placed 0° to it.

Statistical analysis

Our dataset contained 125 left and 17 right radii and 125 left and 21 right tibiae but no significant difference in any of the structural indices was detected between the right and left limbs, therefore, they were pooled. The Shapiro-Wilk W test was used to test the normality of the data. As some indices (especially Tb.Sp and Tb.1/N.SD) were not normally distributed, non-parametric methods were employed for all statistical analyses.

To test the significance of differences in the calculated structural indices in each subregion compared to the global means calculated for the entire trabecular compartment, as well as between 8 subregions, multivariate analysis of variance with the subregion as a repeated measure (RMANOVA) was performed for young and elderly women and men. To identify subregions with significantly different values, post-hoc contrast tests with significance level of $\alpha = 0.005$ were performed in order to control for the experiment-wise probability of making a Type I error. The significance of differences in the structural indices

between women and men as well as between young and elderly adults in each region were determined using Mann-Whitney U test with $\alpha = 0.05$. To examine the age-related changes in the trabecular structure indices in each region, linear regression analyses were performed for women and men of all ages. The Spearman's coefficient, ρ, was obtained for the correlation. Age-related changes in trabecular structure were compared in two subsets of the population: young adults aged 20-29 years and elderly adults aged 65-79 years. This age categorization was used in order to be consistent with previously published work by Khosla et al. and to provide a basis for comparison [8]. The significance of differences in the structural indices between young and elderly adults was determined using Mann-Whitney U test with $\alpha = 0.05$. All statistical tests were performed using JMP (version 7.0, SAS Institute Inc., Cary, NC).

III. RESULTS

Regional analysis was performed on HR-pQCT images of the distal radius and tibia of 146 healthy individuals (93 women and 53 men). **Table 5.1** summarizes the general description of the entire study population, as well as of the subsets (young and elderly women and men), including DXA-derived anthropometric data (height and weight), HR-pQCT-derived standard density measurements (vBMD, Tb.vBMD for the entire trabecular region, and the inner and outer subregions).

Table 5.1 General description of the population – mean ± SD of age, height, weight, BMD, and HR-pQCT-derived bone density indices at the distal radius and tibia for women and men.

	Women			Men			W vs. M (all ages)
	All Ages	Young (20-29 yrs)	Elderly (65-79 yrs)	All ages	Young (20-29 yrs)	Elderly (65-79 yrs)	% diff.
ANTHRO-POMETRIC DATA*							
N	53	7	11	25	5	4	
Height [cm]	161.1 ± 6.8	161.8 ± 5.0	156.1 ± 7.0	175.7 ± 7.5	182.4 ± 3.3	168.0 ± 4.9	-8[c]
Weight [kg]	64.1 ± 13.7	55.6 ± 5.6	60.0 ± 14.4	79.0 ± 15.6	82.4 ± 13.9	71.2 ± 16.8	-19[c]
RADIUS							
N	87	15	11	55	12	9	
Age [years]	49 ± 16	26 ± 3	72 ± 4	46 ± 16	25 ± 3	70 ± 3	-9
vBMD [mg HA/cm^3]	314.3 ± 62.3	345.2 ± 30.9	284.4 ± 49.6	332.6 ± 51.0	345.4 ± 43.7	306.6 ± 44.9	-5
Tb.vBMD [mg HA/cm^3]	150.4 ± 37.1	162.1 ± 34.0	136.2 ± 31.0	183.8 ± 36.5	205.8 ± 32.1	160.7 ± 17.4	-18[c]
Tb.vBMD$_{inn}$ [mg HA/cm^3]	108.8 ± 38.7	120.5 ± 36.8	94.9 ± 30.7	145.8 ± 38.8	169.8 ± 33.6	120.5 ± 17.3	-24[c]
Tb.vBMD$_{out}$ [mg HA/cm^3]	210.4 ± 36.2	221.9 ± 30.8	195.6 ± 35.1	239.0 ± 35.0	257.8 ± 30.8	219.0 ± 20.2	-11[c]
TIBIA							
N	93	17	13	53	13	9	
Age [years]	48 ± 16	27 ± 3	71 ± 4	45 ± 17	25 ± 3	70 ± 3	+11
vBMD [mg HA/cm^3]	296 ± 60	337.4 ± 45.7	247.3 ± 54.8	317.9 ± 55.5	360.5 ± 45.0	279.5 ± 40.5	-7[a]
Tb.vBMD [mg HA/cm^3]	155.6 ± 37.8	174.7 ± 29.7	130.6 ± 33.8	184.6 ± 42.1	221.2 ± 35.3	152.7 ± 26.6	-16[c]
Tb.vBMD$_{inn}$ [mg HA/cm^3]	110.6 ± 38.2	127.6 ± 30.7	86.8 ± 33.6	140.2 ± 43.3	176.2 ± 37.0	102.7 ± 24.7	-21[c]
Tb.vBMD$_{out}$ [mg HA/cm^3]	221.8 ± 39.4	243.8 ± 31.3	195.1 ± 36.8	250.0 ± 42.3	287.5 ± 35.1	226.5 ± 31.3	-11[c]

*N.B. Anthropometric data are obtained using Lunar Prodigy (GE Healthcare), and available only for a subset of the population

Significant difference in mean values with [a] $p < 0.05$; [b] $p < 0.01$; [c] $p < 0.001$, determined by Mann-Whitney U test.

1. Regional variations

Table 5.2 shows the mean values for BV/TV and Tb.N for young and elderly women and men in each region at the distal radius and tibia. Trabecular structure in the inner subregion had lower BV/TV, Tb.N, Tb.Th, and higher Tb.Sp and Tb.1/N.SD compared to the outer trabecular subregion at both distal radius and tibia regardless of gender and age. The

mean values for BV/TV and Tb.Th in the outer subregion were approximately twice as the value of the inner subregion at both distal radius and tibia for elderly adults (e.g. BV/TV = 0.163 ± 0.028 in the outer subregion vs. 0.078 ± 0.023 in the inner subregion at the radius for elderly women; $p < 0.001$). Tb.N and Tb.1/N.SD, however, were not significantly different between the inner and outer subregion at both distal radius and tibia regardless of gender and age group.

Figure 5.3 displays the mean percent differences from the global means in each subregion for all measured parameters for elderly women at their distal radius and tibia. In elderly women, BV/TV ranged from -40% in the IL subregion to +57% in the OP subregion with respect to the global mean at the distal radius, and from -59% in the IL subregion to +100% in the OM subregion at the distal tibia. Low BV/TV, Tb.N, and Tb.Th and high Tb.Sp and Tb.1/N.SD were found in the lateral subregions at the distal radius and in both IL and IA subregions at the distal tibia. In contrast, high BV/TV, Tb.N, and Tb.Th and low Tb.Sp and Tb.1/N.SD were found in the OA subregion at the radius and in both OM and OP subregions at the distal tibia. These trends were spatially similar but with slightly reduced magnitudes at both radius and tibia for young adults and for men.

2. Gender-specific regional variations

In general, women tended to have lower BV/TV, Tb.N and Tb.Th and higher Tb.Sp and Tb.1/N.SD (e.g. globally, in elderly women, BV/TV, Tb.N and Tb.Th were 15%, 10%, and 7% lower, than elderly men and Tb.Sp and Tb.1/N.SD were 15% and 28% higher, respectively, at the distal radius (p = NS except for BV/TV ($p < 0.05$) (**Table 5.2**); with similar to smaller magnitudes at the distal tibia). Gender differences in trabecular structure were stronger between young women and men compared to elderly adults at both distal

radius and tibia. The differences in Tb.N, Tb.Sp and Tb.1/N.SD were not significant except between young women and men at the distal tibia.

Figure 5.4 displays the mean percent differences in the trabecular structure indices for elderly women compared to elderly men in each subregion at the distal radius and tibia. Some regions showed larger differences in trabecular structure between women and men compared to the other regions. For instance, at the distal radius, while BV/TV was 15% lower for elderly women globally ($p = 0.048$), it was 28% lower in the IA subregion ($p < 0.05$) but only 6% lower in the OP subregion (p = NS). Similarly at the distal tibia, while BV/TV tended to be lower for elderly women by 14% globally (p = NS), it was 29% lower in the IA subregion ($p < 0.05$) but only 0.2% lower in the IP subregion (p = NS) (**Table 5.2** and **Figure 5.4**).

3. Age-related variations

Table 5.3 shows the correlations between the trabecular structure indices and age in each subregion for both women and men. In general, at both distal radius and tibia, BV/TV, Tb.N and Tb.Th correlated negatively with age while Tb.Sp and Tb.1/N.SD correlated positively. Trabecular structure in some regions had stronger and more significant correlations with age compared to the other regions. At the distal radius, the correlations tended to be stronger in the posterior and lateral subregions for women ($|\rho| \leq 0.47$) and in the posterior subregions for men ($|\rho| \leq 0.56$), but weaker in the OA subregion for both women and men ($|\rho| = 0.01$-0.12; all p = NS) (**Table 5.3**). At the distal tibia, the correlations between trabecular structure and age were stronger in the IA subregion for women and IL subregion for men ($|\rho| = 0.22$-0.59; all $p \leq 0.03$), but weaker in the outer subregions for both women and men ($|\rho| = 0.05$-0.44) (**Table 5.3**).

In order to further illustrate the difference in regional variation of trabecular bone structure between young and elderly adults, **Figure 5.5** maps the mean percent difference in the trabecular structure indices for elderly women compared to young women in each subregion at the distal radius and tibia. In general, elderly adults had lower BV/TV, Tb.N and Tb.Th and higher Tb.Sp and Tb.1/N.SD compared to young adults. Elderly adults had larger ranges of BV/TV and Tb.Th compared to young adults at both radius and tibia. For instance at the distal radius, BV/TV ranged from -40% in the IL subregion to +57% in the OP subregion with respect to the global mean for elderly women (**Figure 5.3**), while it ranged from -33% to +48% in the respective subregions for young women. The ranges of other indices remained comparable between elderly and young adults. Trabecular structure at some regions showed larger differences between young and elderly adults. At the distal radius, while BV/TV tended to be lower for elderly women by 16% globally ($p = NS$), it was 24% lower in the IP and IL subregions ($p < 0.05$ and NS, respectively) but 3% higher in the OA subregion ($p = NS$) compared to young women (**Table 5.2** and **Figure 5.5**). At the distal tibia, while BV/TV was 25% lower for elderly women globally ($p < 0.001$), it was 42% lower in the IA subregion ($p < 0.001$) but only 15% lower in the OM subregion compared to young women ($p < 0.01$) (**Table 5.2** and **Figure 5.5**). Similar patterns and degrees of differences in other trabecular structure indices between young and elderly adults were observed at both radius and tibia (**Figure 5.5**).

Table 5.2 Comparisons of the mean values for BV/TV and Tb.N between young and elderly women and men in each region at the distal radius and tibia.

BV/TV [1]	Women				Men				Women vs. Men			
	Mean ± SD		E vs. Y Differences		Mean ± SD		E vs. Y Differences		Young (20-29 yo)		Elderly (65-79 yo)	
	Young	Elderly	Abs.	%	Young	Elderly	Abs.	%	Abs.	%	Abs.	%
RADIUS												
N	15	11			12	9						
Global	0.135 ± 0.028	0.114 ± 0.026	-0.021	-16	0.172 ± 0.027	0.135 ± 0.014	-0.037	-22[b]	-0.036	-21[b]	-0.020	-15[a]
Inner	0.099 ± 0.030	0.078 ± 0.023	-0.021	-21	0.140 ± 0.029	0.099 ± 0.016	-0.041	-29[b]	-0.041	-29[b]	-0.021	-21
Outer	0.184 ± 0.025	0.163 ± 0.028	-0.021	-12	0.214 ± 0.025	0.181 ± 0.019	-0.032	-15[b]	-0.030	-14[a]	-0.019	-10[a]
Subregion IM	0.100 ± 0.031	0.081 ± 0.021	-0.019	-19	0.140 ± 0.033	0.108 ± 0.021	-0.032	-23[a]	-0.040	-29[b]	-0.027	-25[a]
IP	0.114 ± 0.035	0.087 ± 0.029	-0.027	-24[a]	0.158 ± 0.028	0.099 ± 0.029	-0.059	-38[b]	-0.045	-28[b]	-0.012	-12
IL	0.095 ± 0.032	0.072 ± 0.033	-0.023	-24	0.134 ± 0.032	0.090 ± 0.015	-0.045	-33[c]	-0.039	-29[a]	-0.018	-20
IA	0.083 ± 0.030	0.070 ± 0.021	-0.013	-15	0.119 ± 0.026	0.096 ± 0.024	-0.023	-19	-0.036	-31[b]	-0.026	-28[a]
OM	0.185 ± 0.027	0.172 ± 0.021	-0.013	-7	0.217 ± 0.031	0.199 ± 0.027	-0.018	-8	-0.032	-15[b]	-0.027	-14[a]
OP	0.219 ± 0.028	0.179 ± 0.039	-0.040	-18[a]	0.248 ± 0.023	0.191 ± 0.030	-0.057	-23[b]	-0.029	-12[a]	-0.012	-6
OL	0.172 ± 0.030	0.141 ± 0.043	-0.030	-18	0.200 ± 0.027	0.158 ± 0.020	-0.042	-21[b]	-0.029	-14	-0.017	-11
OA	0.166 ± 0.022	0.170 ± 0.022	+0.004	+3	0.192 ± 0.024	0.185 ± 0.018	-0.007	-4	-0.026	-14[b]	-0.015	-8
TIBIA												
N	17	13			12	9						
Global	0.146 ± 0.025	0.109 ± 0.028	-0.036	-25[c]	0.184 ± 0.029	0.127 ± 0.022	-0.057	-31[c]	-0.020	-15[b]	-0.018	-14
Inner	0.107 ± 0.025	0.073 ± 0.028	-0.034	-32[b]	0.147 ± 0.030	0.086 ± 0.021	-0.061	-42[c]	-0.029	-21[b]	-0.013	-15
Outer	0.202 ± 0.026	0.162 ± 0.031	-0.040	-20[c]	0.238 ± 0.030	0.188 ± 0.026	-0.050	-21[b]	-0.018	-8[a]	-0.027	-14
Subregion IM	0.140 ± 0.027	0.104 ± 0.026	-0.036	-26[b]	0.171 ± 0.030	0.113 ± 0.023	-0.058	-34[c]	-0.018	-11[a]	-0.009	-8
IP	0.103 ± 0.035	0.080 ± 0.030	-0.023	-22	0.144 ± 0.037	0.080 ± 0.029	-0.063	-44[b]	-0.029	-22[a]	-0.000	±0
IL	0.082 ± 0.030	0.050 ± 0.036	-0.032	-39[a]	0.129 ± 0.035	0.067 ± 0.029	-0.062	-48[b]	-0.037	-31[a]	-0.017	-25
IA	0.100 ± 0.026	0.058 ± 0.031	-0.042	-42[c]	0.146 ± 0.032	0.082 ± 0.018	-0.064	-44[c]	-0.035	-26[b]	-0.024	-29[a]
OM	0.249 ± 0.023	0.211 ± 0.032	-0.038	-15[b]	0.269 ± 0.036	0.227 ± 0.026	-0.042	-15[a]	-0.001	0.5	-0.016	-7
OP	0.190 ± 0.038	0.159 ± 0.030	-0.032	-17[a]	0.229 ± 0.032	0.176 ± 0.035	-0.053	-23[b]	-0.021	-10[a]	-0.017	-10
OL	0.172 ± 0.036	0.139 ± 0.038	-0.033	-19[a]	0.221 ± 0.032	0.169 ± 0.031	-0.052	-24[b]	-0.032	-16[b]	-0.030	-18[a]
OA	0.191 ± 0.031	0.138 ± 0.038	-0.052	-27[c]	0.233 ± 0.032	0.180 ± 0.030	-0.054	-23[b]	-0.025	-12[a]	-0.041	-23[a]

Tb.N [1/mm]	Women				Men				Women vs. Men			
	Mean ± SD		E vs. Y Differences		Mean ± SD		E vs. Y Differences		Young (20-29 yo)		Elderly (65-79 yo)	
	Young	Elderly	Abs.	%	Young	Elderly	Abs.	%	Abs.	%	Abs.	%
RADIUS												
N	15	11			12	9						
Global	1.88 ± 0.30	1.68 ± 0.26	-0.20	-11	2.03 ± 0.23	1.87 ± 0.26	-0.16	-8	-0.145	-7	-0.189	-10
Inner	1.83 ± 0.33	1.62 ± 0.26	-0.22	-12[a]	1.99 ± 0.23	1.79 ± 0.27	-0.19	-10	-0.158	-8	-0.179	-10
Outer	1.95 ± 0.26	1.77 ± 0.28	-0.18	-9	2.07 ± 0.24	1.96 ± 0.24	-0.11	-5	-0.120	-6	-0.193	-10
Subregion IM	1.88 ± 0.32	1.67 ± 0.25	-0.21	-11[a]	2.06 ± 0.24	1.90 ± 0.32	-0.16	-8	-0.182	-9	-0.226	-12
IP	1.90 ± 0.34	1.77 ± 0.27	-0.14	-7	2.04 ± 0.23	1.80 ± 0.27	-0.24	-12	-0.141	-7	-0.034	-2
IL	1.77 ± 0.36	1.55 ± 0.36	-0.21	-12	1.92 ± 0.25	1.72 ± 0.24	-0.21	-11	-0.157	-8	-0.166	-10
IA	1.75 ± 0.32	1.54 ± 0.24	-0.21	-12	1.88 ± 0.23	1.72 ± 0.35	-0.16	-8	-0.124	-7	-0.176	-10
OM	2.06 ± 0.29	1.93 ± 0.25	-0.14	-7	2.20 ± 0.28	2.15 ± 0.30	-0.05	-2	-0.137	-6	-0.219	-10
OP	2.06 ± 0.23	1.90 ± 0.32	-0.16	-8	2.11 ± 0.19	1.95 ± 0.24	-0.15	-7	-0.044	-2	-0.053	-3
OL	1.88 ± 0.29	1.65 ± 0.39	-0.23	-12	2.00 ± 0.24	1.84 ± 0.22	-0.16	-8	-0.121	-6	-0.189	-10
OA	1.83 ± 0.28	1.80 ± 0.26	-0.03	-1	1.97 ± 0.26	1.96 ± 0.28	-0.01	-1	-0.146	-7	-0.162	-8
TIBIA												
N	17	13			12	9						
Global	1.77 ± 0.23	1.52 ± 0.31	-0.25	-14[a]	2.17 ± 0.41[a]	1.61 ± 0.18	-0.56	-26[b]	-0.396	-18[a]	-0.083	-5
Inner	1.68 ± 0.25	1.41 ± 0.31	-0.27	-16[a]	2.10 ± 0.43[a]	1.46 ± 0.19	-0.64	-30[b]	-0.422	-20[a]	-0.049	-3
Outer	1.94 ± 0.19	1.73 ± 0.32	-0.21	-11[a]	2.29 ± 0.37[a]	1.89 ± 0.18	-0.40	-18[b]	-0.347	-15[a]	-0.156	-8
Subregion IM	1.76 ± 0.23	1.54 ± 0.30	-0.22	-12	2.10 ± 0.42	1.55 ± 0.16	-0.56	-26[b]	-0.346	-17	-0.009	-1
IP	1.73 ± 0.26	1.54 ± 0.35	-0.18	-11	2.21 ± 0.39[a]	1.56 ± 0.22	-0.65	-29[b]	-0.485	-22[b]	-0.019	-1
IL	1.65 ± 0.28	1.36 ± 0.36	-0.29	-18[a]	2.11 ± 0.45[a]	1.42 ± 0.25	-0.69	-33[b]	-0.457	-22[a]	-0.056	-4
IA	1.60 ± 0.29	1.28 ± 0.28	-0.33	-20[b]	2.01 ± 0.47	1.36 ± 0.19	-0.64	-32[b]	-0.403	-20	-0.089	-7
OM	1.98 ± 0.15	1.87 ± 0.32	-0.11	-6	2.24 ± 0.38[a]	1.96 ± 0.13	-0.28	-13[a]	-0.256	-11[a]	-0.081	-4
OP	1.99 ± 0.22	1.85 ± 0.32	-0.14	-7	2.45 ± 0.37[a]	2.03 ± 0.19	-0.42	-17[b]	-0.461	-19[b]	-0.178	-9
OL	1.91 ± 0.25	1.67 ± 0.37	-0.24	-13	2.33 ± 0.37[a]	1.86 ± 0.23	-0.47	-20[b]	-0.420	-18[a]	-0.190	-10
OA	1.90 ± 0.24	1.60 ± 0.35	-0.30	-16[a]	2.17 ± 0.37	1.74 ± 0.18	-0.43	-20[b]	-0.268	-12	-0.138	-8

Significant difference in mean values with [a]$p < 0.05$; [b]$p < 0.01$; [c]$p < 0.001$ using Mann-Whitney U test.

For graphical display of the differences in all examined structural indices at each region for elderly women compared to elderly men, see **Figure 5.4**. Similarly, for graphical display of the difference in structural indices at each region for elderly women compared to young women, see **Figure 5.5**.

Table 5.3 Spearman's correlation coefficients for the trabecular structure indices and age in each region for women (N = 93) and men (N = 53).

Spearman's	BV/TV		Tb.N		Tb.Th		Tb.Sp		Tb.1/N.SD	
ρ	Women	Men	Women	Men	Women	Men	Women	Men	Women	Men
RADIUS										
Global	-0.33[b]	-0.52[c]	-0.21	-0.19	-0.30[b]	-0.35[b]	0.24[a]	0.29[a]	0.21	0.27[a]
Inner	-0.30[b]	-0.51[c]	-0.24[a]	-0.22	-0.29[b]	-0.44[c]	0.25[a]	0.29[a]	0.21[a]	0.28[a]
Outer	-0.37[c]	-0.44[c]	-0.15	-0.13	-0.28[b]	-0.32[a]	0.19	0.24	0.13	0.20
Subregion IM	-0.23[a]	-0.40[b]	-0.19	-0.20	-0.19	-0.35[b]	0.21	0.26	0.17	0.25
IP	-0.35[c]	-0.56[c]	-0.17	-0.22	-0.39[c]	-0.53[c]	0.21	0.36[b]	0.21	0.30[a]
IL	-0.33[b]	-0.50[c]	-0.23[a]	-0.23	-0.34[b]	-0.46[c]	0.25[a]	0.30[a]	0.18	0.30[a]
IA	-0.14	-0.35[b]	-0.21	-0.17	-0.09	-0.29[a]	0.20	0.22	0.16	0.22
OM	-0.24[a]	-0.27[a]	-0.09	-0.11	-0.15	-0.18	0.12	0.18	0.06	0.16
OP	-0.43[c]	-0.56[c]	-0.11	-0.15	-0.47[c]	-0.47[c]	0.19	0.32[a]	0.06	0.23
OL	-0.41[c]	-0.46[c]	-0.21	-0.16	-0.37[c]	-0.38[b]	0.26[a]	0.30[a]	0.21[a]	0.28[a]
OA	0.05	-0.12	0.02	-0.03	0.01	-0.12	-0.02	0.06	-0.08	0.11
TIBIA										
Global	-0.42[c]	-0.61[c]	-0.20[a]	-0.51[c]	-0.38[c]	-0.17	0.24[a]	0.56[c]	0.24[a]	0.55[c]
Inner	-0.39[c]	-0.62[c]	-0.21[a]	-0.53[c]	-0.43[c]	-0.37[b]	0.24[a]	0.57[c]	0.23[a]	0.54[c]
Outer	-0.43[c]	-0.53[c]	-0.17	-0.44[b]	-0.30[b]	-0.14	0.22[a]	0.50[c]	0.17	0.51[c]
Subregion IM	-0.39[c]	-0.54[c]	-0.17	-0.48[c]	-0.38[c]	-0.23	0.22[a]	0.52[c]	0.20	0.50[c]
IP	-0.28[b]	-0.58[c]	-0.13	-0.51[c]	-0.31[b]	-0.37[b]	0.16	0.57[c]	0.17	0.54[c]
IL	-0.33[b]	-0.59[c]	-0.22[a]	-0.53[c]	-0.35[c]	-0.42[b]	0.23[a]	0.54[c]	0.22[a]	0.53[c]
IA	-0.40[c]	-0.57[c]	-0.26[a]	-0.48[c]	-0.39[c]	-0.32[a]	0.28[b]	0.50[c]	0.25[a]	0.48[c]
OM	-0.35[c]	-0.41[b]	-0.10	-0.36[b]	-0.32[b]	-0.16	0.15	0.42[b]	0.05	0.44[c]
OP	-0.33[b]	-0.46[c]	-0.10	-0.42[b]	-0.30[b]	-0.17	0.14	0.49[c]	0.19	0.51[c]
OL	-0.30[b]	-0.54[c]	-0.17	-0.45[c]	-0.22[a]	-0.15	0.20	0.52[c]	0.19	0.52[c]
OA	-0.42[c]	-0.53[c]	-0.21[a]	-0.42[b]	-0.30[b]	-0.12	0.25[a]	0.50[c]	0.12	0.49[c]

Significant correlation with age (ρ) with [a] $p < 0.05$; [b] $p < 0.01$; and [c] $p < 0.001$.

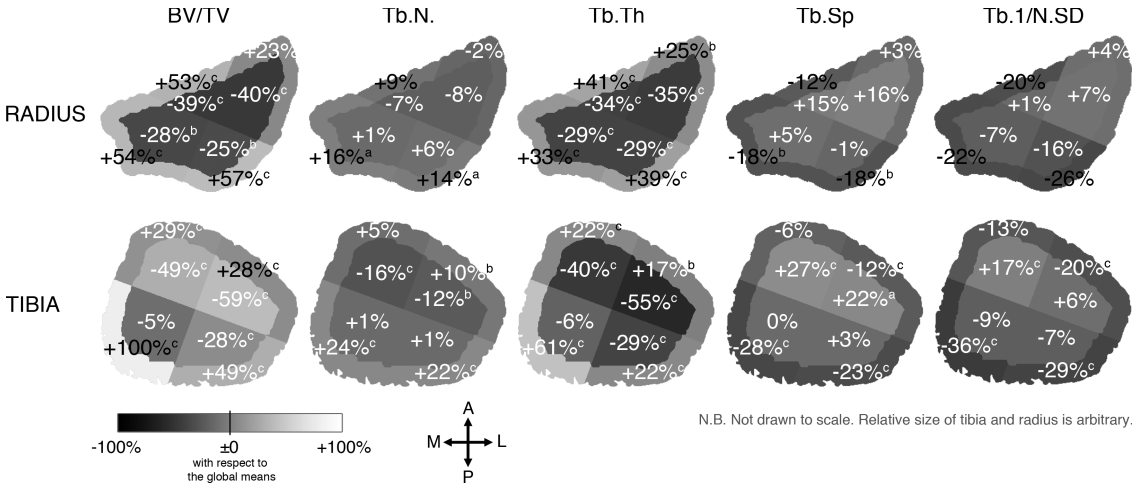

Figure 5.3 The mean percent difference from the global means in each subregion for each structure index for elderly women at the distal radius (top) and tibia (bottom). Similar patterns were observed for elderly men and young adults. Significant difference from the global mean with $^{a}p < 0.005$; $^{b}p < 0.001$ determined by multivariate RMANOVA and post-hoc contrast test.

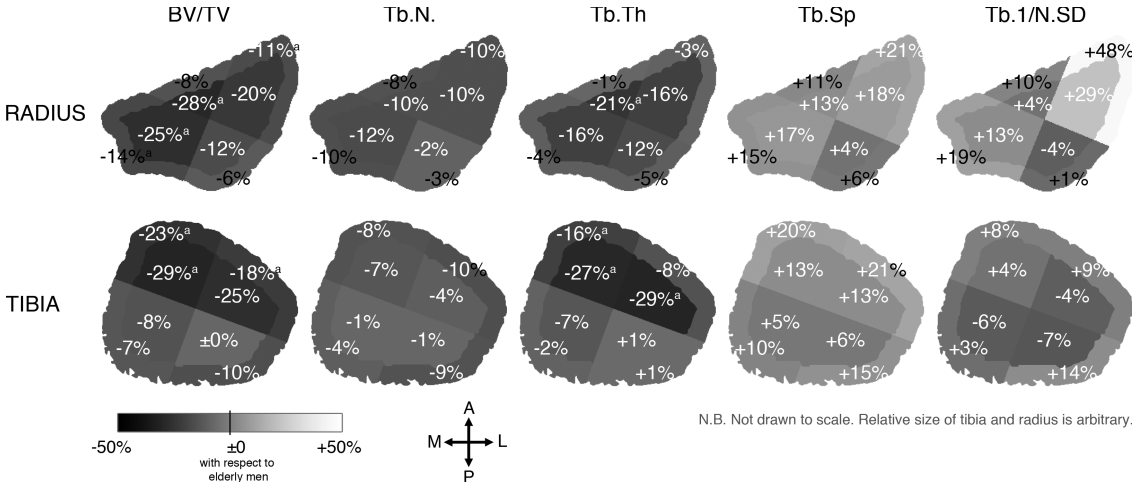

Figure 5.4 The mean percent difference in the trabecular structure indices for elderly women (N = 13) compared to elderly men (N = 9) in each subregion at the distal radius (top) and tibia (bottom). Significant difference from elderly men with $^{a}p < 0.05$; $^{b}p < 0.01$ $^{c}p < 0.001$ using Mann–Whitney U test.

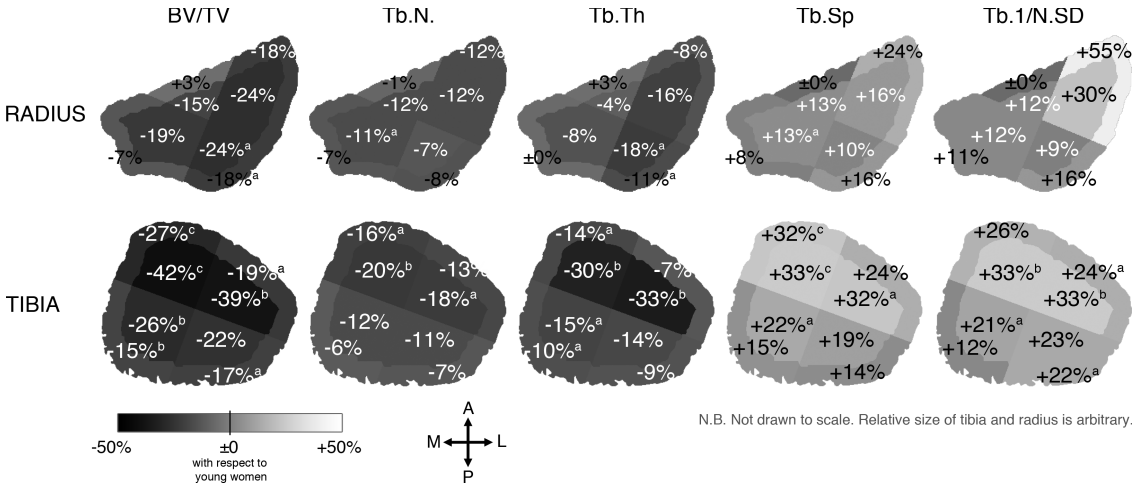

Figure 5.5 The mean percent difference in the trabecular structure indices for elderly women (N = 13) compared to young women (N = 17) in each subregion at the distal radius (top) and tibia (bottom). Significant difference from young women with $^{a}p < 0.05$; $^{b}p < 0.01$ $^{c}p < 0.001$ using Mann–Whitney U test.

IV. Discussion

The results of this study highlight the substantial regional variability of trabecular bone structure in the distal radius and tibia, which is obscured by the conventional analysis that reports only the global average value and the standard deviation across the entire trabecular compartment. BV/TV, Tb.N, Tb.Th, Tb.Sp, and Tb.1/N.SD were examined regionally from the HR-pQCT images of the distal radius and tibia of 146 healthy individuals aged from 20-79 years. Our major findings are (1) trabecular bone structure varies dramatically across the cross-section at the distal radius and tibia (e.g. -40% to +57% and -59% to +100% of the global means in BV/TV at the distal radius and tibia, respectively, for elderly women), (2) the gender differences in trabecular structure are more prominent in the IA subregion at the radius as well as tibia compared to the other regions or the global mean differences, and (3) the age-related differences are more prominent in the IP subregion for the radius and in both IL and IA subregions for the tibia compared to the other regions or the global mean differences.

The cross-sectional variations between the subregions observed in this study were substantially larger than the longitudinal variations along the 9-mm span of the scanning section at the distal radius and tibia [18]. For example for elderly women at the distal radius, Tb.N varied from 8% less than the global value (in the IL subregion) to 16% more (in the OM subregion), with the net mean difference of 0.39 mm^{-1}; at the distal tibia, Tb.N varied from 16% less than the global value (in the IA subregion) to 24% more (in the OM subregion) with the net mean difference of 0.59 mm^{-1}. The difference in the global mean of Tb.N between the proximal and distal ends of the scanning section, however, is roughly 0.05 mm^{-1} [18] and 0.17-0.23 mm^{-1} at the distal radius and tibia, respectively [18, 19]. One implication of this result is the importance of a careful and standardized procedure for selecting a region to take virtual bone biopsy [20, 21] for meaningful comparison across cross-section and between subjects. Assuming bone status of a larger region from that of its smaller subregion using may introduce a confounding sampling error.

One possible explanation for the observed regional variability is the local biomechanical environment, particularly for the tibia as it is a site that is habitually loaded. During gait, the peak force is experienced at the heel [22]. Consequently, substantial compressive and shear forces are imposed on the medial and posterior part of the distal tibia due to the ground reaction force as well as internal muscle forces [2, 3, 23]. Wolff's law dictates that the bone mass and structure adapt to the mechanical loading patterns it is under [24-28]. In addition, trabecular structural indices correlate well with the tissue-level mechanical property [29-33]. As trabecular compartment carries 35-71% of axial loads at this distal section [31], trabecular bone structure is, therefore, expected to have adapted to meet the local biomechanical environment. Indeed, the OM and OP subregions featured greater trabecular bone volume with more numerous, thicker trabeculae with reduced separation and heterogeneity (**Figure 5.3**). It also coincides with the area of high

compressive strength measured using osteopenetrometer [34], as well as the most frequent sites for stress fracture among runners [35-38].

The results of regional analysis can provide additional information that was obscured using the conventional global approach. For example, for fall that typically results in a Colles' fracture, the ground reaction force results in a considerable dorsal and lateral compressive to the distal radius [39]. Consequently, strain energy density is elevated at the medial and posterior (dorsal) regions [33]. Coincidentally, the results of this study revealed that trabeculae in the IM and IP subregions are structural vulnerable, particularly for women and elderly adults. Indeed, fracture initiation is observed at these regions under simulated axial and off-axis loading [40], respectively. In combination with fall kinetics measurements, regional analysis can bring underlying local bone property, thereby contributed in elucidating the fracture risk as well as developing preventive strategy.

This study contributed in understanding of the age-related alteration in bone structure by providing spatial and anatomical information. Because the inner trabecular subregion has substantially lower BV/TV and Tb.Th compared to the global mean values regardless of gender, age group or site (**Table 5.2** and **Figure 5.3**), it is not a surprise that the age-related deterioration of trabecular structure is more apparent in this region than the outer subregion. The effect is particularly severe for women, as reduced estrogen levels upon menopause leads to loss of bone mass by decreases in BV/TV, Tb.Th, and Tb.N as well as an increase in Tb.Sp [41-47]. Our results are consistent with pronounced bone deterioration in the inner subregion observed in ovariectomized rats [48, 49]. For men, on the other hand, age-related alterations in trabecular structure were site-dependent, partially in agreement with Khosla et al [8]. At the distal radius, the age-related decrease in BV/TV was driven by strong overall trabecular thinning particularly in the IP and IL subregions. At the distal tibia, on the other hand, it was driven by trabecular disruption

evenly across the trabecular compartment. In fact, there exists disagreement in the literature with regard to the age-related alteration in trabecular bone structure at the distal radius and tibia for men: Mueller et al [19, 50] reported significant negative correlations with age for both Tb.N and Tb.Th at the distal radius; Dalzell et al [6] reported a lack of correlation with age for any trabecular structure indices at either site. These discrepancies may be attributed to the complex hormonal interplay involving estrogen [51-53], serum bioavailable estradiol [45], and IGF-I levels [44]. The study design such as *in vivo* versus *ex vivo* images, use of a prototype HR-pQCT [19], and the difference in the study populations, along with many other factors likely contribute to the significant variability in the measures. Clearly, further investigation on the gender difference in age-related changes of trabecular structure at the distal tibia and radius is called for.

There are some limitations in the study design that are worth mentioning. First, the definition of regions employed in this study was arbitrary. However, it was systematic, consistent with anatomical coordinate system, and unaffected by patient positioning. The measurement location was set with a fixed distance (9.2 mm for radius and 22.5 mm for tibia) from the endplate consistent with the standard *in vivo* protocol regardless of bone length. These locations are known to have variable proportions of cortical and trabecular bone [54] and load sharing [31] for both radius and tibia. As cortical bone is an integral part, regional variations in cortical density and structure are expected. In fact, substantial regional variations in cortical vBMD along the shaft of the tibia measured by the pQCT have been reported [55, 56]. Thorough investigation of the regional variation in cortical vBMD, thickness, and area, as well as regional variation in load sharing using finite element analysis on the same dataset using HR-pQCT are currently in progress. In addition, acquiring images at the fixed distance from the endplate disregards individual body size, which has a substantial effect on bone property [5, 57]. Sekhon et al [58] reported

substantial errors in density measures calculated from HR-pQCT images, related to the cortical geometry and trabecular density. This may be due to beam hardening and scatter. Such effect may confound region-wise comparisons, though this is likely limited to differences between inner and outer sub-regions. The cross-sectional study design in a multi-ethnic population with relatively small sample sizes may compromise the statistical power. In the future, regional differences in age-related changes of trabecular structure at the distal radius and tibia need to be examined in a larger cross-sectional and a longitudinal studies.

In conclusion, this study has provided a basis for understanding the regional variation in trabecular bone structure at the distal radius and tibia. Knowing such intrinsic variability in trabecular structure is critical in interpreting data. But the conventional global analysis may obscure regional differences. Similarly, assuming bone status of a larger region from that of its smaller subregion using virtual bone biopsy [21] may introduce a confounding sampling error. Therefore, a combined approach that investigates entire region, each subregion, and the cortical compartment may offer more complete information. Applying the proposed regional analysis can provide additional spatial and anatomical information to understanding of the bone status.

REFERENCES

[1] Osteoporosis prevention, diagnosis, and therapy. NIH Consens Statement 2000; 17: 1-45.

[2] Liu XS, Zhang XH, Sekhon KK, Adam MF, McMahon DJ, Bilezikian JP, Shane E, Guo XE. High-Resolution Peripheral Quantitative Computed Tomography Can Assess Microstructural and Mechanical Properties of Human Distal Tibial Bone. J Bone Miner Res 2009.

[3] MacNeil JA, Boyd SK. Accuracy of high-resolution peripheral quantitative computed tomography for measurement of bone quality. Med Eng Phys 2007; 29: 1096-105.

[4] Sode M, Burghardt AJ, Nissenson RA, Majumdar S. Resolution dependence of the non-metric trabecular structure indices. Bone 2008; 42: 728-36.

[5] MacNeil JA, Boyd SK. Load distribution and the predictive power of morphological indices in the distal radius and tibia by high resolution peripheral quantitative computed tomography. Bone 2007; 41: 129-37.

[6] Boutroy S, Bouxsein ML, Munoz F, Delmas PD. In vivo assessment of trabecular bone microarchitecture by high-resolution peripheral quantitative computed tomography. J Clin Endocrinol Metab 2005; 90: 6508-15.

[7] Boutroy S, Van Rietbergen B, Sornay-Rendu E, Munoz F, Bouxsein ML, Delmas PD. Finite element analysis based on in vivo HR-pQCT images of the distal radius is associated with wrist fracture in postmenopausal women. J Bone Miner Res 2008; 23: 392-9.

[8] Melton LJ, 3rd, Riggs BL, van Lenthe GH, Achenbach SJ, Muller R, Bouxsein ML, Amin S, Atkinson EJ, Khosla S. Contribution of in vivo structural measurements and load/strength ratios to the determination of forearm fracture risk in postmenopausal women. J Bone Miner Res 2007; 22: 1442-8.

[9] Radspieler H, Frieling I, Dambacher MA, Neff M. In Vivo Assessment of 3-Dimensional Bone Micro Architecture with HR-pQCT in Patients With and Without Fractures. In: 30th Annual Meeting of the American Society for Bone and Mineral Research. Montréal, Quebéc, Canada; 2008.

[10] Lai YM, Qin L, Yeung HY, Lee KK, Chan KM. Regional differences in trabecular BMD and micro-architecture of weight-bearing bone under habitual gait loading--a pQCT and microCT study in human cadavers. Bone 2005; 37: 274-82.

[11] Sasimontonkul S, Bay BK, Pavol MJ. Bone contact forces on the distal tibia during the stance phase of running. J Biomech 2007; 40: 3503-9.

[12] Wehner T, Claes L, Simon U. Internal loads in the human tibia during gait. Clin Biomech (Bristol, Avon) 2009; 24: 299-302.

[13] Laib A, Hammerle S, Koller B. A new 100 μm resolution scanner for in vivo 3D-CT of the human forearm and lower leg. In: 16th International Bone Densitometry Workshop. Annecy, France; 2004.

[14] Dalzell N, Kaptoge S, Morris N, Berthier A, Koller B, Braak L, van Rietbergen B, Reeve J. Bone micro-architecture and determinants of strength in the radius and tibia: age-related changes in a population-based study of normal adults measured with high-resolution pQCT. Osteoporos Int 2009; 20: 1683-94.

[15] Kazakia GJ, Hyun B, Burghardt AJ, Krug R, Newitt DC, de Papp AE, Link TM, Majumdar S. In vivo determination of bone structure in postmenopausal women: a comparison of HR-pQCT and high-field MR imaging. J Bone Miner Res 2008; 23: 463-74.

[16] Khosla S, Riggs BL, Atkinson EJ, Oberg AL, McDaniel LJ, Holets M, Peterson JM, Melton LJ, 3rd. Effects of sex and age on bone microstructure at the ultradistal radius: a population-based noninvasive in vivo assessment. J Bone Miner Res 2006; 21: 124-31.

[17] Laib A, Hauselmann HJ, Ruegsegger P. In vivo high resolution 3D-QCT of the human forearm. Technol Health Care 1998; 6: 329-37.

[18] MacNeil JA, Boyd SK. Improved reproducibility of high-resolution peripheral quantitative computed tomography for measurement of bone quality. Med Eng Phys 2008; 30: 792-9.

[19] Sornay-Rendu E, Boutroy S, Munoz F, Delmas PD. Alterations of cortical and trabecular architecture are associated with fractures in postmenopausal women, partially independent of decreased BMD measured by DXA: the OFELY study. J Bone Miner Res 2007; 22: 425-33.

[20] Vico L, Zouch M, Amirouche A, Frère D, Laroche N, Koller B, Laib A, Thomas T, Alexandre C. High-Resolution pQCT Analysis at the Distal Radius and Tibia Discriminates Patients With Recent Wrist and Femoral Neck Fractures. Journal of Bone and Mineral Research 2008; 23: 1741-1750.

[21] Dalzell N, Kaptoge S, Morris N, Berthier A, Koller B, Braak L, van Rietbergen B, Reeve J. Bone micro-architecture and determinants of strength in the radius and tibia: age-related changes in a population-based study of normal adults measured with high-resolution pQCT. Osteoporos Int 2009.

[22] Laib A, Ruegsegger P. Calibration of trabecular bone structure measurements of in vivo three-dimensional peripheral quantitative computed tomography with 28-microm-resolution microcomputed tomography. Bone 1999; 24: 35-9.

[23] Muller R, Hildebrand T, Hauselmann HJ, Ruegsegger P. In vivo reproducibility of three-dimensional structural properties of noninvasive bone biopsies using 3D-pQCT. J Bone Miner Res 1996; 11: 1745-50.

[24] Laib A, Newitt DC, Lu Y, Majumdar S. New model-independent measures of trabecular bone structure applied to in vivo high-resolution MR images. Osteoporos Int 2002; 13: 130-6.

[25] Boyd SK. Site-specific variation of bone micro-architecture in the distal radius and tibia. J Clin Densitom 2008; 11: 424-30.

[26] Mueller TL, van Lenthe GH, Stauber M, Gratzke C, Eckstein F, Muller R. Regional, age and gender differences in architectural measures of bone quality and their correlation to bone mechanical competence in the human radius of an elderly population. Bone 2009; 45: 882-91.

[27] Gomberg BR, Wehrli FW, Vasilic B, Weening RH, Saha PK, Song HK, Wright AC. Reproducibility and error sources of micro-MRI-based trabecular bone structural parameters of the distal radius and tibia. Bone 2004; 35: 266-76.

[28] Wehrli F, Saha P, Gomberg B, Song H. Noninvasive assessment of bone architecture by magnetic resonance micro-imaging-based virtual bone biopsy. Proceedings of the IEEE 2003; 91: 1520-1542.

[29] Cheung JT, Zhang M, Leung AK, Fan YB. Three-dimensional finite element analysis of the foot during standing--a material sensitivity study. J Biomech 2005; 38: 1045-54.

[30] Anderson DD, Goldsworthy JK, Shivanna K, Grosland NM, Pedersen DR, Thomas TP, Tochigi Y, Marsh JL, Brown TD. Intra-articular contact stress distributions at the ankle throughout stance phase-patient-specific finite element analysis as a metric of degeneration propensity. Biomech Model Mechanobiol 2006; 5: 82-9.

[31] Carter DR, Orr TE, Fyhrie DP. Relationships between loading history and femoral cancellous bone architecture. J Biomech 1989; 22: 231-44.

[32] Fernandes P, Rodrigues H, Jacobs C. A Model of Bone Adaptation Using a Global Optimisation Criterion Based on the Trajectorial Theory of Wolff. Comput Methods Biomech Biomed Engin 1999; 2: 125-138.

[33] Lanyon LE, Rubin CT. Static vs dynamic loads as an influence on bone remodelling. J Biomech 1984; 17: 897-905.

[34] Skedros JG, Baucom SL. Mathematical analysis of trabecular 'trajectories' in apparent trajectorial structures: the unfortunate historical emphasis on the human proximal femur. J Theor Biol 2007; 244: 15-45.

[35] Wolff J. The Law of Bone Remodeling (Das Gesetz der transformation der knochen). Berlin: Springer; 1892.

[36] Bevill G, Eswaran SK, Gupta A, Papadopoulos P, Keaveny TM. Influence of bone volume fraction and architecture on computed large-deformation failure mechanisms in human trabecular bone. Bone 2006; 39: 1218-25.

[37] Liu XS, Sajda P, Saha PK, Wehrli FW, Guo XE. Quantification of the roles of trabecular microarchitecture and trabecular type in determining the elastic modulus of human trabecular bone. J Bone Miner Res 2006; 21: 1608-17.

[38] Mittra E, Rubin C, Gruber B, Qin YX. Evaluation of trabecular mechanical and microstructural properties in human calcaneal bone of advanced age using mechanical testing, muCT, and DXA. J Biomech 2007.

[39] Ulrich D, van Rietbergen B, Laib A, Ruegsegger P. Load transfer analysis of the distal radius from in-vivo high-resolution CT-imaging. J Biomech 1999; 32: 821-8.

[40] Hvid I, Rasmussen O, Jensen NC, Nielsen S. Trabecular bone strength profiles at the ankle joint. Clin Orthop Relat Res 1985: 306-12.

[41] Bennell KL, Brukner PD. Epidemiology and site specificity of stress fractures. Clin Sports Med 1997; 16: 179-96.

[42] Boden BP, Osbahr DC, Jimenez C. Low-risk stress fractures. Am J Sports Med 2001; 29: 100-11.

[43] Brukner P, Bradshaw C, Khan KM, White S, Crossley K. Stress fractures: a review of 180 cases. Clin J Sport Med 1996; 6: 85-9.

[44] Daffner RH, Pavlov H. Stress fractures: current concepts. AJR Am J Roentgenol 1992; 159: 245-52.

[45] Troy KL, Grabiner MD. Asymmetrical ground impact of the hands after a trip-induced fall: experimental kinematics and kinetics. Clin Biomech (Bristol, Avon) 2007; 22: 1088-95.

[46] Troy KL, Grabiner MD. Off-axis loads cause failure of the distal radius at lower magnitudes than axial loads: a finite element analysis. J Biomech 2007; 40: 1670-5.

[47] Akhter MP, Lappe JM, Davies KM, Recker RR. Transmenopausal changes in the trabecular bone structure. Bone 2007; 41: 111-6.

[48] Brouwers JE, Lambers FM, van Rietbergen B, Ito K, Huiskes R. Comparison of bone loss induced by ovariectomy and neurectomy in rats analyzed by in vivo micro-CT. J Orthop Res 2009; 27: 1521-7.

[49] Jiang SD, Shen C, Jiang LS, Dai LY. Differences of bone mass and bone structure in osteopenic rat models caused by spinal cord injury and ovariectomy. Osteoporos Int 2007; 18: 743-50.

[50] Khosla S, Melton LJ, 3rd, Achenbach SJ, Oberg AL, Riggs BL. Hormonal and biochemical determinants of trabecular microstructure at the ultradistal radius in women and men. J Clin Endocrinol Metab 2006; 91: 885-91.

[51] Khosla S, Riggs BL, Robb RA, Camp JJ, Achenbach SJ, Oberg AL, Rouleau PA, Melton LJ, 3rd. Relationship of volumetric bone density and structural parameters at different skeletal sites to sex steroid levels in women. J Clin Endocrinol Metab 2005; 90: 5096-103.

[52] Riggs BL, Khosla S, Melton LJ, 3rd. Sex steroids and the construction and conservation of the adult skeleton. Endocr Rev 2002; 23: 279-302.

[53] Yang J, Pham SM, Crabbe DL. High-resolution Micro-CT evaluation of mid- to long-term effects of estrogen deficiency on rat trabecular bone. Acad Radiol 2003; 10: 1153-8.

[54] Bagi CM, Ammann P, Rizzoli R, Miller SC. Effect of estrogen deficiency on cancellous and cortical bone structure and strength of the femoral neck in rats. Calcif Tissue Int 1997; 61: 336-44.

[55] Ito M, Nishida A, Nakamura T, Uetani M, Hayashi K. Differences of three-dimensional trabecular microstructure in osteopenic rat models caused by ovariectomy and neurectomy. Bone 2002; 30: 594-8.

[56] Khosla S, Melton LJ, 3rd, Riggs BL. Clinical review 144: Estrogen and the male skeleton. J Clin Endocrinol Metab 2002; 87: 1443-50.

[57] Khosla S, Atkinson EJ, Dunstan CR, O'Fallon WM. Effect of estrogen versus testosterone on circulating osteoprotegerin and other cytokine levels in normal elderly men. J Clin Endocrinol Metab 2002; 87: 1550-4.

[58] Gennari L, Nuti R, Bilezikian JP. Aromatase activity and bone homeostasis in men. J Clin Endocrinol Metab 2004; 89: 5898-907.

[59] Schlenker RA, VonSeggen WW. The distribution of cortical and trabecular bone mass along the lengths of the radius and ulna and the implications for in vivo bone mass measurements. Calcif Tissue Res 1976; 20: 41-52.

[60] Cooper DM, Ahamed Y, Macdonald HM, McKay HA. Characterising cortical density in the mid-tibia: intra-individual variation in adolescent girls and boys. Br J Sports Med 2008; 42: 690-5.

[61] Lai YM, Qin L, Hung VW, Chan KM. Regional differences in cortical bone mineral density in the weight-bearing long bone shaft--a pQCT study. Bone 2005; 36: 465-71.

[62] Sekhon K, Kazakia GJ, Burghardt AJ, Hermannsson B, Majumdar S. Accuracy of volumetric bone mineral density measurement in high-resolution peripheral quantitative computed tomography. Bone 2009; 45: 473-9.

Chapter 6 – Clinical Application of Subregional Analysis

I. INTRODUCTION

Osteoporosis is a skeletal disorder manifested by compromised bone strength and resulting in an increased risk of fracture that currently affects more than 10 million people in the United States [1]. Osteoporosis is currently diagnosed based on the areal bone mineral density (aBMD) obtained using dual x-ray absorptiometry (DXA). The fact that it explains up to 70% of bone strength and cannot account for all osteoporotic fractures highlights the multifactorial and complex nature of fracture risk assessment. DXA-obtained aBMD is in fact limited as both detailed three-dimensional geometry as well as trabecular structure information are obscured. Due to its large surface area available for turnover, trabecular bone structure is expected to be more responsive to the changes in the local environment. Moreover, by combining information on trabecular structure with densitometric measurements, an increased proportion of bone strength can be explained [2-5]. Therefore, trabecular structure has received research interests, such as for monitoring progression of bone related disease as well as evaluating the efficacy of therapeutic interventions. Using high-resolution peripheral quantitative computed tomography (HR-pQCT), a nominal resolution of 82 μm can be achieved in vivo, enabling the assessment of 3D trabecular microarchitecture noninvasively. Its discriminatory power for fracture risks has been shown at various sites [6-9], raising its potential as an effective tool for research clinical use.

Alendronate is among a class of anti-resorptive drugs called bisphosphonates commonly used for treating osteoporosis. Anti-resorptive agents decrease bone turnover rate by inhibiting bone resorption via promoting osteoclast apoptosis [10]. Bisphosphonates increase BMD at the spine and hip [11, 12], however, only account for a

small percentage (~20%) of reduction in vertebral fracture risk [11, 13]. Moreover, alendronate-induced increases in DXA-aBMD at clinically relevant sites including the wrist at 2.5 years have been found to be associated with a decrease in biochemical markers for bone turnover at 6 month [12].

As exhibited in the previous chapter, substantial variability in trabecular bone structure across the cross-section at the distal end of radius and tibia is evident [14]. For instance for elderly women, bone volume fraction (BV/TV) and trabecular number (Tb.N) were 40% and 8% less in the inner-lateral (IL) subregion of the distal radius, respectively, and 59% and 12% less in the IL subregion of the tibia, respectively, compared to the global mean values (calculated for the entire trabecular compartment). Furthermore, the age-related differences are more prominent in the inner-posterior (IP) subregion for the radius and in both the IL and inner-anterior (IA) subregions for the tibia, compared to the other regions or the global mean differences between young and elderly adults [14] (**Figure 6.1**). Therefore, the conventional analysis that examines only the global mean value may overlook such regional variations in trabecular bone structure, thereby obscures the changes that may have more clinical relevance. Subregional analysis may show differences with greater magnitude between the treatment and placebo groups at a specific region, or may allow earlier detection of therapy-induced changes compared to the global analysis.

To examine the potency of subregional analysis in a clinical study, it was applied to a double-blinded, placebo-controlled randomized pilot study that explored the association between biochemical marker for bone turnover and changes in bone geometric, microarchitectural and biomechanical properties in post-menopausal osteopenic women at the distal radius and tibia using HR-pQCT. The goal of the original longitudinal study was two-fold: 1) to compare the densitometric, geometric, micro-architectural, and biomechanical (determined by micro-finite element analysis, μFEA) indices between the

subjects treated with alendronate for 2 years and placebo, 2) to correlate the baseline values of the bone structure with the changes in bone turnover biomarkers as well as in biomechanical indices [15]. This chapter focuses on subregional analysis of the former, the comparison of the densitometric, geometric, and micro-architectural indices between the subjects treated with alendronate for 2 years and placebo. We hypothesize that regions with low bone mass, such as the IL subregion of both the distal radius and tibia, may be more sensitive to alendronate-induced changes in the cortical and trabecular densitometric and structural indices.

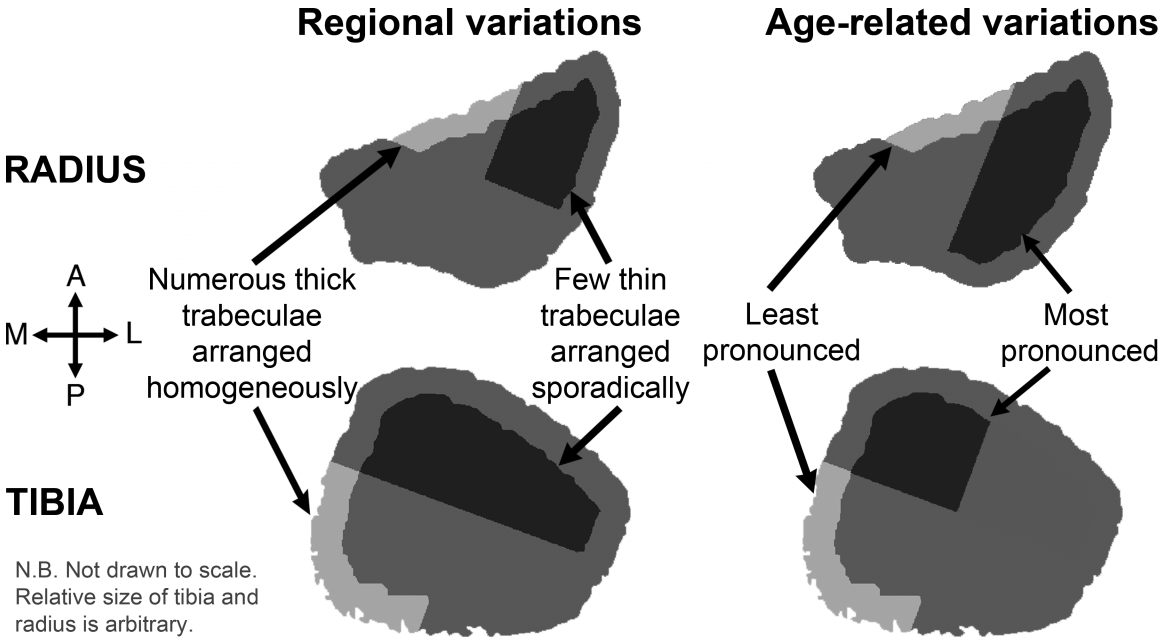

Figure 6.1 Summary of regional variations for elderly women (65-79 years old) and age-related regional variations at the distal radius and tibia for women. In the subregion with most pronounced age-related effect, not only the trabecular sturcutre indices are strongly correlated to age, but also BV/TV is significantly lower for elderly women compared to young women (20-29 years old) [14].

II. MATERIALS AND METHODS

1. Subjects

A total of 53 early post-menopausal osteopenic women, ranging from 45 to 65 years old (average age was 55.6 years old), participated in this longitudinal study. They were post-menopausal for at least a year but no more than 6 years. Their bone status

(osteopenia) was determined by t-score (ranged -1.1 to -2.5) of DXA-obtained aBMD values at either the lumber spine, the total proximal femur, trochanter, or neck, according to the world health organization (WHO) criteria [16]. Twenty-six women were randomly assigned to the treatment group (70 mg alendronate once weekly and daily 2800 IU of vitamin D3 and OScal+D (1000 mg calcium + 400 IU vitamin D3)) and 27 women into placebo (daily 2800 IU vitamin D3 and OScal+D) groups.

Exclusion criteria were a history of fracture after age 50; any disease condition that could play a significant role in the development of osteoporosis (e.g. idiopathic osteoporosis, immobilization, hyperthyroidism) or those which may affect bone metabolism (e.g. alcoholism or chronic drug use, chronic gastrointestinal disease, renal or hepatic impairment); receiving chronic treatment that is known to affect bone turnover rate (e.g. antacids, adrenal or anabolic steroids, anticonvulsants or anticoagulants, thiazides, pharmacological doses of Vitamin A or D supplements), and estrogen usage in the past 6 months; a history of fluoride, calcitonin, or tamoxifen use. Those failing to meet DXA, QCT, HR-pQCT, and magnetic resonance imaging (MRI) safety guidelines (e.g. a metal implant, pacemaker, claustrophobia) were excluded as well. All subjects gave written informed consent prior to participation. The study protocol was approved by the University of California San Francisco Committee on Human Research.

2. HR-pQCT image acquisition

Subjects were imaged in a clinical HR-pQCT system (XtremeCT, Scanco Medical AG, Brüttisellen, Switzerland) using the manufacturer's standard in vivo protocol described in previous patient studies [7-9, 17-20]. Each subject's forearm and lower leg were immobilized in corresponding carbon-fiber molds, and fixed to the scanner to minimize motion during acquisition. A 9.02-mm-long section (110 slices) of the radius and tibia was imaged. The imaged section starts at 9.5 mm and 22.5 mm proximal to the distal endplate,

respectively, and extends proximally. The non-dominant side was scanned unless there was a history of fracture, in which case, the contra-lateral side was scanned. The x-ray source potential was 60 kVp with a current of 900 μA. A two-dimensional detector containing 3072 × 256 CCD elements was used to acquire 750 projections over 180 degrees with a 100 ms integration time per angular position. The 12.6 cm field of view was reconstructed across a 1536 × 1536 matrix, yielding 82 μm isotropic voxels. Image acquisition time was 3 minutes per scan. Images were immediately reviewed for motion artifacts and repeated if obvious artifacts were detected. The effective dose was 3 μSv per measurement [21].

Attenuation values were converted to equivalent hydroxyapatite (HA) density (mg HA/cm^3) by deriving a linear relationship measured from the scan of a phantom containing cylinders of HA-resin mixtures with five different concentrations (0, 100, 200, 400, and 800 mg HA/cm^3) (QRM, Möhrendorf, Germany). For quality control, the linear attenuation values of the phantom were monitored daily.

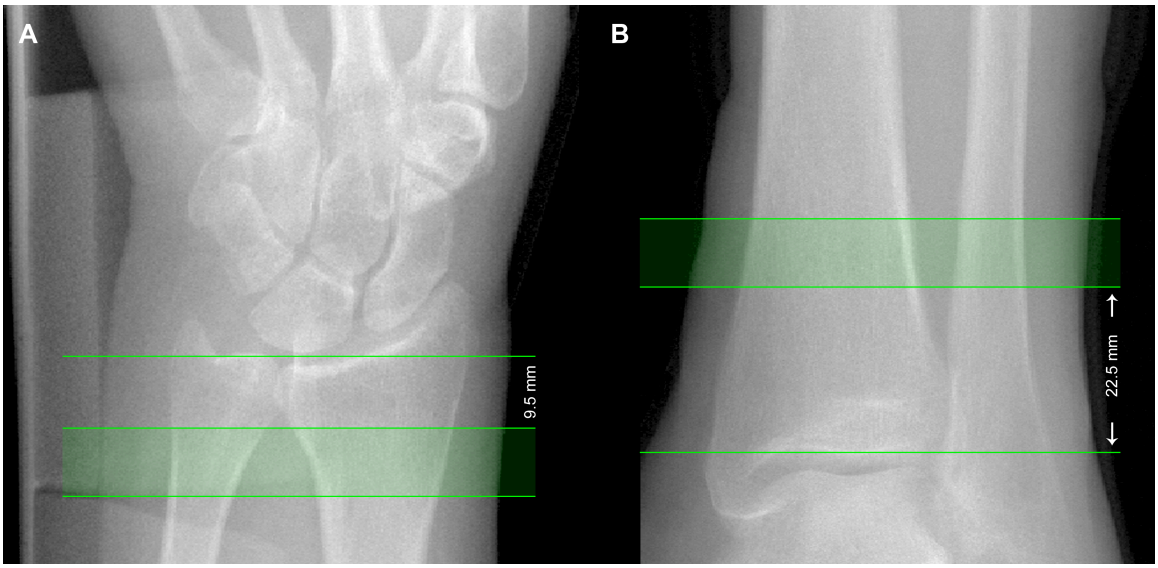

Figure 6.2 The standard location for HR-pQCT image acquisition and measurement, with respect to the reference landmarks at the distal radius (A) and tibia (B) (Courtesy of A Burghardt).

3. HR-pQCT analysis

Image Registration

Only a common volume of interest, identified using software provided by the manufacturer, between baseline, 12-month, and 24-month measurements was analyzed. The periosteal cross-sectional area (CSA) was calculated on a slice-by-slice basis for each time point. Cross-correlation was used to determine an optimal offset between the measurements to match the CSA between scans. As a result, the volume of interest (VOI) was generally less than the full 110 slices acquired (average = 103 slices). All subsequent analyses of HR-pQCT data were applied to the common VOI.

HR-pQCT Image Analysis (Standard patient style analysis)

The images were segmented and processed in accordance to the standard patient-style analysis protocol using Image Processing Language (Scanco Medical AG, Brüttisellen, Switzerland) as described elsewhere [7-9, 17-20]. First, a semi-automated edge-defining algorithm was applied to the original grayscale image to contour the periosteal surface. The total volumetric bone mineral density (vBMD) was calculated within this contour. The cortical and trabecular regions were segmented automatically by the analysis protocol as described in detail by Laib et al [22]. In brief, the trabecular compartment was smoothed out by applying a 3D Gaussian operator first, followed by a fixed threshold (16% of the positive integer space). As a result, cortex was separated from background. Cortical volumetric BMD (Ct.vBMD) was calculated as the mean density within this segmented cortical VOI; cortical thickness (Ct.Th) and cortical area (Ct.Ar) were calculated using an annular model approximation [23].

Calculation of the trabecular densitometric and structural indices from HR-pQCT images has been described in the previous chapters as well as elsewhere [22], validated [24-26] and employed in many studies [7-9, 17-20, 27]. First, bone volume fraction (BV/TV)

was derived from trabecular volumetric BMD (Tb.vBMD) and assuming the fully mineralized trabecular bone has a density of 1200 mg HA/cm^3. The mineralized phase was extracted by applying a Laplace-Hamming filter followed by a fixed global threshold (40% of the positive integer space), which resulted in binary representation of trabecular bone [28]. In addition to the BV/TV, trabecular number (Tb.N), thickness (Tb.Th), separation (Tb.Sp), standard for the patient analysis, the standard deviation of trabecular separation (Tb.1/N.SD, μm) was taken as a measure of heterogeneity in trabecular distribution [29]. The reproducibility of the trabecular structure indices obtained from in vivo HR-pQCT images is ≤ 5.8% at the radius and ≤1.5% at the tibia [19].

Subregional analysis

In addition to the standard patient-style evaluation, which results in a global average value for the entire volume, the following process for defining subregions was performed automatically using an algorithm developed in house. The trabecular compartment was divided into two concentric regions (inner and outer subregions), where the area of the inner subregion was 60% of the entire trabecular region. The volume was further divided into axial quadrants. In the leg, a line connecting the axial centroids of the tibia and fibula and its orthogonal compliment defined approximately medial-lateral/anterior-posterior quadrants. In the forearm, the major and minor axes of the axial cross section of the radius defined medial-lateral/anterior-posterior quadrants. A total of 4 cortical quadrants and 8 trabecular subregions resulted, as shown in **Figure 6.3**. Mean cortical and trabecular densitometric and micro-architectural indices were computed for each individual subregion.

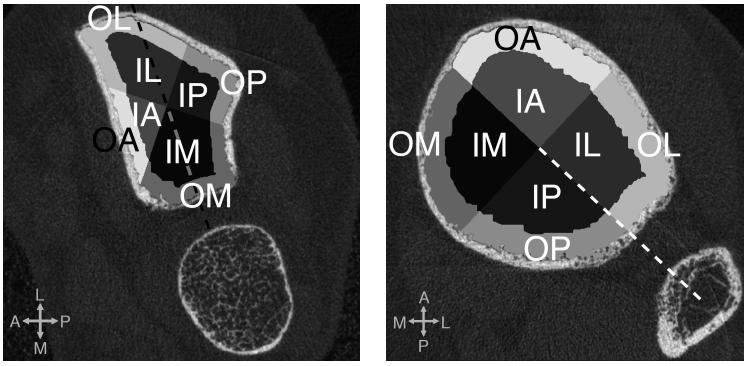

Figure 6.3 Definition for region-based analyses shown for the radius (left) and tibia (right). Each subregion was denoted by a two letter acronym two based on location: I or O for inner or outer subregions, respectively; and M, P, L, or A for medial, posterior, lateral and anterior, respectively.

4. Statistical Analysis

Results were summarized and the percentage differences from baseline values were presented for the treated (ALN) and placebo (PBO) groups. The significance of the differences in mean values due to time and treatment was assessed using a two-way analysis of variance with repeated measures on time (RMANOVA) with $\alpha = 0.05$. A significance level of $p < 0.05$ was considered statistically significant. All statistical tests were performed using JMP (version 7.0, SAS Institute Inc., Cary NC).

III. RESULTS

Twenty subjects in the ALN-treated group and 13 in placebo group remained at the end of the two-year study. Baseline age, months since menopause, and total hip and spine T-scores were not significantly different between the baseline and 24-month groups (Table 5.1).

Figure 6.4 illustrates the percent global and selected regional changes in Ct.vBMD, Ct.Th and Tb.N at the distal radius and tibia at 12- and 24-months with respect to the baseline values for each group. **Figure 6.5** displays the mean percent regional changes in Tb.vBMD, Tb.N and Ct.Th at the distal radius and tibia at 24-months with respect to the

baseline values. **Figure 6.6** summarizes the regions with significant treatment effect at 24-months.

In the distal radius, no significant longitudinal or treatment effect was detected globally, except in the total and trabecular BMD at 12 months (**Figure 6.4**). Total and trabecular BMD were unchanged in the ALN-treated group at 12- or 24-months while they significantly declined by 3% in the placebo group at 12-months ($p < 0.05$) compared to baseline (data not shown). Subregional analysis, on the other hand, revealed significant treatment effects mainly in the lateral quadrant ($p < 0.05$) (**Figure 6.6**) – at 24-months, trabecular BMD increased by 5% in the ALN group but 3% in PBO in the IL subregion (both p = NS); similarly, it remained unchanged in the ALN group but decreased by 3% in the PBO group in the outer-posterior (OP) subregion (**Figure 6.5**), resulting in significant difference between the groups ($p < 0.05$). Significant treatment effects in Ct.Th and Ct.Ar as well as in Tb.N and Tb.Sp were detected in the lateral quadrant (**Figure 6.4** and **Figure 6.6**). For instance, at 24 months, Ct.Th in the lateral quadrant decreased 10% from the baseline value in the placebo group ($p < 0.01$), but it was maintained in the ALN-treated group (-2%, p = NS); similarly, Tb.N in the lateral quadrant decreased 2 to 4% in the placebo group after 24 months, but it increased by 3 to 4% in the ALN-treated group (p = NS except for $p < 0.05$ in the IL region) (**Figure 6.5**).

In the distal tibia, in the cortical compartment, ALN treatment maintained Ct.vBMD and increased Ct.Th (**Figure 6.4**) and Ct.Ar. Globally, while Ct.vBMD decreased to 1.5% of the baseline value in the placebo group at 12-months ($p < 0.01$), it was maintained in the ALN-treated group throughout (p = NS) (**Figure 6.4**). Subregional analysis revealed that this significant treatment effect in Ct.vBMD was in fact focal in the posterior quadrant ($p < 0.05$) (**Figure 6.6**), as the increase in the ALN-treated group and the decrease in the PBO-group were large compared to the other regions (data not shown). Tibial geometry was

altered by ALN treatment – globally, both Ct.Th and Ct.Ar increased 2% and 3%, respectively, after 12- and 24-months (all $p < 0.05$) while they remained unchanged for the placebo group (**Figure 6.4**). Subregional analysis detected this significant treatment effects to be focal in the posterior quadrant (**Figure 6.6**), and larger than the effects observed globally – at 24 months, Ct.Th and Ct.Ar were 5% and 4% larger, respectively, compared to the baseline values in this region due to ALN treatment ($p < 0.05$), while they were both 2% smaller (all p = NS) in the placebo group (**Figure 6.5**). In the trabecular compartment, globally, neither longitudinal or treatment effect was detected (**Figure 6.4**). Subregional analysis, however, detected significant treatment effect in Tb.vBMD in the IL subregion only (**Figure 6.6**) – it increased by 4% compared to baseline in the ALN group ($p < 0.05$) while decreased by 2% in the PBO group (**Figure 6.5**).

Table 6.1 Study patient characteristics

	Baseline		24-months	
	PBO (N=27)	ALN (N=26)	PBO (N=13)	ALN (N=20)
Age [yrs]	55.4 ± 3.3	55.8 ± 3.9	56.4 ± 2.4	56.1 ± 4.1
Total Hip T-score	-0.8 ± 0.6	-0.8 ± 0.6	-0.8 ± 0.5	-0.7 ± 0.7
Lumbar Spine T-score	-1.0 ± 0.7	-1.2 ± 0.7	-1.1 ± 0.7	-1.1 ± 0.7
Months since menopause	31.5 ± 17.8	30.5 ± 17.4	33.5 ± 18.6	32.0 ± 16.6

N.B. No statistically significant differences between PBO and ALN at baseline or 24 months

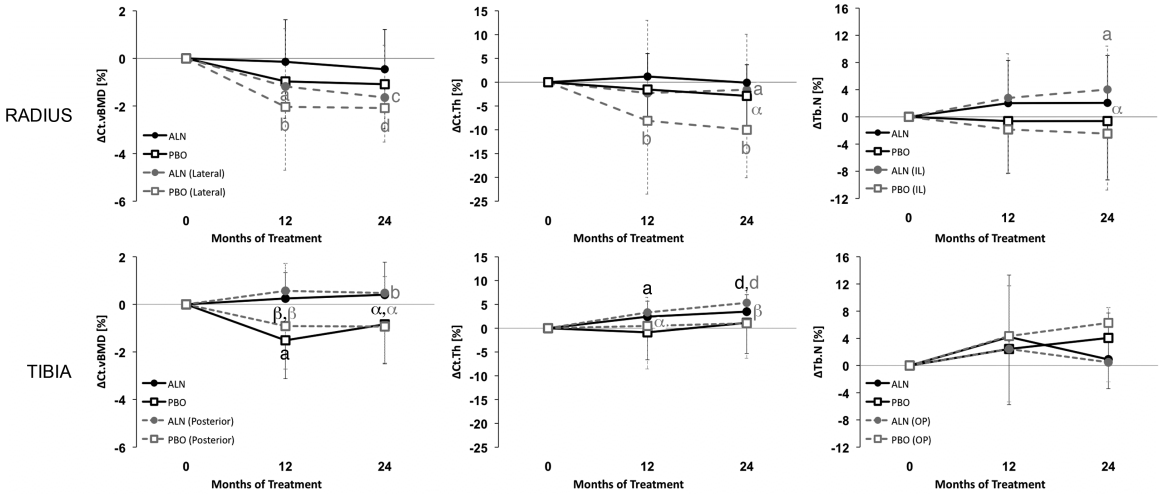

Figure 6.4 Line-plot of the mean % change in Ct.vBMD, Ct.Th, and Tb.N at the distal radius and tibia for the ALN-treated group (filled circle) and the placebo group (open square) after 12- and 24-months compared to baseline. (Adapted from Burghardt et al 2010). Overlayed in gray are the results of subregional analysis: for the lateral quadrant and the IL subregion for the cortical and trabecular parameters of the radius, respectively, and the posterior quadrant and the OP subregion of the distal tibia, respectively (**Figure 6.3**). $^{a}p < 0.05$, $^{b}p < 0.01$, $^{c}p < 0.001$, $^{d}p < 0.0001$ with respect to baseline; $^{\alpha}p < 0.05$, $^{\beta}p < 0.01$, $^{\gamma}p < 0.001$, $^{\delta}p < 0.0001$ ALN vs. PBO.

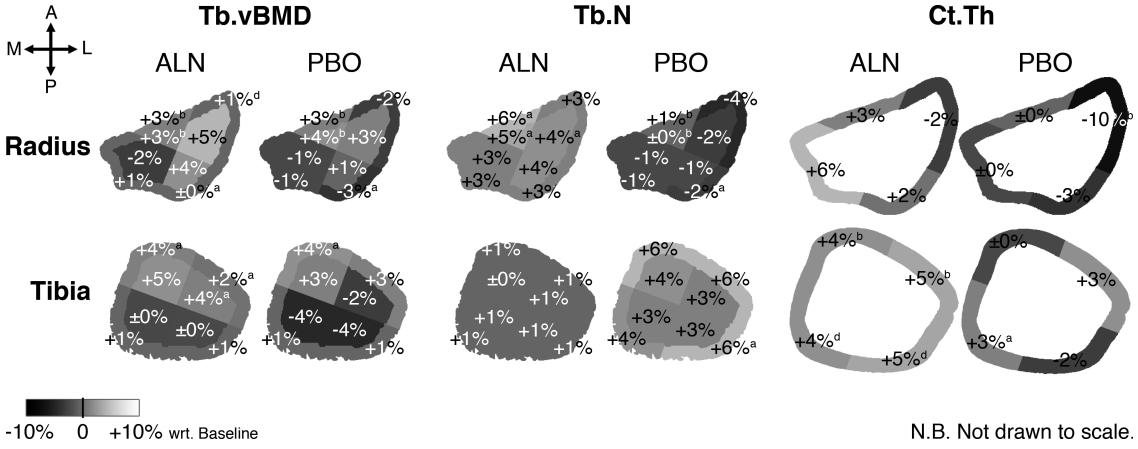

Figure 6.5 Mean percent differences in Tb.vBMD, Tb.N and Ct.Th at each subregion of the distal radius and tibia at 24-months compared to baseline for each group. $^{a}p < 0.05$; $^{b}p < 0.01$; $^{c}p < 0.001$; $^{d}p < 0.0001$; otherwise, not significant.

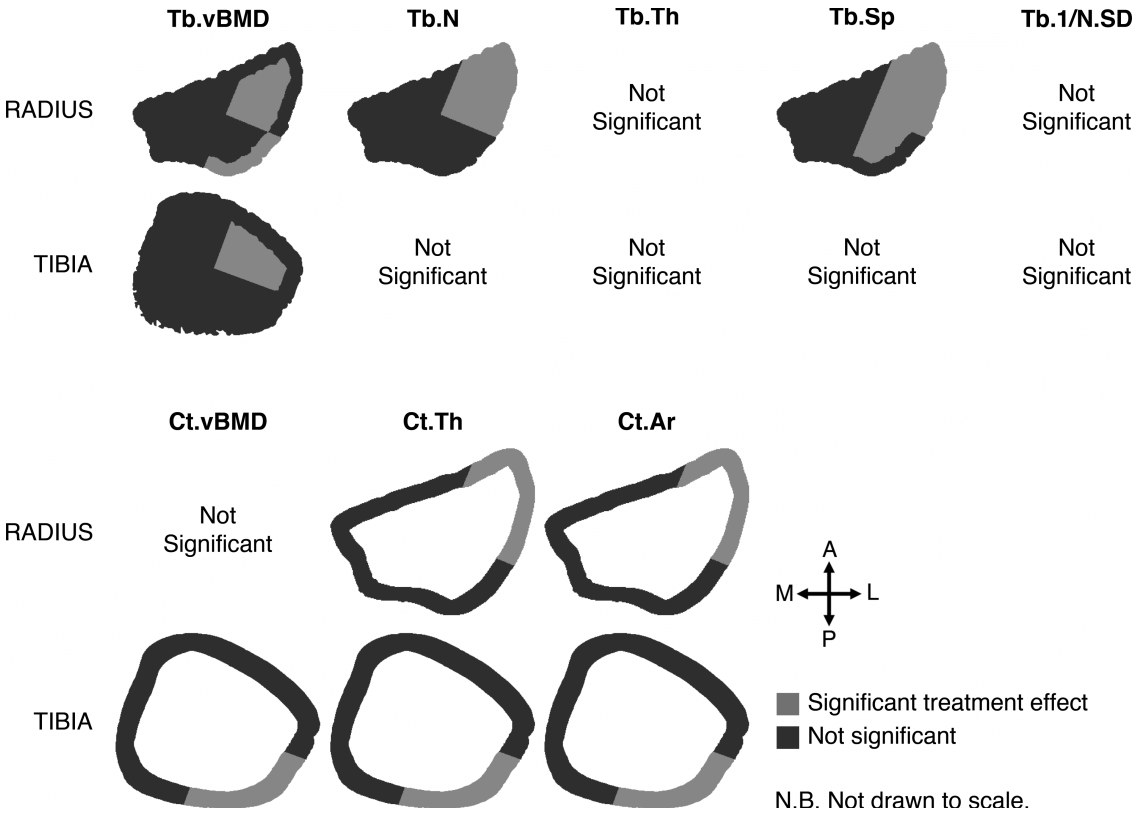

Figure 6.6 The summary of the regions with a significant treatment effect ($p < 0.05$) in selected trabecular and cortical parameters after 24 months (highlighted in light gray), determined by RMANOVA with time as a repeated measure.

IV. DISCUSSION

The effects of alendronate treatment on cortical and trabecular bone at the distal radius and tibia were assessed by HR-pQCT globally as well as regionally in this longitudinal study. With alendronate treatment, vBMD was maintained at the radius and significantly increased at the tibia over 24 months, compared to the placebo group, supporting the reports from the previous studies on anti-resorptive drugs [11, 12].

This study is novel not only for investigating alendronate effects in cortical geometric and trabecular structure in detail for the first time, but also for applying subregional analysis in addition to the conventional global analysis for more complete information. At the distal radius, while no treatment effect in the density (except in Tb.vBMD at 24 months), cortical geometric, and trabecular structure parameters was

detected globally after 12- or 24-months, subregional analysis detected the significant treatment effects mainly in the lateral quadrant. At the distal tibia, in addition to the global significant treatment effects in the density and cortical geometry parameters, subregional analysis further revealed that the effects were predominantly at the posterior quadrant. This result highlights the strength subregional analysis: the sensitivity to detect localized treatment effects that may be obscured by the global analysis.

The lateral quadrant at the distal radius and tibia where the substantial treatment effect in the trabecular bone structure was detected (**Figure 6.6**) feature markedly thin and scarce trabeculae for elderly female (**Figure 6.1**) [14]. Similarly, the lateral quadrant of the distal radius and the posterior quadrant of the distal tibia where significant treatment effects on cortical geometric parameter were detected (**Figure 6.6**) also feature anecdotally thin cortex. Therefore, our hypothesis that treatment effect was pronounced in the region with low bone mass was true. There are few potential explanations for this observation. First, biologically, low bone mass implies more surface area available for bone resorption to take place. Therefore, anti-resorptive effect of alendronate is more noticeable. Second, because of the intrinsically low values and high variance in density, cortical geometry and trabecular structure parameters, a change due to alendronate may be amplified. Therefore the observed significant longitudinal and treatment effects should be interpreted carefully. Biomechanically, bone in the region with high load (e.g. primarily on the medial and posterior part of the distal tibia) is expected to remain mechanically intact. In fact, trabecular structure in the outer-medial (OM) subregion not only features higher BV/TV and Tb.N compared to the global values for elderly women, but also is not affected by age [14]. Indeed, no significant longitudinal or treatment effect was detected in any of the tested parameters at the distal tibia in this study (data not shown).

There are several limitations worth mentioning. The small number of subjects may have confounded the statistical power. As the reproducibility for cortical geometry and trabecular structure indices are not as high compared to densitometric indices, the significance in difference observed in this study requires careful interpretation. Note that our results are consistent with the results of 12-month longitudinal study on postmenopausal women with alendronate and denosumab combined treatment [30]. The determination of the common VOI between baseline and follow-up scans based on 2D periosteal cross-sectional area matching is less accurate than the three-dimensional registration [20], and may have introduced an error as it does not account for potential periosteal apposition; to our best knowledge, significant periosteal expansion has not been reported with the clinical dose of alendronate previously [31], however. The changes in BV/TV and Ct.Th may have been overestimated as alendronate has been found to increase tissue mineralization by as much as 10% [23, 32]. Although Tb.vBMD measurement from HR-pQCT images is affected by the geometry [33], its effect is negligible for longitudinal changes.

In this chapter, subregional analysis was applied to a double-blinded, placebo-controlled randomized pilot study for characterizing the cortical geometric and trabecular micro-architectural response to alendronate in postmenopausal women with low bone density using noninvasive HR-pQCT imaging. Subregional analysis revealed the significant treatment and longitudinal effects in the distal radius where the conventional global analysis did not show; it also revealed that the effects were more pronounced and focal in the lateral subregion of the distal tibia. The region with significant effects coincided with low bone mass, which is relevant considering the local biomechanical environment as well as the effects of the intervention. The results of this study displayed the potency of

subregional analysis for providing additional and valuable information that supplement the conventional global analysis that may be more relevant for a clinical study.

REFERENCES

[1] Osteoporosis prevention, diagnosis, and therapy. NIH Consens Statement 2000; 17: 1-45.

[2] Bevill G, Eswaran SK, Gupta A, Papadopoulos P, Keaveny TM. Influence of bone volume fraction and architecture on computed large-deformation failure mechanisms in human trabecular bone. Bone 2006; 39: 1218-25.

[3] Liu XS, Sajda P, Saha PK, Wehrli FW, Guo XE. Quantification of the roles of trabecular microarchitecture and trabecular type in determining the elastic modulus of human trabecular bone. J Bone Miner Res 2006; 21: 1608-17.

[4] MacNeil JA, Boyd SK. Load distribution and the predictive power of morphological indices in the distal radius and tibia by high resolution peripheral quantitative computed tomography. Bone 2007; 41: 129-37.

[5] Ulrich D, van Rietbergen B, Laib A, Ruegsegger P. Load transfer analysis of the distal radius from in-vivo high-resolution CT-imaging. J Biomech 1999; 32: 821-8.

[6] Boutroy S, Van Rietbergen B, Sornay-Rendu E, Munoz F, Bouxsein ML, Delmas PD. Finite element analysis based on in vivo HR-pQCT images of the distal radius is associated with wrist fracture in postmenopausal women. J Bone Miner Res 2008; 23: 392-9.

[7] Melton LJ, 3rd, Riggs BL, van Lenthe GH, Achenbach SJ, Muller R, Bouxsein ML, Amin S, Atkinson EJ, Khosla S. Contribution of in vivo structural measurements and load/strength ratios to the determination of forearm fracture risk in postmenopausal women. J Bone Miner Res 2007; 22: 1442-8.

[8] Sornay-Rendu E, Boutroy S, Munoz F, Delmas PD. Alterations of cortical and trabecular architecture are associated with fractures in postmenopausal women, partially independent of decreased BMD measured by DXA: the OFELY study. J Bone Miner Res 2007; 22: 425-33.

[9] Vico L, Zouch M, Amirouche A, Frère D, Laroche N, Koller B, Laib A, Thomas T, Alexandre C. High-Resolution pQCT Analysis at the Distal Radius and Tibia Discriminates Patients With Recent Wrist and Femoral Neck Fractures. Journal of Bone and Mineral Research 2008; 23: 1741-1750.

[10] Brown JP, Josse RG. 2002 clinical practice guidelines for the diagnosis and management of osteoporosis in Canada. CMAJ 2002; 167: S1-34.

[11] Cummings SR, Black DM, Thompson DE, Applegate WB, Barrett-Connor E, Musliner TA, Palermo L, Prineas R, Rubin SM, Scott JC, Vogt T, Wallace R, Yates AJ, LaCroix AZ. Effect of alendronate on risk of fracture in women with low bone density but without vertebral fractures: results from the Fracture Intervention Trial. JAMA 1998; 280: 2077-82.

[12] Greenspan SL, Parker RA, Ferguson L, Rosen HN, Maitland-Ramsey L, Karpf DB. Early changes in biochemical markers of bone turnover predict the long-term response to alendronate therapy in representative elderly women: a randomized clinical trial. J Bone Miner Res 1998; 13: 1431-8.

[13] Black DM, Cummings SR, Karpf DB, Cauley JA, Thompson DE, Nevitt MC, Bauer DC, Genant HK, Haskell WL, Marcus R, Ott SM, Torner JC, Quandt SA, Reiss TF, Ensrud

KE. Randomised trial of effect of alendronate on risk of fracture in women with existing vertebral fractures. Fracture Intervention Trial Research Group. Lancet 1996; 348: 1535-41.

[14] Sode M, Burghardt AJ, Kazakia GJ, Link TM, Majumdar S. Regional variations of gender-specific and age-related differences in trabecular bone structure of the distal radius and tibia. Bone 2010.

[15] Burghardt AJ, Kazakia GJ, Sode M, de Papp AE, Link TM, Majumdar S. A longitudinal HR-pQCT study of alendronate treatment in post-menopausal women with low bone density: Relations between density, cortical and trabecular micro-architecture, biomechanics, and bone turnover. J Bone Miner Res 2010.

[16] Assessment of fracture risk and its application to screening for postmenopausal osteoporosis. Report of a WHO Study Group. World Health Organ Tech Rep Ser 1994; 843: 1-129.

[17] Boutroy S, Bouxsein ML, Munoz F, Delmas PD. In vivo assessment of trabecular bone microarchitecture by high-resolution peripheral quantitative computed tomography. J Clin Endocrinol Metab 2005; 90: 6508-15.

[18] Dalzell N, Kaptoge S, Morris N, Berthier A, Koller B, Braak L, van Rietbergen B, Reeve J. Bone micro-architecture and determinants of strength in the radius and tibia: age-related changes in a population-based study of normal adults measured with high-resolution pQCT. Osteoporos Int 2009; 20: 1683-94.

[19] Kazakia GJ, Hyun B, Burghardt AJ, Krug R, Newitt DC, de Papp AE, Link TM, Majumdar S. In vivo determination of bone structure in postmenopausal women: a comparison of HR-pQCT and high-field MR imaging. J Bone Miner Res 2008; 23: 463-74.

[20] MacNeil JA, Boyd SK. Improved reproducibility of high-resolution peripheral quantitative computed tomography for measurement of bone quality. Med Eng Phys 2008; 30: 792-9.

[21] Laib A, Hammerle S, Koller B. A new 100 μm resolution scanner for in vivo 3D-CT of the human forearm and lower leg. In: 16th International Bone Densitometry Workshop. Annecy, France; 2004.

[22] Laib A, Hauselmann HJ, Ruegsegger P. In vivo high resolution 3D-QCT of the human forearm. Technol Health Care 1998; 6: 329-37.

[23] Davis KA, Burghardt AJ, Link TM, Majumdar S. The effects of geometric and threshold definitions on cortical bone metrics assessed by in vivo high-resolution peripheral quantitative computed tomography. Calcif Tissue Int 2007; 81: 364-71.

[24] Laib A, Ruegsegger P. Calibration of trabecular bone structure measurements of in vivo three-dimensional peripheral quantitative computed tomography with 28-microm-resolution microcomputed tomography. Bone 1999; 24: 35-9.

[25] MacNeil JA, Boyd SK. Accuracy of high-resolution peripheral quantitative computed tomography for measurement of bone quality. Med Eng Phys 2007; 29: 1096-105.

[26] Muller R, Koller B, Hildebrand T, Laib A, Gianolini S, Ruegsegger P. Resolution dependency of microstructural properties of cancellous bone based on three-dimensional mu-tomography. Technol Health Care 1996; 4: 113-9.

[27] Khosla S, Riggs BL, Atkinson EJ, Oberg AL, McDaniel LJ, Holets M, Peterson JM, Melton LJ, 3rd. Effects of sex and age on bone microstructure at the ultradistal radius: a population-based noninvasive in vivo assessment. J Bone Miner Res 2006; 21: 124-31.

[28] Laib A, Ruegsegger P. Comparison of structure extraction methods for in vivo trabecular bone measurements. Comput Med Imaging Graph 1999; 23: 69-74.

[29] Laib A, Newitt DC, Lu Y, Majumdar S. New model-independent measures of trabecular bone structure applied to in vivo high-resolution MR images. Osteoporos Int 2002; 13: 130-6.

[30] Seeman E, Delmas PD, Hanley DA, Sellmeyer D, Cheung AM, Shane E, Kearns A, Thomas T, Boyd SK, Boutroy S, Bogado C, Majumdar S, Fan M, Libanati C, Zanchetta J. Microarchitectural deterioration of cortical and trabecular bone: Differing effects of denosumab and alendronate. J Bone Miner Res 2010.

[31] Allen MR, Follet H, Khurana M, Sato M, Burr DB. Antiremodeling agents influence osteoblast activity differently in modeling and remodeling sites of canine rib. Calcif Tissue Int 2006; 79: 255-61.

[32] Boivin GY, Chavassieux PM, Santora AC, Yates J, Meunier PJ. Alendronate increases bone strength by increasing the mean degree of mineralization of bone tissue in osteoporotic women. Bone 2000; 27: 687-94.

[33] Sekhon K, Kazakia GJ, Burghardt AJ, Hermannsson B, Majumdar S. Accuracy of volumetric bone mineral density measurement in high-resolution peripheral quantitative computed tomography. Bone 2009; 45: 473-9.

Chapter 7 – Conclusion

Taking advantage of its 82 μm nominal resolution, characterization of trabecular bone structure from *in vivo* high-resolution peripheral quantitative computed tomography (HR-pQCT) images has become a part of the assessment of skeletal status. In this dissertation, two sources of error associated with assessment of trabecular bone structure from HR-pQCT images, namely errors from the partial volume effect on non-metric indices and motion artifact errors, were characterized. Furthermore, a quantitative motion detection technique and regional analysis were proposed for improving assessment of trabecular bone structure.

In summary, three non-metric indices of trabecular bone structure – structure model index (SMI), connectivity density (Conn.D) and degree of anisotropy (DA) – were affected by the spatial resolution of CT images. The SMI deviated from the high-resolution μCT reference value depending on the structure type, whether plate-like or rod-like. The Conn.D and DA were both underestimated at an *in vivo* HR-pQCT resolution (82 μm) (Chapter 2). Using the proposed motion detection technique, the strong correlations were detected between the motion-induced error in density and trabecular structure indices and the motion estimate (Chapter 3).

Regional analysis where trabecular structure indices were calculated in 8 regions was proposed (Chapter 4). Substantial regional variability in trabecular bone structure across the cross-section at the distal radius and tibia was revealed. Gender differences were more prominent in the inner-lateral (IA) subregion at the distal radius but not as pronounced in the tibia. Age-related differences were more prominent in the inner-posterior (IP) subregion for the radius and in both inner-lateral (IL) and IA subregions for

the tibia. Furthermore, regional analysis was applied to a longitudinal, double-blind, placebo-controlled randomized study to test the efficacy of alendronate treatment over 24 months (Chapter 5). While no treatment effect was detected globally after 12- or 24-months, subregional analysis detected the significant treatment effects mainly in the lateral quadrant of the distal radius. It also revealed that the significant treatment effects were indeed driven by treatment in the posterior quadrant.

In conclusion, the results of studies in this dissertation have provided a basis for understanding associated errors in trabecular structural indices derived from HR-pQCT images. Furthermore, the proposed quantitative motion detection technique and regional analysis can be utilized in assessing trabecular bone structure using HR-pQCT. While there exist other sources of error worth addressing (e.g. beam hardening) as well as room for improvements (e.g. better motion correction and more robust beam hardening correction), the results of this work can be used as a guideline for establishing a standardized protocol across studies, scanners, and study centers. Collectively, this dissertation work helps advance the use of HR-pQCT as an effective tool for assessing skeletal status in research and clinical studies.

Publishing Agreement

It is the policy of the University to encourage the distribution of all theses, dissertations, and manuscripts. Copies of all UCSF theses, dissertations, and manuscripts will be routed to the library via the Graduate Division. The library will make all theses, dissertations, and manuscripts accessible to the public and will preserve these to the best of their abilities, in perpetuity.

Please sign the following statement:

I hereby grant permission to the Graduate Division of the University of California, San Francisco to release copies of my thesis, dissertation, or manuscript to the Campus Library to provide access and preservation, in whole or in part, in perpetuity.

September 24, 2010

Author Signature | Date